2018

PRESSURE MEASUREMENTS INSIDE MULTIPLE CAVITIES OF A TORQUE CONVERTER AND CFD CORRELATION

Edward De Jesus Rivera
Michigan Technological University, edejesus@mtu.edu

PRESSURE MEASUREMENTS INSIDE MULTIPLE CAVITIES OF A TORQUE CONVERTER AND CFD CORRELATION

By

Edward De Jesús Rivera

A DISSERTATION

Submitted in partial fulfillment of the requirements for the degree of

DOCTOR OF PHILOSOPHY

In Mechanical Engineering-Engineering Mechanics

MICHIGAN TECHNOLOGICAL UNIVERSITY

2018

This dissertation has been approved in partial fulfillment of the requirements for the Degree of DOCTOR OF PHILOSOPHY in Mechanical Engineering-Engineering Mechanics.

Department of Mechanical Engineering-Engineering Mechanics

Dissertation Advisor:	*Darrell Robinette*
Committee Member:	*Jason Blough*
Committee Member:	*Carl Anderson*
Committee Member:	*Gowtham S.*
Department Chair:	*William W. Predebon*

Table of Contents

List of Figures

List of Tables

Preface

There are multiple objectives when creating computer models. Industries are heavily relying on computer models to validate designs. In the future, all phases of development will be done with simulations. To fully rely on simulations for complex designs like torque converters, accuracy must be improved. Past professional experience with simulations done by others made me question validity of their results. Errors in the order of 30% for torque predictions cannot be correct. As a personal goal, I took on the challenge of learning how to simulate a torque converter. I successfully improved the accuracy by 5 times in most of my simulations, others were even better in the order of 1% error.

Solution time was a secondary personal goal. Past professional experiences showed results no earlier than a month after the project had started. After obtaining my first working model, solution times took 9 hours per speed ratio. Accuracy was good but nine hours per speed ratio was excessive and was eventually reduced to under 30 minutes for the torus only model while the full torque converter, solutions per speed ratio took less than 40 minutes. 1-D models showed me that I could obtain results in seconds. Unfortunately, the task to develop a good 1-D is daunting and difficult. I also learned that 1-D models are not repeatable. Each design require an exclusive 1-D model. CFD is more versatile and can be used with many geometries as long as good understanding and validation is done. Over the 2 years, 5 geometries were studied. The present work is for the torque converter geometry provided by Ford Motor Company. Four additional geometries from a different original

equipment manufacturer were studied with similar accuracies. The additional four geometries varied in size and blade shape.

Acknowledgements

To all teachers and professors encountered throughout all my years of education. To all sponsors especially Ford Motor Company, without their financial support and contribution to science, none of this work would have been possible. To my family and friends who shaped me into what I have become.

Thanks to IR Telemetrics who provided the impressive telemetry system and took the time to train us on how to use it. This project and many others before had not been possible without their knowledge and support.

Thanks to Hunter Wang and Manish Kumar from ANSYS. Without their help on getting the software running and guidance on setting up the initial stages of the model, I would still be cracking at it.

Thanks to Mark Woodland who was essential in building our laboratory and in setting up the multiple data acquisition systems used in both of our research projects.

Abstract

A torque converter was instrumented with 29 pressure transducers. The pressure transducers were located in multiple cavities. The instrumented cavities included, four transducers mounted on the impeller shell, on the channel between blades. Six transducers mounted on the pressure and suction sides on the middle streamline of a turbine blade. Another seven transducers mounted on the pressure and suction sides of the core, middle and shell streamlines of a stator blade. Seven transducers mounted on the torque converter clutch cavity. Finally, five on the cavity between the pressure plate and the turbine shell. The torque converter was part of a 6 speed front wheel drive transmission and differential, also instrumented with various pressure transducers, thermocouples and a flow meter. The transmission measurements were not in scope for the present work with the exception of the thermocouples, flow meter and torque converter clutch pressure, which approximated torque converter inlet pressure during early stages of the project.

A transmission lab was designed and built as part of the investigation. Acquisition of the torque converter pressure data was accomplished with a custom designed and built telemetry system developed for the present study by IRT Telemetrics located in Hancock Michigan.

A computational fluids dynamics model was developed using a commercially available software. The computer model was used to correlate with the torque converter measured torques and pressures. The computer model was optimized accuracy of predicted torques

and for accelerated solution time. Solution times were reduced from 9 hours to under 40 minutes per speed ratio while the accuracy of torques error varied by up to 6% between tests and simulation. Accuracy of pressure simulated values varied widely depending on the cavity under study. The torque converter inlet flow worked best with 5% turbulence intensity while other cavities such as the toroidal ones were best modeled with a turbulence intensity set to 50%.

The computer model was able to predict pressure trends during the many tests completed as part of the investigation. Flow recirculation was seen on the turbine and stator blade passages on the low speed ratios. The recirculation region affected simulated and measured pressures on both sides of the turbine and stator blades as seen in previous investigations.

Further studies should be carried out using the model developed as part of this work as a starting point. Further improvements in accuracy and solution time are highly valued by the industry to help reduce costs associated with computer time and development costs associated with inaccuracies.

1. Introduction

A transmission with an instrumented torque converter was tested over a wide range of steady state speeds and torques. The instrumented torque converter contained 29 pressure transducers located throughout the impeller, turbine, stator, pressure plate, and torque converter clutch cover.

1.1 Objectives

The main objectives of this research is to develop a Computational Fluids Dynamics (CFD) model of the experimental torque converter using a commercially available software. The CFD model must be optimized not only for reduced solution time but also for accuracy of predicted torques. Once a CFD model with optimal parameters is available, it will be used to correlate tested pressure and torque data gathered or documented as part of this investigation.

Accuracy in any analysis tool is of paramount importance. An inaccurate CFD tool is a costly endeavor. (Figure 1-1).

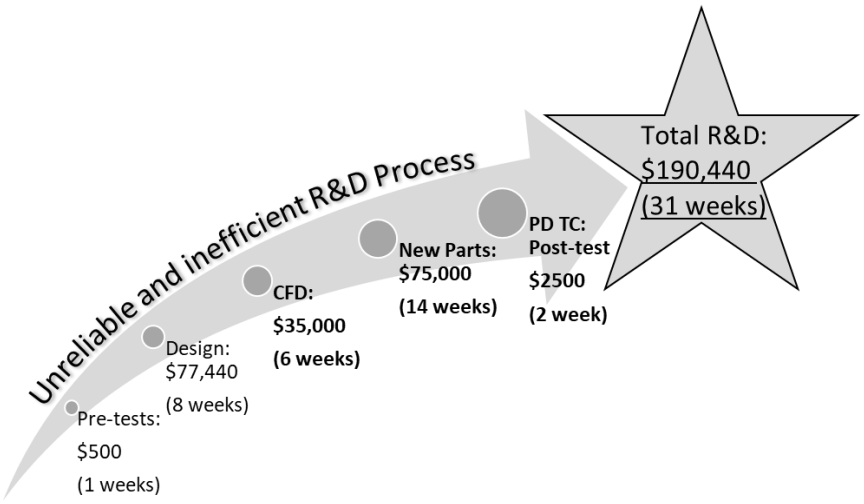

Figure 1-1. Typical inefficiencies (bold) in CFD process (one try cost).

On the simulation area, typical inefficiencies in the process may include inexperienced analysts. A torque converter is a complex turbomachine, complete and competent understanding is needed for an effective simulation. The analyst working on torque converter simulation today should not be working on lubrication systems tomorrow and body aerodynamics the following day. The analyst sole expertise should be in a single subject in order to tune in and truly understand the machine application or process. Only then, experience and expertise will be gained. Repeatability of the simulation is one of the most common sources of inefficiencies in the simulation process. As part of this investigation, accuracy of the results for several researches was studied and compared. It was seen that for each simulation reported by a single researcher, errors varied. The variation in error per simulation procedure once a method has been developed demonstrate the inability to replicate results. Another source of inefficiency is the lack of understanding of typical torque converter variation. A target 3% torque increase or decrease cannot be

achieved if the typical design variations in manufacture are up to +/-12% during test as in the case of the torque converter in this investigation. An efficient CFD process could reduce the cost associated with multiple design trials. Most cost associated with prototype testing could be reduced dramatically once a reliable process is determined (Figure 1-2).

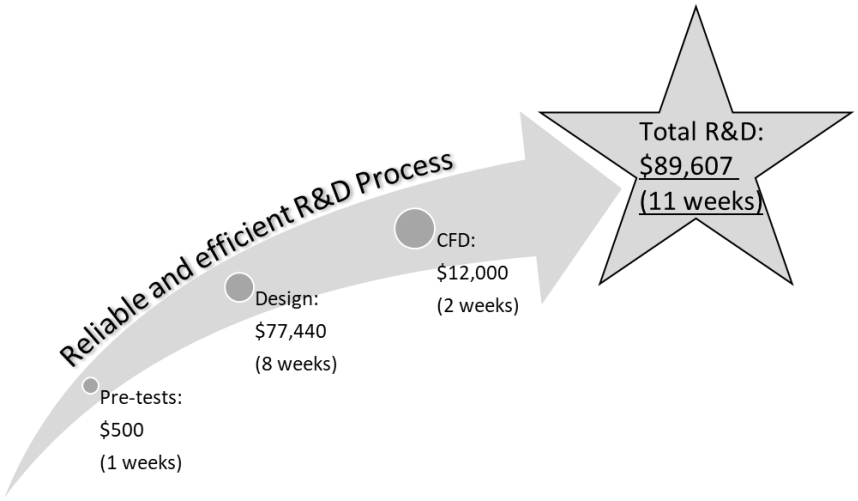

Figure 1-2. Efficient CFD process

The efficient CFD process have an attractive potential for research and development (R & D) cost reduction. The example represents the cost associated with inefficiencies of a CFD process per trial. Past experience dictates that throughout the design phase of a torque converter, at least two trials have been done with line of sight for a third. The bottom line of the problem when looked in terms of human resources is the fact that the money spent in such trial and error exercises could have supported a considerable number of potential employees (Figure 1-3).

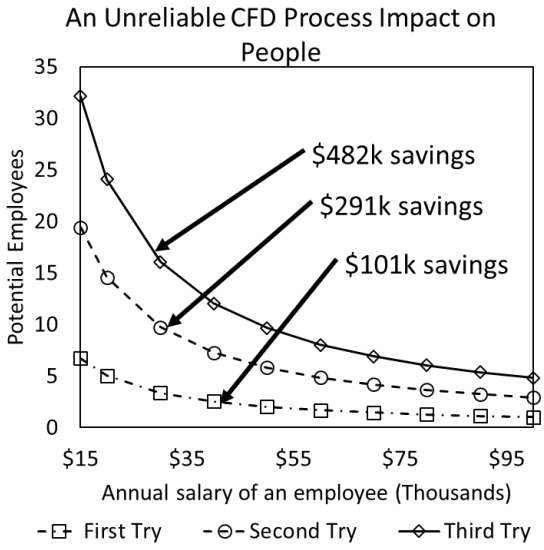

Figure 1-3. Human resources affected by inaccurate CFD process.

A CFD process must be fast in order to be implemented with accelerated new product introductions. It is because of these reasons, the present study had as a primary goal, the accuracy of the results and as a secondary goal, time to reach a solution. The solution times in the initial trials in the present investigation was 9 hours per speed ratio. The maximum torque errors in the simulation ranging as high as 11%. After an optimization of parameters in the simulation was completed, the solution times per speed ratio was reduced to 40 minutes. The maximum torque errors for the optimal simulation settings were reduced to less than 6% when temperature effects were considered.

1.2 Torque Converter Operation

A torque converter is a turbomachine with characteristics of a fluid coupling. It transmits torque from an engine into a transmission and multiplies torque during low speed ratios. It was first conceived by Dr. Hermann Foettinger in 1903 and referred to his invention as a

transformer [1]. The use of a torque converter allows for an overall smaller transmission package and reduces the number of gears/shift speeds on a transmission. Other benefits of employing a torque converter includes vibration reduction during shifting or engine firing. Torque converters are used over a wide range of applications that includes automotive and heavy construction industries and applications.

A basic torque converter consist of a pump or impeller, a turbine and a stator enclosed inside a pressurized vessel. A working fluid commonly referred to as Automatic Transmission Fluid (ATF) is pressurized. The torque converter impeller is attached to an engine that provides power (torque and speed) to the ATF. The ATF transmits that power to the turbine after energy losses have taken place. The turbine carries power into a transmission. The stator inside the torque converter provides torque multiplication during low speed ratios of operation (normally referred to as converter drive).

The ATF inside the torque converter follows a toroidal or circular path as it moves inside the torque converter around the impeller, turbine and stator (Figure 1-4).

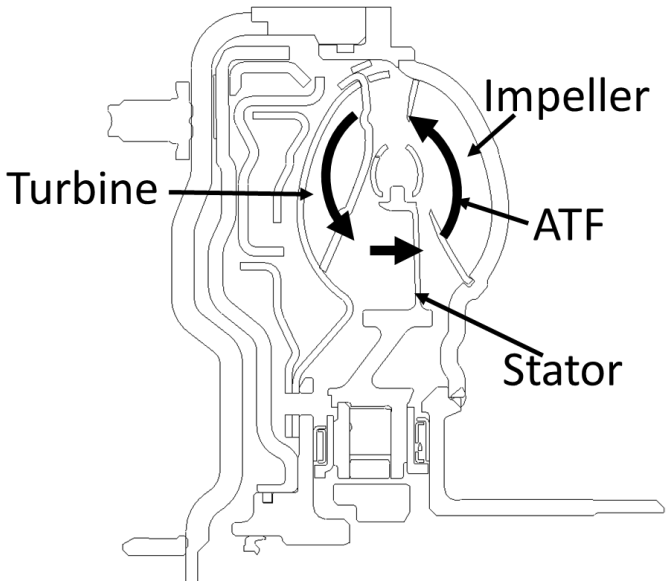

Figure 1-4. ATF flow path inside the torque converter.

Over the years, fuel economy have demanded torque converters that are more efficient. Features to improve a torque converter's overall efficiency include one-way clutches, lock-up clutches, torque dividers and in some instances multiple impellers, turbines and stators elements. The torque converter under study is characterized as a three-element, single-stage, double-phase torque converter with a torque converter clutch. Three-elements refers to, one impeller, one turbine and one stator. Single-stage means that the torque converter only has one turbine. Double phase refers to two methods of operation. Phase one, when the stator is fixed to allow for torque multiplication (low speed ratios or converter drive). Phase two, when the stator is allowed to spin (free-wheels) once the torque converter speed ratio is at or above the coupling point. The addition of the lock-up clutch allows the impeller and turbine to operate at the same speed carrying the same torque. Engaging the

lock-up clutch provides direct drive operating mode and further eliminates losses inside the torque converter caused by fluid shearing and heat generation.

1.3 Literature Review

1.3.1 Torque Converter CFD

Early turbomachine designs including torque converter performance approximation required the use of 1-D models. The use of 1-D model sometimes involved the use empirical data to approximate losses inside the torque converter. There is a variety of examples in literature where mathematical models were employed to understand such losses [2-13]. The disadvantages of any 1-D model relying on empirical or approximated loss models is the unreliability and lack of repeatability of accuracy levels from design to design. Many variations and 1-D models approximations have also been used to simulate performance of many other turbomachine types [14-28]. All 1-D models are based on many forms of loss estimates found in literature. Losses such as friction, slip, shock and secondary flow among others [29-31].

Numerical 3-D simulations, be it for a full torque converter geometry or just for a single-flow path have all been advances in Computational Fluids Dynamics (CFD) and have been used as a design tool for several decades. It allows design engineers to optimize or tune new products to meet required performance. CFD allows for flow visualization highlighting areas of inefficiencies inside a torque converter [32-39]. CFD have allowed cavitation in torque converters to be studied, visualized and in some instances mitigated

[36, 37]. Aside from flow visualization, one of the main uses of CFD is to allow design engineers to develop new torque converters. Input and output torque predictions are essential part of a proper new product introduction.

Prior studies showed a very wide range of accuracy when it comes to predicting torque converter behavior. While performing the literature review for this work, it was seen that some authors put a lot of emphasis and reported only non-dimensional numbers like torque ratio resulting in quantitative agreement but the qualitative results of the individual torques forming such ratios was far from desirable. Results presented by authors in the form of torque ratio and k-factors were used to estimate impeller and turbine torque discrepancy from test in percentage form (Equation 1-1).

$$T_{I_{CFD}} = \frac{N_I}{\left(KF_{I_{CFD}}\right)^2} = \frac{N_I}{\left[KF_{I_{test}} * (1 + E_{KF})\right]^2} = T_{I_{test}} * \frac{1}{(1 + E_{KF})^2} \qquad \text{Equation 1-1}$$

Where $T_{I_{CFD}}$ and $T_{I_{test}}$ represents the impeller torque obtained with the CFD and test respectively. The impeller speed is represented by N_I. The K-factor obtained with the CFD and test are represented by $KF_{I_{CFD}}$ and $KF_{I_{test}}$respectively. E_{KF} represents the K-factor's error percentage between test and CFD. Once the K-Factor error is known, it could be used to obtain the magnitude of the test and CFD impeller torque discrepancy (Equation 1-2).

$$E_I = \frac{1}{(1 + E_{KF})^2} - 1 \qquad \text{Equation 1-2}$$

Similarly, mathematical manipulation of torque ratio discrepancy between test and CFD along with the impeller torque discrepancy are used to obtain the turbine torque discrepancy (Equation 1-3).

$$T_{t_{CFD}} = TR_{CFD} * T_{I_{CFD}} = (TR_{test}) * \left(T_{I_{test}}\right) * (1 + E_{TR}) * (1 + E_I) \quad \text{Equation 1-3}$$

The CFD turbine torque and torque ratio are represented by $T_{t_{CFD}}$ and TR_{CFD} respectively. Similarly, the test turbine torque is represented by TR_{test}.Torque ratio discrepancy between test and CFD is represented by E_{TR}. Once the expression is known, the turbine torque discrepancy between test and CFD, (E_t), is easily calculated (Equation 1-4).

$$E_t = (1 + E_{TR}) * (1 + E_I) - 1 \quad \text{Equation 1-4}$$

The most accurate results studied are the ones presented by Schweitzer and Gandham [38]. Approximate accuracy discrepancies from test for torque ratio and K-Factor of -3% and -2% respectively yield errors within 5% for impeller and turbine torques. Good graphical correlation between test and simulation was also obtained by S. Jeyakumar and Sasikumar [39]. An analysis with various torque converter geometries was performed by Srinivasan et. al. reporting errors between model and test within -2% and 6% for impeller and turbine respectively and as high as 37% and -15% depending on torque converter case under study under similar model set ups [64]. The CFD error spread obtained may shed light into a worrisome fact about repeatability across designs especially if an engineer is tasked with designing a torque converter for which no experimental data is available. Discrepancy from test for K-factor, torque ratio, impeller and turbine torques errors of 10%, 6% , -17% and -12% respectively were reported by C. Liu while studying inlet angles on a torque converter

[40]. Torque ratio, k-factor, impeller and turbine torques on a CFD model presented by Migus M. resulted in calculated accuracy errors of 6%, -11%, 26% and 34% respectively while investigating simulated flow inside a torque converter [41]. A comparison between two commercial software was performed by Kathiresan M [42]. The better of the two commercial software yielded results within -32% for impeller torque, -26% for turbine torque. The K-factor and torque ratio results were within 22% and 9% compared to test respectively. Cavitation simulation proved essential in predicting torque converter performance parameters when compared against a non-cavitating simulation [43]. Impeller and turbine torque errors between simulation and test when cavitation was not taken into account were as high as -51% and -48% respectively. When cavitation was taken into consideration as part of the simulation, errors were reduced to 4% for the impeller torque and 2% for the turbine torque. Two more torque converter geometries showed improvement when cavitation was taken into account. The study also highlighted non-repeatable accuracy magnitudes for the three geometries studied. Another study comparing torque converter simulation when considering cavitation effects or not in the simulation was presented by Ju et al [44]. B. Liu reported K-factor and torque ratio errors of -6% and 6% when compared to test while studying flow induced oscillations inside a torque converter [45]. The errors in k-factor and torque ratio represent deviations in impeller and turbine torques of 14% and 21% respectively. WU Guangqiang reported K-factor and torque ratio discrepancy from test in the order of 11% and 7% respectively while studying converter designs and simulations [46]. Errors within -5% and 10% for k-factor and torque

ratio resulted in estimated impeller and turbine torque errors of 11% and 22% respectively while studying impeller flow in a torque converter [47]. The study found that pressure distributions at the exit affected negatively the flow characteristics. Stator flow studies on a torque converter showed approximate impeller and turbine torque errors as high as -48% and -49% respectively. Resulting K-factor and torque ratio errors were in the order of 39% and 1% respectively [48]. Accuracy of results compared to test of -7% for impeller and turbine torque were obtained while studying torque converter optimization parameters [49]. The resulting K-factor and torque ratio errors obtained were below 3% and -1% respectively. Errors below -9% and-10% for impeller and turbine torques were reported by Watanabe N. while studying a torque converter with CFD solver parameter improvements [50].

As can be seen, CFD accuracy presented by several authors varied widely depending not only on geometry but also on commercial software package and even CFD parameter set up. If the Root Mean Square Errors (RMSE) of the results found in the literature review were to be visualized graphically, it will show ranking in their procedure (Figure 1-5).

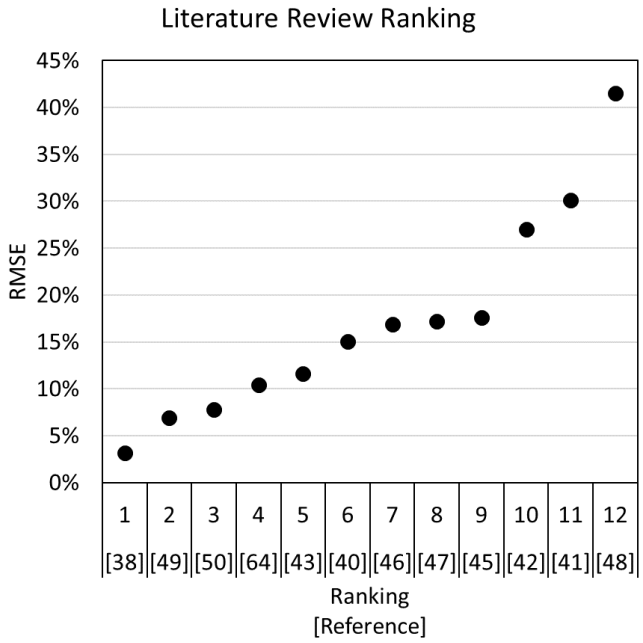

Figure 1-5. Literature CFD torque accuracies.

For the available data in the literature, error in torque prediction for the impeller and turbine torques can be statistically seen as a group (Table 1-1).

Table 1-1. Statistical parameters for torque errors found in literature CFD procedures.

Parameter	Impeller	Turbine
Minimum	0.0%	0.4%
Maximum	48%	49%
STD Dev.	14%	13%
Variance	2%	2%
Mean	14%	13%
Median	9%	8%
Mode	4%	4%

Other CFD modeling have been completed with various degrees of success all with different scopes. The use of CFD allows design optimizations to take place. A dual-blade stator design was studied and results were used to create a 1-D model [51]. Effects of turbine blade and impeller passage modification on torque converter efficiency were quantified and flow visualization possible when modeling a torque converter single path [52]. The simulated flow visualization results were in good agreement with experimental results. Impeller and turbine scroll angle impact on torque converter flow behavior was studied [53]. The results obtained could be used as guides as of what direction to take during early stages of design. CFD was also used in understating the effects of torque converter performance of two stator blade shapes [54]. Poor correlation between the simulation and test results were seen. The exercise highlighted the importance of the study while optimizing the torque converter performance. The effect of splitting the stator blade of an automotive torque converter demonstrated a more uniform flow and pressure distribution across blade sides [55]. The study showed that splitting the stator blade helped control flow separation and improved torque converter capacity.

Improvements in torque ratio and K-Factor were achieved by modifications to the stator blade shapes [56]. Among the modifications to the stator, an increase to the torque ratio at stall near 7.4% was observed which helped increase the torque converter efficiency by 1%. Other modifications allowed increase in pump torques of up to 28%. The leakage between elements of a torque converter can also be optimized with the use of CFD [57]. The study

demonstrated that the leakage could detrimentally affect stall torque ratio by around 3.6%. The leakage was also shown to reduce peak efficiency near 2%.

Flow phenomena that badly affect the torque converter performance are secondary losses caused by vortices and flow reversal. CFD provides an excellent tool for secondary flow understanding and visualization [58]. The study showed that CFD could be used to create models to predict vortex behavior.

Another use of CFD is not only to reduce the axial length (squashing) of a torque converter but also to understand losses associated with squashing [59].

1.3.2 Torque Converter Instrumentation

Instrumentation in torque converters have been achieved by past investigators. Temperature, pressure and flow velocities have all been successfully studied. Instrumentation on the blade tip of an automotive torque converter turbine blade was used to understand flow conditions entering the turbine [65]. Two automotive torque converter turbines were instrumented with strain gages to study the blade loading and micro-crack propagation near the inlet core tang/tab fillet radius [66]. The turbines were tested over a wide range of speed ratios for two constant impeller torques as well as at stall (SR=0) for several impeller speeds.

Torque converter instrumentation have been accomplished by different means with different degrees of success. Early measurement techniques concentrated on the non-

spinning components while the use of telemetry opened up the scope of possibilities. An automotive torque converter impeller was instrumented with five pressure transducers to study effects of cavitation instability and torque degradation during stall [67]. Their results demonstrated that cavitation inception is dependent on operating charge pressure and input speed. Torque degradation was observed during advanced cavitation. A stator was instrumented with fifteen pressure tabs on its nose to understand cavitation phenomena occurring at the leading edge of the stator blade [68]. The experiments showed that cavitation inception occurs at the stator leading edge and bubbles collapse near the impeller entrance.

One of the earliest instrumentations in a torque converter was done on a stator to study static pressure profiles at 72 locations [69]. The results obtained were used to calculate blade loading and extract stator torque by integration approximation between the measured pressures on both blades sides.

It will be shown that the procedure used to determine optimal CFD set up as part of this investigation yield very competitive accuracies for impeller and turbine torques under study. The torque results are of most importance than non-dimensional or semi-non-dimensional numbers and more emphasis will be put in them throughout the report with occasional discussion of non-dimensional ones.

The literature review has shown that although test and CFD correlation of pressures have been done to some extent in the past for the many regions of a torque converter, they have all been targeted individually and independently (e.g. impeller, turbine, stator, clutch

independently). The scope of the work presented here, encompasses all torque converter cavities instrumented all together and accompanied by a single, full torque converter computational fluids dynamics correlating model.

2 Experimental Setup

A transmission test stand was designed and built for Michigan Technological University as part of this investigation. The transmission studied is a six speed, front wheel drive automatic transmission with final drive. The transmission input is driven by an electric dynamometer controlled in either torque or speed mode. The output of the transmission was connected to an absorbing dynamometer that could be controlled in speed or torque mode as well. Gear shifting was achieved by an externally mounted control unit. Different transmission shift selection provided a variety of total gear ratios (Table 2-1).

Table 2-1. Transmission total gear ratios per gear selection after differential.

Gear Selection	Gear Ratio
1st	15.38
2nd	9.95
3rd	6.41
4th	4.85
5th	3.36
6th	2.50
Rev	-9.88

Working fluid (ATF) is contained within the transmission case. A hydraulic in-line mounted pump driven by the torque converter provided working fluid at the necessary flow rate and pressure. Pressures, temperatures and flows into and out of the transmission were monitored but not controlled. Final working pressures and flows were set by the transmission system.

2.1 Torque Converter Type

The torque converter is a three-element, single-stage, double-phase torque converter with torque converter clutch (TCC). More information about the torque converter will be provided in the next chapters.

2.2 Torque Converter Instrumentation Layout

The torque converter under study was instrumented with 29 pressure transducers located throughout the impeller, turbine, stator, clutch plate and other cavities in the torque converter. All the instrumentation hardware was custom designed, made and assembled by IR Telemetrics in Hancock, Michigan. Three different transmitters were used in the telemetry system. Each transmitter handled a series of pressure transducers. The instrumentation location discussed throughout this chapter may differ slightly from the final instrumentation location. An example of the reasons for the variation in the location of the sensors is that of the turbine and stator blades. Too many sensors and cabling in one blade, although possible will detrimentally affect flow characteristics. As a result, the transducers have been spread out throughout multiple blades.

2.2.1 Impeller & Cover Instrumentation

The impeller instrumentation was the easiest one to accomplish. All wiring was routed on the outside of the torque converter and into the externally mounted hardware (Figure 2-1).

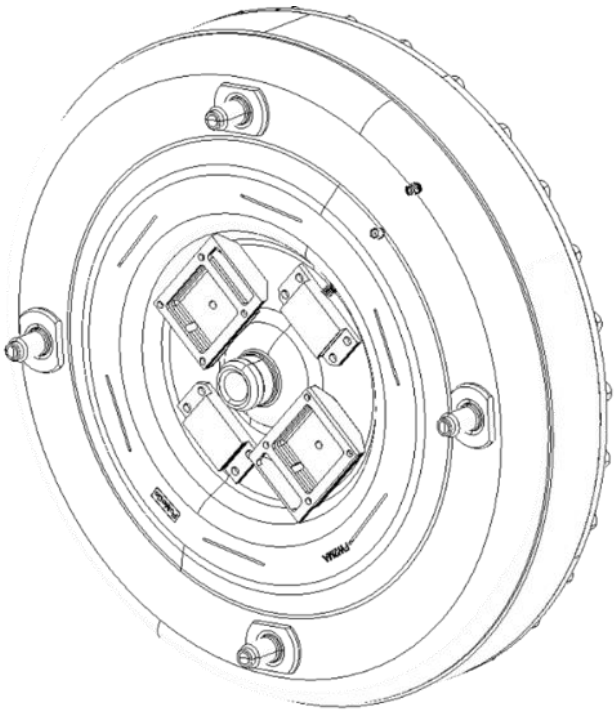

Figure 2-1. Impeller transmitter hardware mounted externally.

The telemetry signal bounces off inside the transmission bell housing until picked up by a series of antennas calibrated at frequencies set for the impeller transducer.

The impeller and cover transmitter worked with 7 pressure transducers. All pressure transducers around the impeller were Kulite-XCEL-072. With 1.9 mm diameter and 9.5 mm in length and given the available space around the impeller periphery, these sensors made a good fit for the investigation. The pressure range is for 200 psi and up to +/- 0.5% Full Scale Output (FSO) maximum hysteresis. The operating temperature range provides a very broad range of operation up to 235 degrees Celsius. There were 3 pressure transducers located on the impeller shell (Figure 2-2).

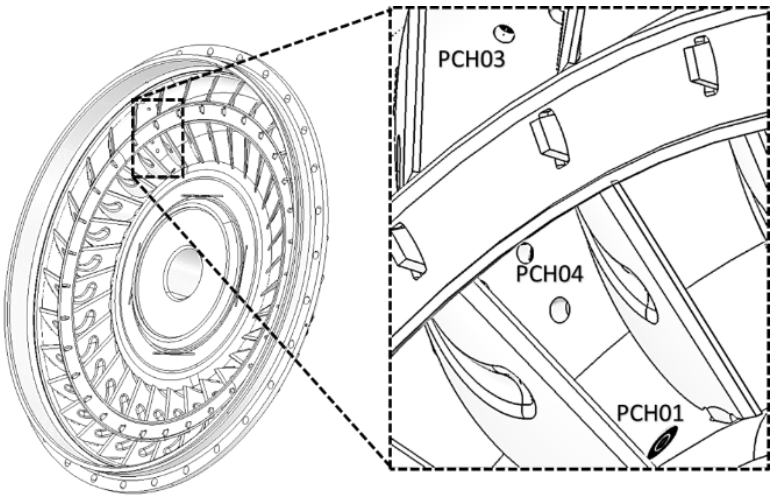

Figure 2-2. Impeller pressure transducers location.

The impeller and cover transmitter also worked with 3 pressure transducers mounted throughout the torque converter cover, two of them near the TCC (Figure 2-3).

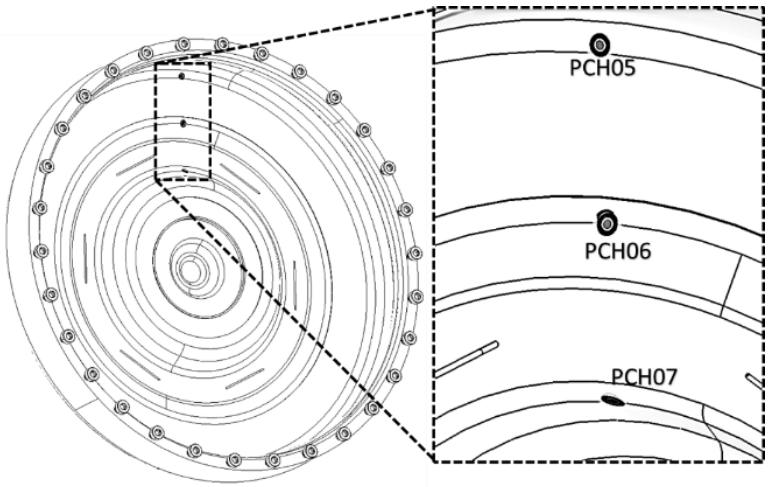

Figure 2-3. Torque converter cover pressure transducers location.

A cross-section of the torque converter provides a better view of the transducers located on the cover more clearly (Figure 2-4).

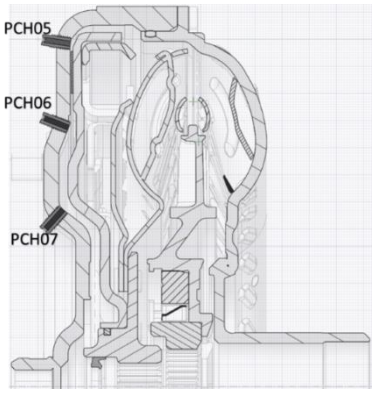

Figure 2-4. Cross section showing pressure transducers on the cover.

The last of the 7 pressure transducers handled by the impeller and cover transmitter is located outside the torus, roughly in the vicinity between the impeller and turbine (Figure 2-5).

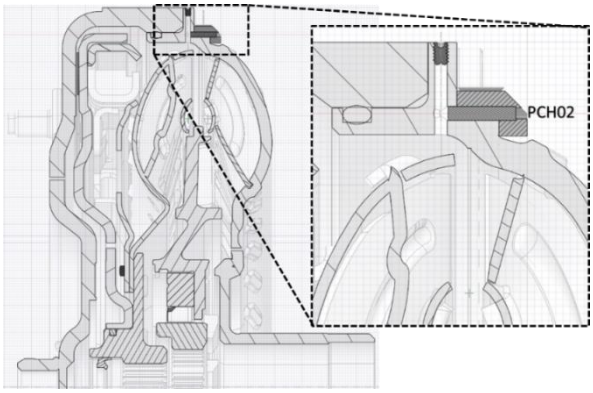

Figure 2-5. Pressure transducer on the outer-most location of the cover.

2.2.2 Clutch & Turbine Instrumentation

The turbine instrumentation was the most challenging to accomplish. A secondary excite induction coil pair was required to supply power. Wiring was routed through several stages and locations inside the torque converter (Figure 2-6).

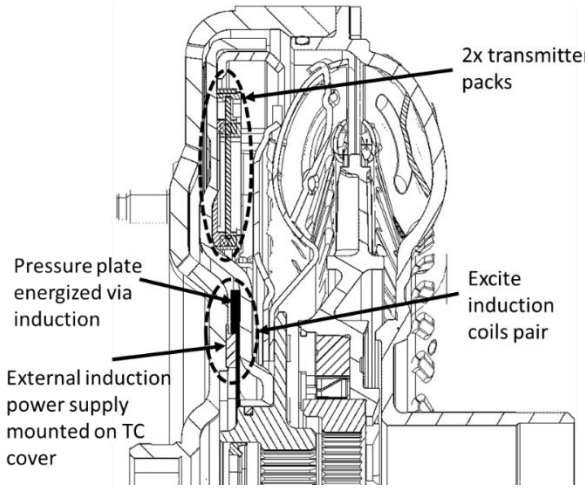

Figure 2-6. Turbine transmitter power supply induction coils.

The transducers mounted straight on the pressure plate get their power directly after the induction coil pair. The transducers mounted on the turbine blade and shell received their power via an array of connector pins (Figure 2-7).

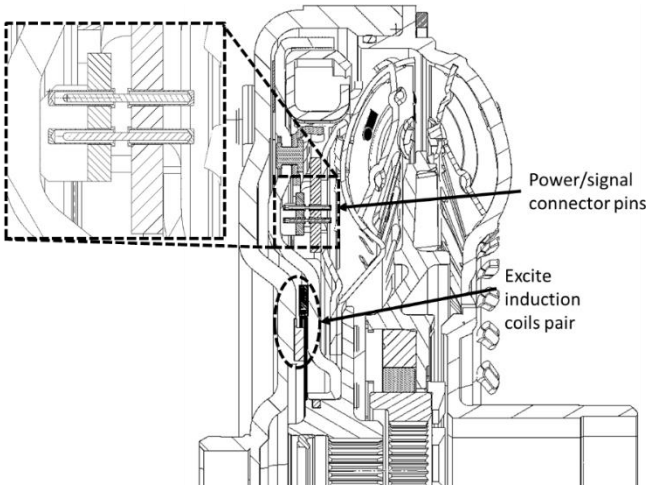

Figure 2-7. Power supply connector pins for the transducers on the turbine blade and shell.

For clutch engagement, the pressure plate must be allowed to move axially. As a result, all connector pins must allow for the axial movement of the pressure plate. To achieve sliding

motion, maintain power, and signal connection, redundancy was needed. A total of 20 connector pin sets were used (Figure 2-8).

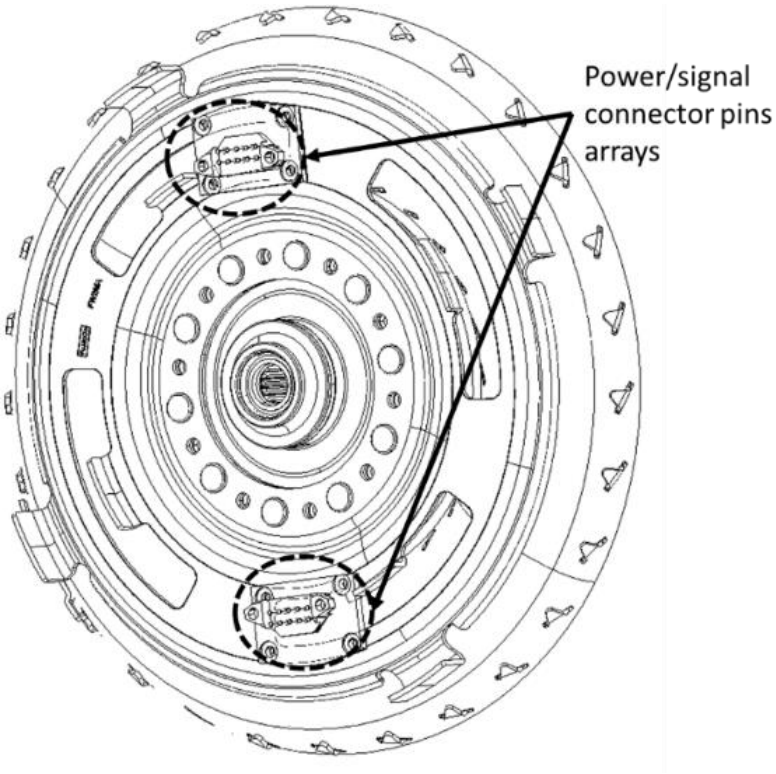

Figure 2-8. Turbine power connector pins arrays.

The transmitter for the turbine transducers was mounted right on the pressure plate as previously seen in Figure 2-6. The resulting turbine signal bounces inside the torque converter. It had to go through two separate slots sealed with three sheets of a Kevlar type antenna material transparent to the bouncing signal (Figure 2-9).

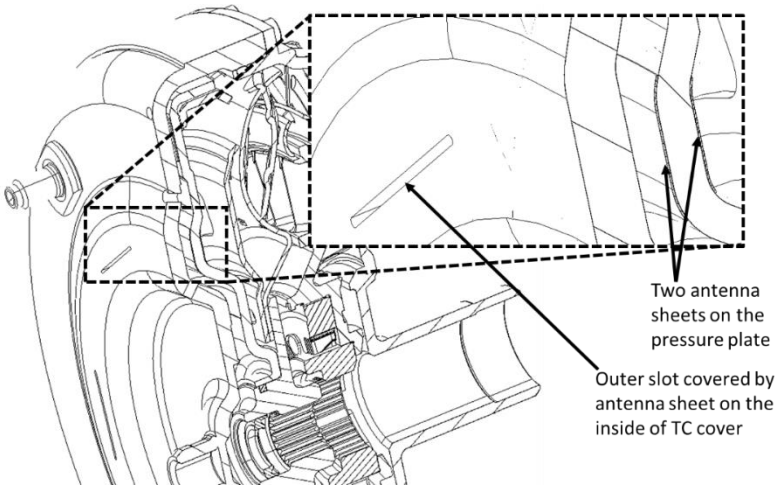

Figure 2-9. Turbine antenna slots on the pressure plate and torque converter cover.

Once the signal is airborne, it is picked up by a series of antennas inside the bell housing. The complexity in the turbine instrumentation resulted in poor quality of the signal with significant dropouts as will be shown in Chapter 4.

The turbine and clutch plate transmitter worked with 15 pressure transducers. Two of the 15 transducers throughout the turbine were Kulite XCEL-072 already discussed. The remaining thirteen of the turbine pressure transducers were low profile Kulite LE-160 series. Their 0.63 MAX thickness, 4.1 mm MAX Diameter and overall 9.5 mm sheet length made them ideal for low flow disruption and provided the ability to mount in tight spaces. With operating range up to 250 psi and 235 degrees Celsius. Their hysteresis and repeatability of up to +/-0.5% FSO. Pressure transducers located throughout the turbine blade and shell totaled 8 while the remaining 7 were located throughout the clutch plate. There were 3 sensors located on the pressure side of several turbine blades. For the CFD model, all transducer monitor points were located on one turbine blade (Figure 2-10).

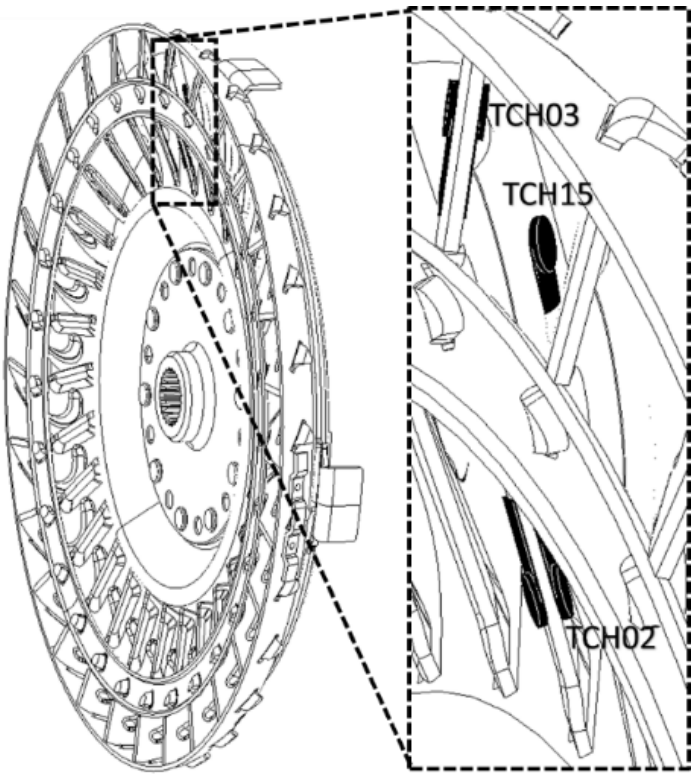

Figure 2-10. Pressure transducers on the pressure side of the turbine blade.

The placement of transducers on the turbine blade aimed at aligning it as much as possible with the mid-span of the blade on the leading, middle and trailing edges. The rib located on the mid-span however, did not allow the mid-chord transducer to be mounted at the mid-span and was shifted slightly.

The next 3 pressure transducers on the turbine blade are located on the suction side. Once more, due to blade rib interference, the sensors were located as close as possible to the mid-span of the blade (Figure 2-11).

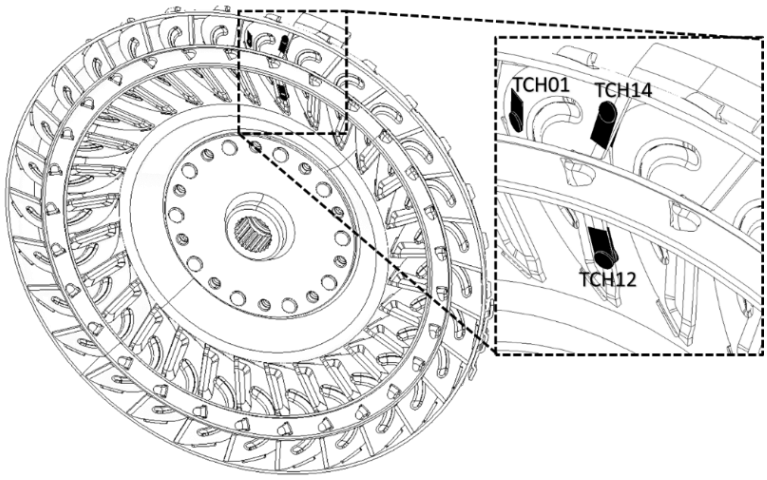

Figure 2-11. Pressure transducers on the suction side of the turbine blade.

The last 2 pressure transducers located on the turbine were installed outside the turbine shell between the turbine and the clutch plate hardware (Figure 2-12).

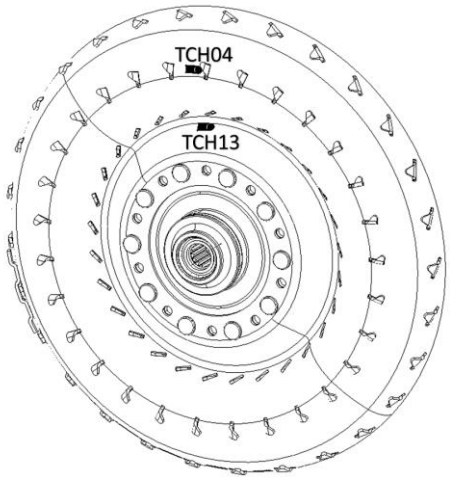

Figure 2-12. Pressure transducers located outside the turbine shell.

A cross section of the torque converter serves best to show the pressure transducers outside the turbine shell exact location (Figure 2-13).

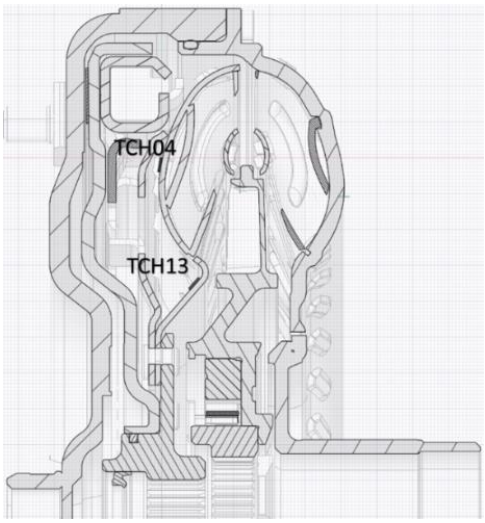

Figure 2-13. Torque converter cross section showing the location of the turbine shell pressure transducers.

All other pressure transducers part of the turbine and clutch plate transmitter were mounted on both sides of the pressure plate (Figure 2-14).

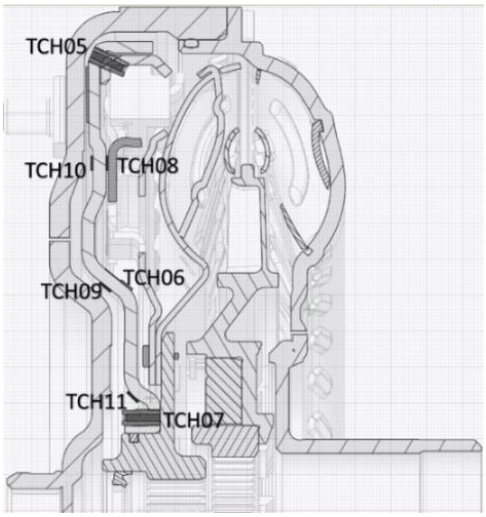

Figure 2-14. Pressure transducers location around the pressure plate.

The innermost pressure transducer between the turbine and the pressure plate is deadheaded when the TCC is OFF because of its location between the clutch plate and the turbine hub.

2.2.3 Stator Instrumentation

The third transmitter in the instrumentation was for the stator transducers. Similar to the turbine, it relied on induction coils to power the sensors via a excite induction coil (Figure 2-15).

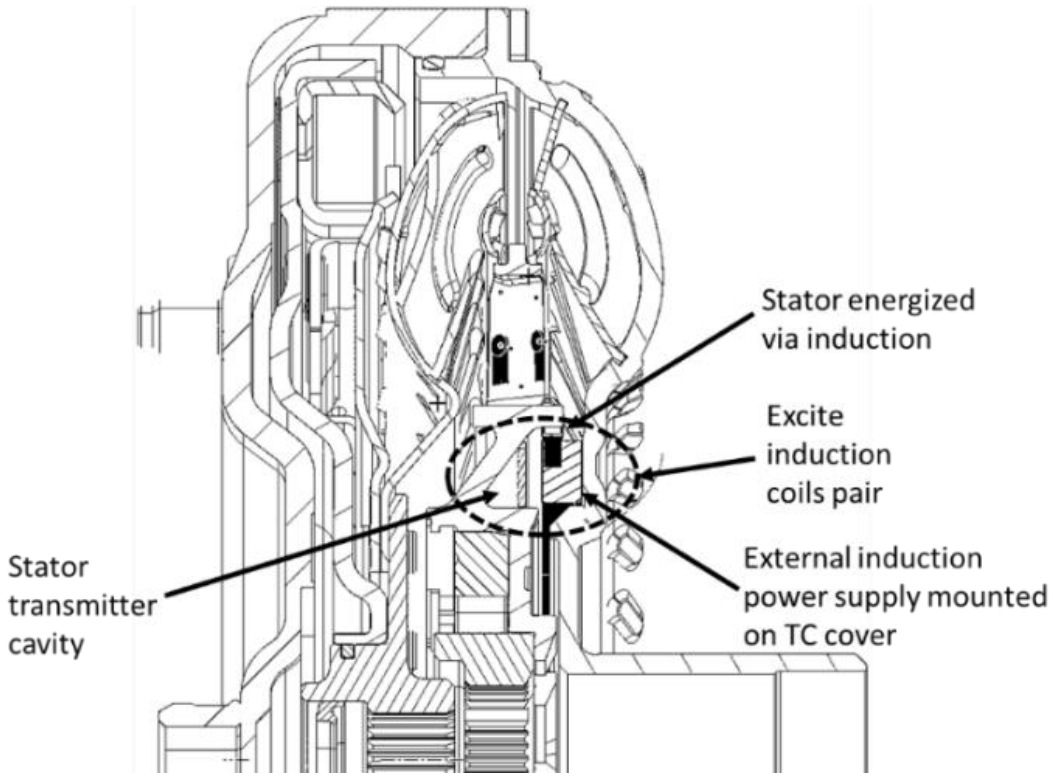

Figure 2-15. Stator power supply induction coil and transmitter.

The signal also bounced inside the torque converter before exiting through slots on the impeller shell that were covered by the Kevlar type induction coil housing (Figure 2-16).

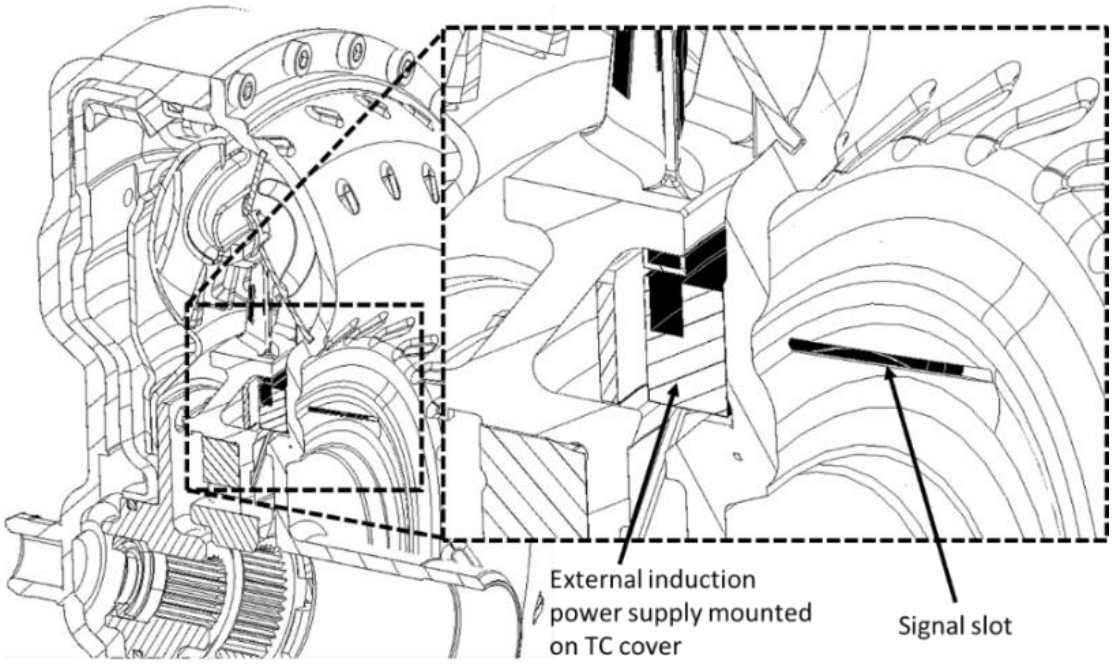

Figure 2-16. Antenna slot for the stator signal located on the impeller shell.

The stator telemetry required an impeller speed of at least 600 rpm to work properly. The quality of the stator signal will be shown in Chapter 4. The stator transmitter handled 7 pressure transducers located on the pressure and suction sides of several stator blades. All the 7 transducers were Kulite LE-160 series transducers covered earlier on the turbine instrumentation section. There were 5 pressure transducers located on the pressure side of the blade (Figure 2-17).

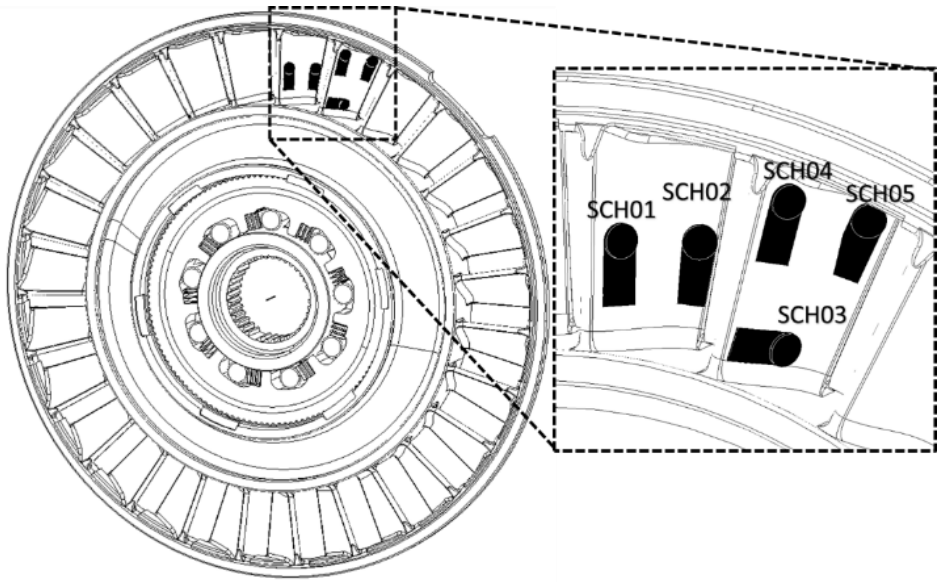

Figure 2-17. Pressure transducers located on the pressure side of the stator blade.

The last 2 stator blade pressure transducers were located on the suction side (Figure 2-18).

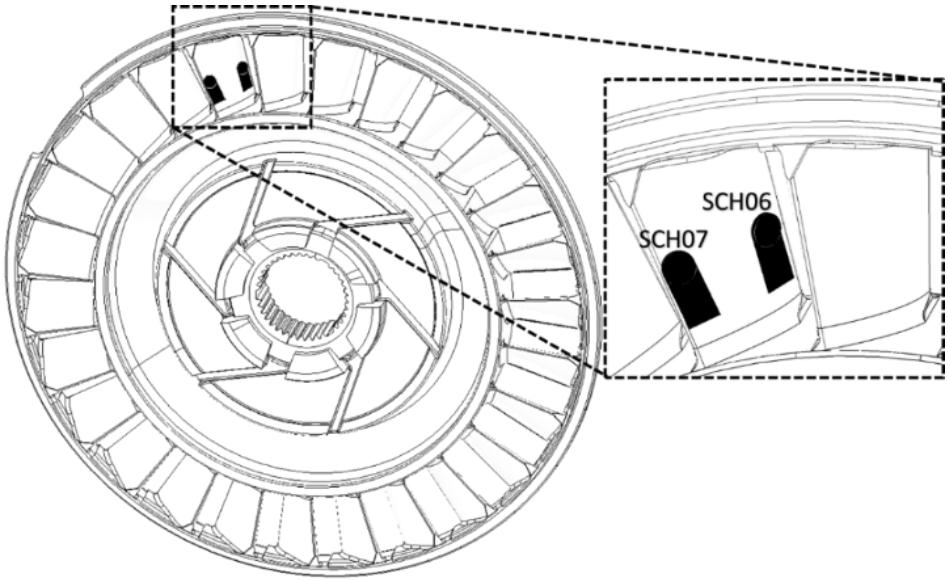

Figure 2-18. Pressure transducers located on the pressure side of the stator blade.

Similar to the turbine pressure transducers, all the CFD monitor points describing the transducer location on the stator were located around 2 blades as shown in the previous

pictures. All the details regarding exact location of the instrumentation for all the cavities can be found Appendix D.

2.3 Laboratory Layout

To test the transmission, a test stand had to be built. The two dynamometers were already available at Michigan Technological University torque converter laboratory. A test fixture was designed and placed between the input and absorbing dynamometers (Figure 2-19).

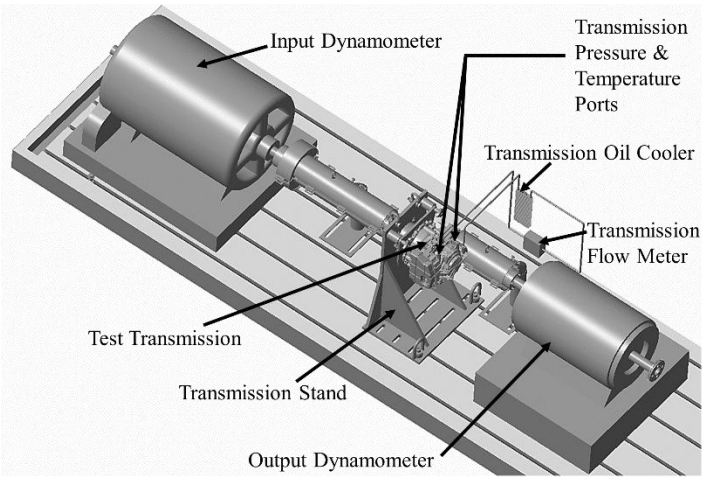

Figure 2-19. Transmission laboratory layout at Michigan Technological University.

Input and output speeds and torques were controlled by an in-house system developed using LabView. Variables monitored but not controlled included, transmission inlet and outlet pressures, temperatures and cooler flow. Transmission shifting and pressure settings were established via a separate transmission control tower supplied by Ford Motor Company. The input dynamometer is a General Electric Direct Current Dynamometer with 285 HP for motoring capabilities and 8000 rpm MAX speed but controlled to never exceed 5500 rpm. For absorbing, a General Electric Alternate Current Dynamometer with 460 HP

absorbing capability was employed. With speed range up to 8000 rpm but restricted to never exceed 5500 rpm. Dynamometer torques measurements were achieved with the use of PCB 1403-02A "pancake" style axial load cell mounted perpendicular to each of the dynamometer's torque arms. Each load cell has a capacity of 2224 N, sensitivity of 0.05 % on the full scale and less than 0.02% hysteresis. Flow measurements were achieved with the use of a Hedland flow meter with 2-19 LPM capability, sensitivity of +/-5% at full scale and repeatability within +/-1%. The operating temperature range of up to 121 degrees Celsius. Temperature measurements were achieved with the use of two K-type thermocouples at the inlet and outlet ports of the transmission. With a wide range of operation for fluids up to 1260 degrees Celsius and +/-0.75% sensitivity/tolerance made them an ideal fit for the project.

Gauge pressure measurements on several transmission locations were obtained with Kulite XTL-123B-190 and XLT123C-190 M series transducers. The transmission channels of interest to the present work included Line, transmission inlet and outlet and torque converter clutch (TCC) release pressures. Calibration curves for all channels of interest are documented in Appendix A.

2.4 Telemetry Specifications

Telemetry system and data acquisition was designed and developed by IR Telemetrics located in Hancock, Michigan. It comprised of three transmitters/receivers combo. Multiplexing thru the three different transmitter was the method of choice for the data acquisition. Each channel was multiplexed in intervals of approximately 1 second. The

impeller transmitter multiplexed through 7 channels in intervals of 1 second each. The turbine transmitter (handling 15 channels) dictated the data acquiring time length. It was found that 60 seconds of data per transmitter was required to ensure at least one multiplexing cycle in the turbine transmitter. The stator transmitter multiplexed through 7 channels in intervals of 1 second each similar to the impeller. Aligning the channels across all three transmitters was not possible and not necessary for the work being considered as part of this investigation. Calibration and more information can be found in Appendix A.

2.5 Data Acquisition System

National Instruments (NI-9178 Chassis) was used in conjunction with NI-9234 modules to acquire the dynamometer data. Telemetry channels were acquired by receivers developed by IR Telemetrics. The telemetry data is automatically calibrated by the receivers. More information on calibration curves for the telemetry data can be seen in Appendix A. The receivers convert frequency data from the transmitters into a digital voltage signal. Sampling frequency is not constant, it is dictated dynamically by the rate of change of the signal being measured and varied between 18 kHz and 20 kHz. Once the telemetry data is acquired, it has to be re-sampled with a constant sampling rate during post-processing. Resampling the data was not necessary for the present work.

2.6 Test Matrix

A variety of speed ratios ranging from 0.1 to 0.9 in increments of 0.1 was run. In order to establish good correlation between the computer simulation and the experiments, steady

state was ensured for all speed ratios tested. Controllability of the dynamometers required all absorbing dynamometer speeds be above 50 rpm. Data for 5th and 6th gear with a 75 N-m input torque and various transmission output speeds were acquired (Table 2-2).

Table 2-2. Targeted test Matrix for 75 N-m Input Torque at Various Output Speeds.

SR [--]	Torque [N-m]	TC Speed [rpm]		Output Dyno Speed [rpm]	
	Impeller	Impeller	Turbine	5th Gear	6th Gear
0.1	75	1700	170	51	68
0.2	75	1652	330	98	132
0.3	75	1604	481	143	192
0.4	75	1557	623	186	249
0.5	75	1509	754	225	301
0.6	75	1461	877	261	350
0.7	75	1413	989	295	395
0.8	75	1521	1216	363	486
0.88	75	1607	1414	421	564
0.9	75	1785	1607	479	641

The final impeller and turbine speeds measures obtained after all speed ratios were tested in the laboratory was then used in the computational fluids dynamics simulation model.

To understand the impact of input torque on the different pressure measurements inside the torque converter, a second set of speed ratios with 50 N-m input torque and various transmission output speeds were run on 6th gear only due to controllability of absorbing dynamometer at low speeds (Table 2-3).

Table 2-3. Targeted test Matrix for 50 N-m Input Torque at Various Output Speeds.

SR [--]	Torque [N-m]	TC Speed [rpm]		Output Dyno Speed [rpm]
	Impeller	Impeller	Turbine	6th Gear
0.1	50	1388	139	55
0.2	50	1349	270	108
0.3	50	1310	393	157
0.4	50	1271	508	203
0.5	50	1232	616	246
0.6	50	1193	716	286
0.7	50	1154	808	322
0.8	50	1242	993	397
0.88	50	1312	1154	461
0.9	50	1457	1312	524

3 Computational Fluids Dynamics (CFD) Model Setup

To establish correlation between documented torque values and the CFD model, a systematic variable elimination exercise was completed. The exercise objective is to determine the optimal variable combination to obtain accurate results. Computational time was a secondary but important objective. The exercise consisted of seven mayor groups of variables. Sixteen variables generated 288 possible CFD analyses (Table 3-1).

Table 3-1. Systematic elimination of variables under study.

Group	**Variables**
Mesh Type	Tetrahedral
	Polyhedral
Mesh Size	Fine-Mesh Size
	Medium-Mesh Size
	Coarse-Mesh Size
Design Features	Ribs
	No ribs
Turbulence Model	k-ε
	k-ω
	Spalart-Allmaras
Solver setup	Coupled
	Standard
Pressure scheme	2nd order
	PRESTO!
Number of iterations	300 iterations
	3000 iterations

Not all 288 analyses were completed. For sake of simplicity, optimal CFD variable combination was established along the way by eliminating analyses that would not yield accurate results. Such a decision was clear once the exercise matrix was being populated. Out of the 288 possible CFD analyses, 24 analyses were enough to obtain optimal CFD setup. The first criteria was given to accuracy of CFD results with test. Computational time was left as secondary criteria but was seen as equally important only after most of the exercise matrix was completed. Definition of the individual variables will be discussed in the following sub-chapters. For the entirety of the simulations completed for this section the ATF was modeled with a density of 790 kg/m^3 and a dynamic viscosity of 0.00623 Pa-s.

3.1 Torque Converter Test Data

Torque converter test data was made available by the sponsors. The data is considered as an ideal torque converter test situation with its allowable manufacture tolerance errors (Figure 3-1).

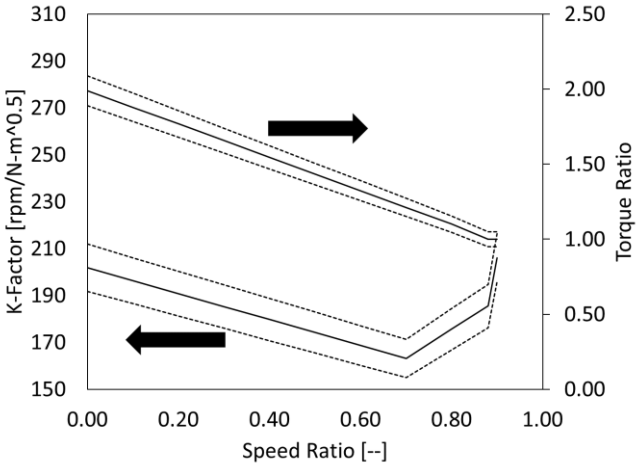

Figure 3-1. Research torque converter test data.

The dashed lines represent the 5% high and low tolerance bands for the respective variables under study. The tolerance bands were used as the determining factors to gage the accuracy of the CFD model.

The torque converter K-Factor and torque ratio are semi-non-dimensional and non-dimensional parameters respectively (Equation 3-1 and Equation 3-2).

$$K - Factor\ \left[\frac{rpm}{(N-m)^{0.5}}\right] = \frac{Impeller\ Speed}{\sqrt{Impeller\ Torque}} \qquad \text{Equation 3-1}$$

$$Torque\ Ratio\ [--] = \frac{Turbine\ Torque}{Impeller\ Torque} \qquad \text{Equation 3-2}$$

Using Figure 3-1, the torque converter torques on each of the three elements could be known for a constant impeller torque of 136 N-m. Only errors for the impeller and turbine torques will be presented throughout the report (Figure 3-2).

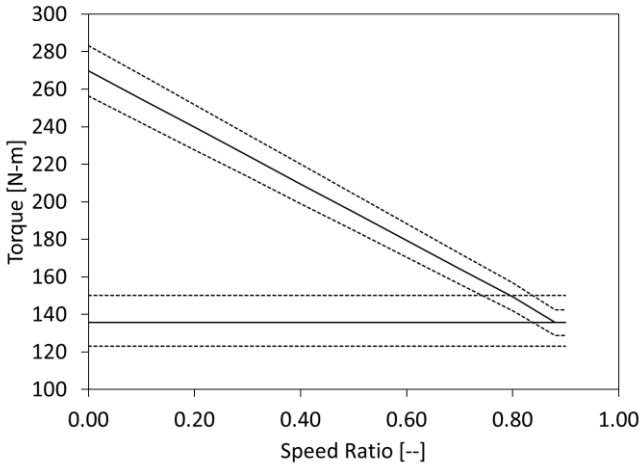

Figure 3-2. Main torque converter torques.

3.2 Variables Under Scrutiny

The variables under consideration (solver type, pressure computational scheme and different turbulence models) must be defined at this point while others are simple enough to define in the subsequent sub-chapters.

The equations of momentum and conservation of mass (continuity) in the investigation must be defined [60]. Starting with the momentum equation for viscous fluid (Equation 3-3).

$$Momentum = \frac{\partial}{\partial t}(\rho\vec{v}) + \nabla \cdot (\rho\vec{v}\vec{v}) = -\nabla\vec{p} + \nabla \cdot (\bar{\bar{\tau}}) + \rho\vec{g} + \vec{F} \qquad \text{Equation 3-3}$$

Fluid density (ρ), velocity vector ($\vec{v}$) and pressure vector ($\vec{p}$) are considered in the momentum equation along with gravitational and external body forces acting on the fluid ($\rho\vec{g}$ and $\vec{F}$). A stress tensor ($\bar{\bar{\tau}}$) accounts for viscous effects in the fluid.

The mass conservation or continuity equation of the investigation must also be defined (Equation 3-4).

$$Continuity = \frac{\partial \rho}{\partial t} + \nabla \cdot (\rho \vec{v}) = 0 \qquad \text{Equation 3-4}$$

The next variable studied that needs definition is the type of solver setup. A standard solver solves the equations of momentum and continuity individually while the coupled solver solves the same equations simultaneously, accelerating convergence but at a memory cost.

A second order accuracy computational scheme for pressure refers to a finite difference method used in solving the pressure variables defined earlier. To better understand the definition, a grid must be defined. For simplicity, a 2D grid is used (Figure 3-3).

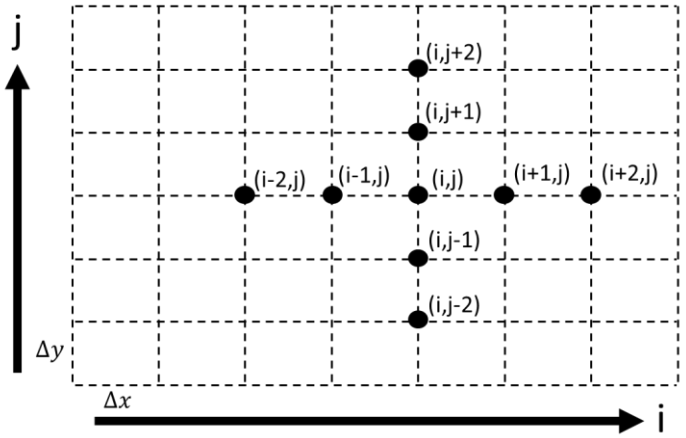

Figure 3-3. 2-D grid example.

The computational scheme used is an upwind or forward difference scheme obtained with a Taylor Expansion Series for points "i+1" and "i+2" truncated at the second term (Equation 3-5 and Equation 3-6).

$$p_{i+1} = p_i + \frac{\Delta x}{1!}\left(\frac{\partial p}{\partial x}\right)_i + \frac{(\Delta x)^2}{2!}\left(\frac{\partial^2 p}{\partial x^2}\right)_i + \cdots$$ Equation 3-5

$$p_{i+2} = p_i + \frac{2\Delta x}{1!}\left(\frac{\partial p}{\partial x}\right)_i + \frac{(2\Delta x)^2}{2!}\left(\frac{\partial^2 p}{\partial x^2}\right)_i + \cdots$$ Equation 3-6

To obtain the first partial derivatives in the momentum and continuity equations previously described, Equation 3-5 and Equation 3-6 must be used to solve by substitution for the first partial derivative term in the "x" direction $\left(\frac{\partial p}{\partial x}\right)$. Let Equation 3-5 be "A" and Equation 3-6 be "B". To solve by substitution, the terms with the partial second derivative must be cancelled out (Equation 3-7).

$$4A - B$$ Equation 3-7

After performing mathematical term groupings and simplifications, the first partial derivative in the "x" direction for the pressure term can be established with a second order accuracy computational scheme (Equation 3-8).

$$\left(\frac{\partial p}{\partial x}\right)_i \approx \frac{4p_{i+1} - p_{i+2} - 3p_i}{2\Delta x}$$ Equation 3-8

Similarly, the partial derivatives in "y" and "z" directions with second order accuracy could be known (Equation 3-9 and Equation 3-10).

$$\left(\frac{\partial p}{\partial y}\right)_j \approx \frac{4p_{j+1} - p_{j+2} - 3p_j}{2\Delta y}$$ Equation 3-9

$$\left(\frac{\partial p}{\partial z}\right)_k \approx \frac{4p_{k+1} - p_{k+2} - 3p_k}{2\Delta z}$$ Equation 3-10

A PRESTO! computational scheme stands for PREssure STaggering Option solving the equations above in a staggered form. Several staggering methods exist, a linear staggering is used to explain the basics. It advances in any given direction half the size of the true element size (Equation 3-11).

$$\left(\frac{\partial p}{\partial x}\right)_{i+\frac{1}{2}} \approx \frac{4p_{i+\frac{3}{2}} - p_{i+\frac{5}{2}} - 3p_{i+\frac{1}{2}}}{2\Delta x} \qquad \text{Equation 3-11}$$

In a similar manner, "y" and "z" directions could be obtained.

Three turbulence models were studied as part of this investigation. They are the three mostly used in industry. In the $k-\varepsilon$ model, the "*k*" stands for turbulence kinetic energy (Equation 3-12), while the "ε" or epsilon stands for turbulence dissipation rate (Equation 3-13) [61].

$$\rho\frac{\partial k}{\partial t} + \rho U_j\frac{\partial k}{\partial x_j} = R_{ij}\frac{\partial U_i}{\partial x_i} - \rho\varepsilon + \frac{\partial}{\partial x_j}\left[\left(\mu + \frac{\mu_T}{\sigma_k}\right)\frac{\partial k}{\partial x_j}\right] \qquad \text{Equation 3-12}$$

The left side of the equation refers to the kinetic energy rate of change of a fluid particle. The term $R_{ij}\frac{\partial U_i}{\partial x_i}$ is a rate of kinetic energy being transferred from the mean flow (U_i) to the turbulence. The right-most term relates the molecular diffusion of "*k*".

$$\rho\frac{\partial \varepsilon}{\partial t} + \rho U_j\frac{\partial \varepsilon}{\partial x_j} = C_{\varepsilon 1}\left(\frac{\varepsilon}{k}\right)R_{ij}\frac{\partial U_i}{\partial x_j} - C_{\varepsilon 2}\rho\left(\frac{\varepsilon^2}{k}\right) + \frac{\partial}{\partial x_j}\left[\left(\mu + \frac{\mu_T}{\sigma_\varepsilon}\right)\frac{\partial \varepsilon}{\partial x_j}\right] \qquad \text{Equation 3-13}$$

In a similar manner, the term on the left of the equation is the dissipation rate of a fluid particle. The $C_{\varepsilon 1}\left(\frac{\varepsilon}{k}\right)R_{ij}\frac{\partial U_i}{\partial x_j}$ term refers to the rate of kinetic energy being transferred into

the turbulence from the mean flow and the right-most term of the equation refers to the molecular diffusion of "ε". Terms $C_{\varepsilon 1}, C_{\varepsilon 2}, \sigma_k$ and σ_ε are constants found in literature [61]. For the standard (most used) form of the $k-\varepsilon$ model, $C_{\varepsilon 1} = 1.44, C_{\varepsilon 2} = 1.92, \sigma_k = 1$ and $\sigma_\varepsilon = 1.3$.

In the $k-\omega$ turbulence model, the "*k*" also stands for kinetic energy and the "ω" or "omega" is the turbulence specific dissipation rate. Both, the $k-\omega$ model and the $k-\varepsilon$ model are 2-equations models. Similarities between both models exist, the "*k*" or turbulence kinetic energy has minor differences in its form (Equation 3-14).

$$\rho\frac{\partial k}{\partial t} + \rho U_j \frac{\partial k}{\partial x_j} = R_{ij}\frac{\partial U_i}{\partial x_i} - \beta^* \rho k\omega + \frac{\partial}{\partial x_j}\left[(\mu + \sigma^* \mu_T)\frac{\partial k}{\partial x_j}\right] \qquad \text{Equation 3-14}$$

Definitions of the terms follow the same pattern as with the $k-\varepsilon$ model.

The turbulence specific dissipation rate "ω" also shares a similar form with the $k-\varepsilon$ model (Equation 3-15).

$$\rho\frac{\partial \omega}{\partial t} + \rho U_j \frac{\partial \omega}{\partial x_j} = \alpha\left(\frac{\omega}{k}\right)R_{ij}\frac{\partial U_i}{\partial x_j} - \beta\rho\omega^2 + \frac{\partial}{\partial x_j}\left[(\mu + \sigma\mu_T)\frac{\partial \omega}{\partial x_j}\right] \qquad \text{Equation 3-15}$$

In a similar way, $\alpha, \beta, \beta^*, \sigma^*,$ and σ are constants found in literature [62].

The standard $k-\omega$ model constant values are, $\alpha = 0.52, \beta = 0.072, \beta^* = 0.09, \sigma^* = 0.5,$ and $\sigma = 0.5$.

The last of the three turbulence models studied is a one-equation model referred to as Spalart-Allmaras model [63].

The commercially available software uses the following variation (Equation 3-16).

$$\frac{\partial}{\partial t}(\rho\tilde{\nu}) + \frac{\partial}{\partial x_i}(\rho\tilde{\nu}u_i) = G_\nu + \frac{1}{\sigma_{\tilde{\nu}}}\left[\frac{\partial}{\partial x_j}\left\{(\mu_t + \rho\tilde{\nu})\frac{\partial\tilde{\nu}}{\partial x_j}\right\} + C_{b2}\rho\left(\frac{\partial\tilde{\nu}}{\partial x_j}\right)^2\right] - Y_\nu + S_{\tilde{\nu}}$$

Equation 3-16

The left term is the rate in which the turbulent viscosity changes for a particle. The explanation of the remaining terms, coefficients and constants can be found in Appendix G along with the effect on torque and pressure by modifying some of the coefficients.

3.3 Mesh Type Studies

A polyhedral mesh is created out of tetrahedral elements by combining neighboring elements to form a polyhedral one. Mesh consisting of tetrahedral and polyhedral cells were considered for the investigation (Figure 3-4).

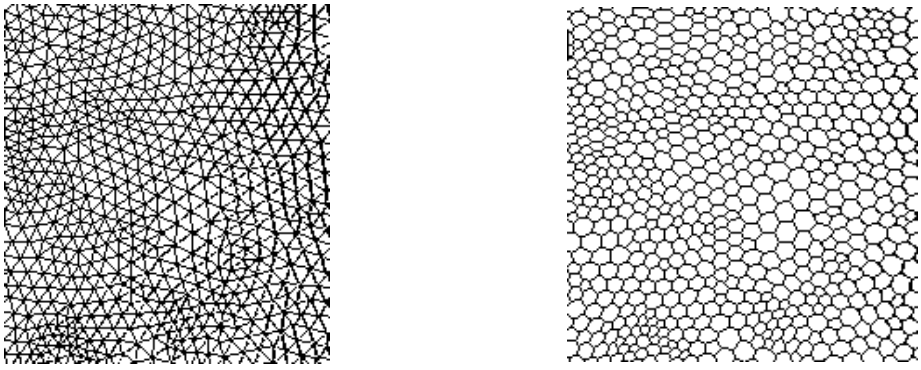

(a) (b)

Figure 3-4. Tetrahedral (a) and polyhedral (b) elements studied.

The model parameters studied are tabulated below (Table 3-2).

Table 3-2. Mesh type studies CFD model definition.

Polyhedral	Tetrahedral
6,447,394 elements	32,828,990 elements
Without blade ribs	Without blade ribs
3000 iterations	3000 iterations
$k-\varepsilon$ turbulence model	$k-\varepsilon$ turbulence model
Standard solver setup	Standard solver setup
2nd order pressure	2nd order pressure
66 hours to solve 11 speed ratios (SR's)	99 hours to solve 11 speed ratios (SR's)

The result of a polyhedral conversion is a reduced element count, which will solve quicker but with less than desirable accuracy (Figure 3-5).

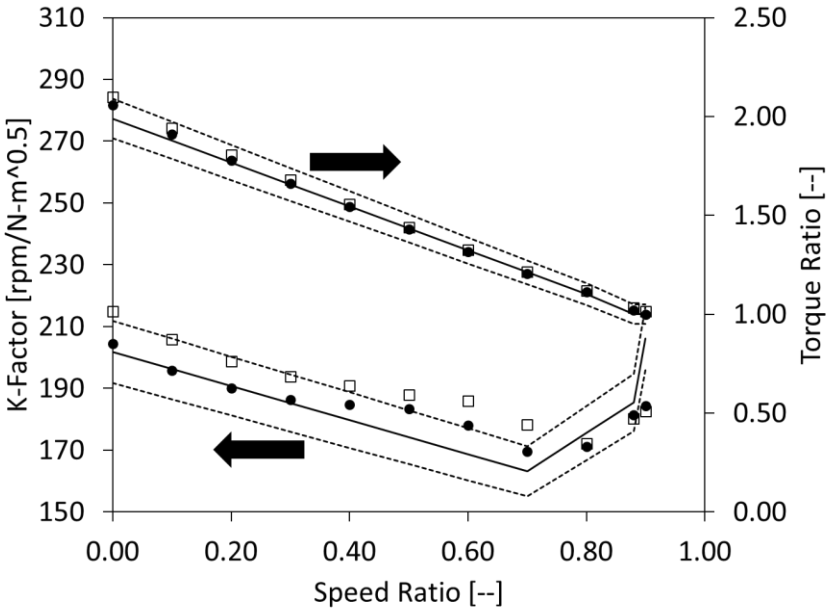

Figure 3-5. Polyhedral CFD (squares), tetrahedral CFD (dots) compared to test (solid) with +/-5% tolerance bands (dashed).

The CFD results showed the tetrahedral mesh within the boundaries of documented test data. A look at the impeller and turbine torques maximum errors from test demonstrate tetrahedral superiority (Table 3-3).

Table 3-3. Mesh type tabulated torque discrepancies from test.

Polyhedral Max error		Tetrahedral Max Error	
Impeller	Turbine	Impeller	Turbine
18%	18%	10%	11%
RMSE 14%	RMSE 14%	RMSE 9%	RMSE 10%

A graphical view of the results show advantages of tetrahedral mesh type (Figure 3-6).

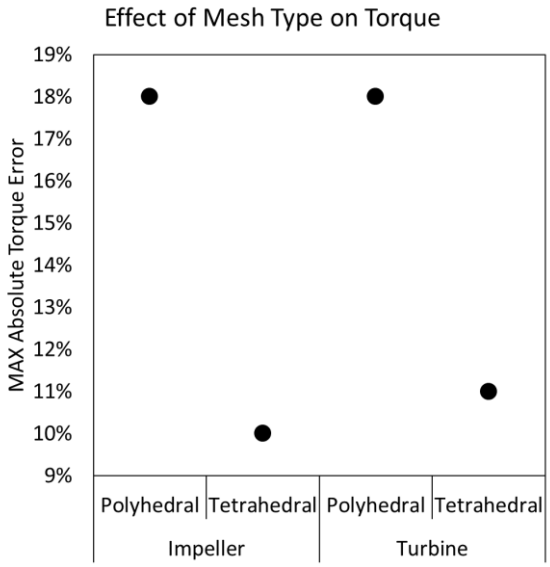

Figure 3-6. Mesh type effect plot between tetrahedral and polyhedral meshes.

Based on the obtained results, polyhedral elements were not utilized for any further analysis. Eliminating polyhedral mesh from the rest of the experiments eliminated 143 of the 288 experiments. In order to achieve comparable accuracy with polyhedral elements,

an excessive amount of tetrahedral elements would need to be converted to polyhedral ones, resulting in solution times that will most likely be back in 99 hours range. The remaining analyses studied, used different tetrahedral elements sizes that will be explained in the following sub-chapters.

3.4 Design Features Studies

Mass producing torque converters in the automotive industry consist of mainly stamping methods. Usually, torque converter impellers and turbines in the automotive industry require the use of ribs along the blade mid-span to stiffen the blades (Figure 3-7).

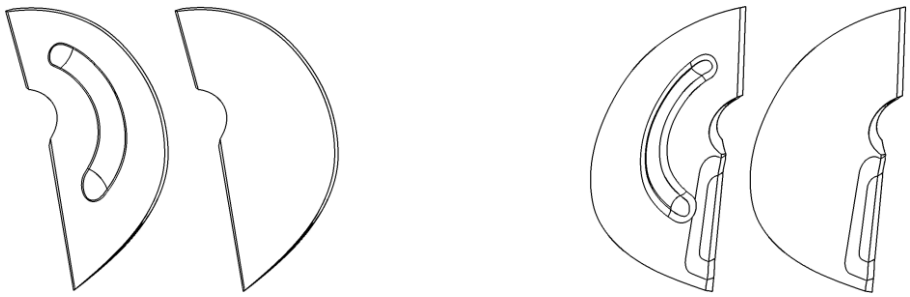

(a) (b)

Figure 3-7. Blade designs with and without ribs for impellers (a) and turbines (b).

The use of ribs add complexity to the CFD model. A study was performed to examine the impact of such blade ribs on the CFD accuracy of results. Gaps due to blade tangs commonly used to attach blades to the shell and core were not modeled since brazing operations will fill up those gaps. Several scenarios and variable combinations were studied but only one presented here (Table 3-4).

Table 3-4. Design features study CFD model definition.

With blade ribs	Without blade ribs
32,978,477 elements	32,828,990 elements
Tetrahedral	Tetrahedral
3000 iterations	3000 iterations
$k-\varepsilon$ turbulence model	$k-\varepsilon$ turbulence model
Standard solver setup	Standard solver setup
2nd order pressure	2nd order pressure
99 hours to solve 11 SR's	99 hours to solve 11 SR's

Although very similar results between the analyses presented here, overall, for all scenarios (presented as well as not shown), the maximum error discrepancy between CFD with or without ribs was around 1% between them (Figure 3-8).

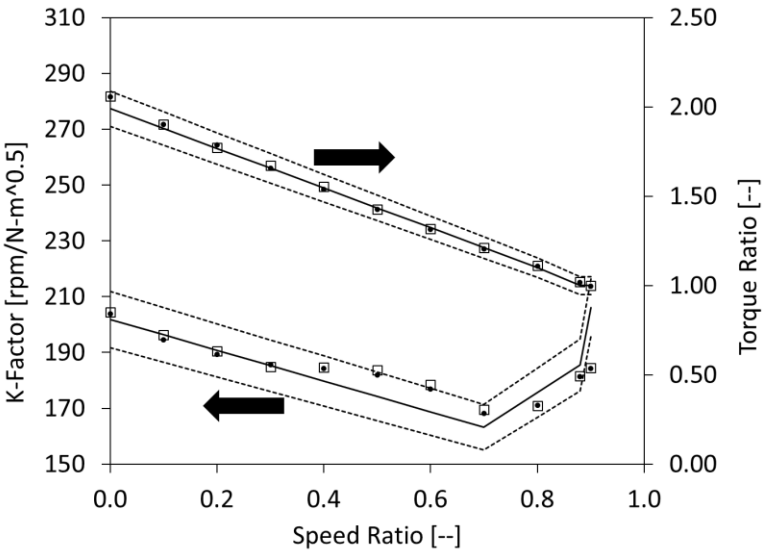

Figure 3-8. CFD without ribs (squares), CFD with ribs (dots) compared to test (solid) with +/-5% tolerance bands (dashed).

The results shown above makes it difficult to gage the difference between a CFD model with or without ribs. A tabulated view will of the maximum errors for impeller and turbine torque show that a CFD model with blade ribs yields results closer to test data (Table 3-5).

Table 3-5. Design features tabulated torque discrepancies from test.

With ribs Max Error		Without ribs Max Error	
Impeller	Turbine	Impeller	Turbine
9%	10%	10%	11%
RMSE 9%	RMSE 9%	RMSE 9%	RMSE 10%

The effect plot can help visualize the results for the design feature test (Figure 3-9).

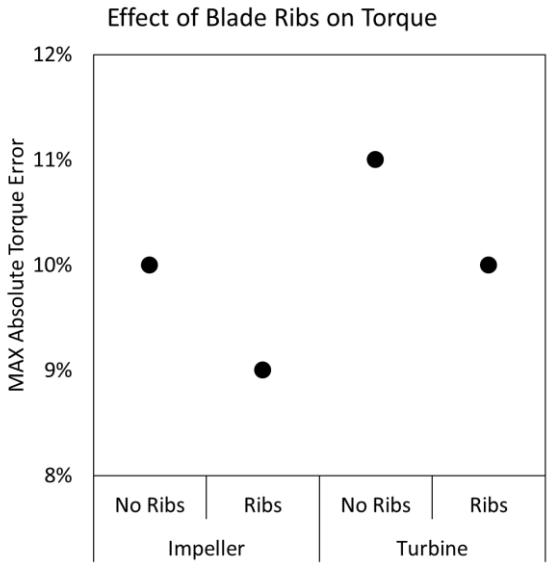

Figure 3-9. Design features effect plot on CFD maximum torque error results.

Although minor differences between the tested design features, a CFD model considering the addition of ribs for the torque converter under study provided results that are more accurate and it is recommended for final CFD model set ups. The results also demonstrate

the ability of the CFD to capture small design features. Torque converter manufacturing methods vary across sizes and industry. Some cast torque converters create mold parting lines on different locations of the blade surfaces. If parting lines are present during manufacture, a representation of the parting lines must be considered during development.

3.5 Mesh Density Studies

Mesh density was considered for the investigation. The elements size for cells in contact with walls is half the size of the elements used for the bulk of the fluid zones not in contact with the walls [64]. Three mesh sizes were studied, fine, medium and coarse (Figure 3-10).

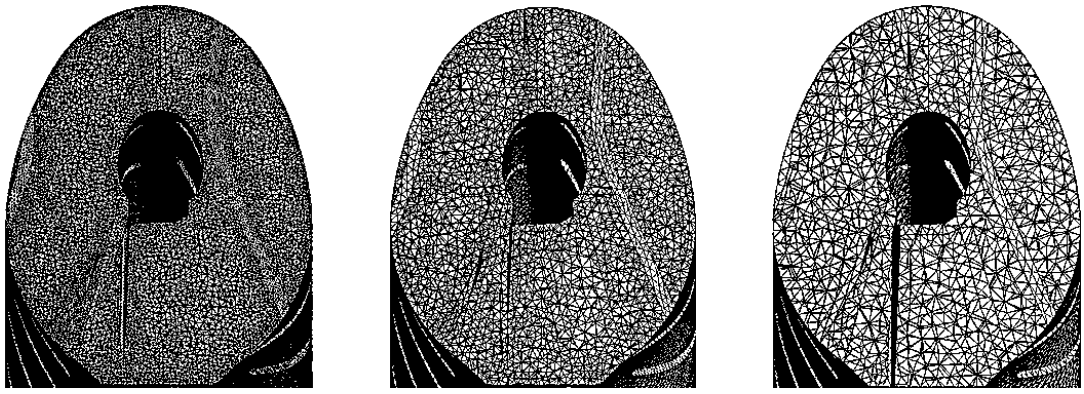

(a) (b) (c)

Figure 3-10. Studied fine (a), medium (b) and coarse (c) mesh.

A fine mesh consisted of 1 mm elements on the bulk fluid while elements in contact with walls was set to 0.5 mm. A medium size mesh consisted of elements measuring 2.5 mm for the bulk of the fluid zone with 1.25 mm elements in contacts with walls. The coarse mesh element size was set to 4 mm for the bulk of the fluid zone with 2 mm sized elements in contact with all walls. Details of the study are best seen tabulated (Table 3-6).

Table 3-6. Mesh density studies CFD model definition.

Fine	Medium	Coarse
32,828,990 elements	3,310,295 elements	935,703 elements
Without blade ribs	Without blade ribs	Without blade ribs
Tetrahedral	Tetrahedral	Tetrahedral
3000 iterations	3000 iterations	3000 iterations
$k-\varepsilon$ turbulence	$k-\varepsilon$ turbulence	$k-\varepsilon$ turbulence
Standard solver setup	Standard solver setup	Standard solver setup
2nd order pressure	2nd order pressure	2nd order pressure
99 hours to 11 SR's	11 hours to solve 11 SR's	2.75 hours to solve 11 SR's

There is a clear difference between the CFD modeled with different mesh sizes and the documented test results (Figure 3-11).

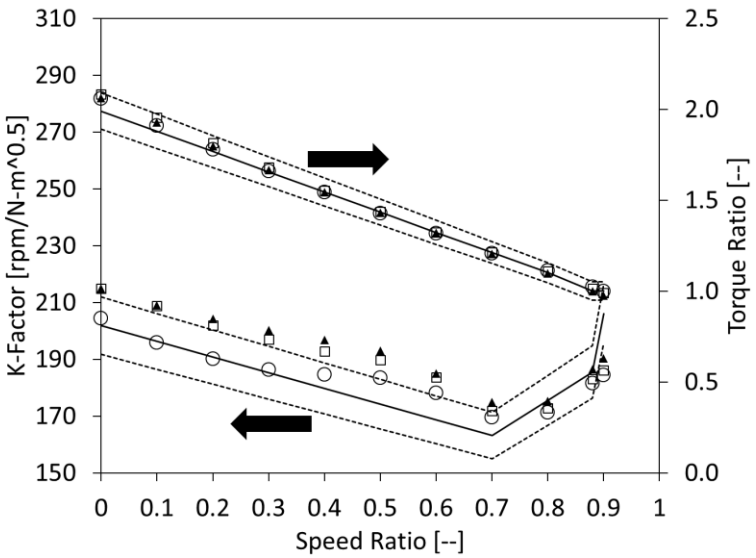

Figure 3-11. CFD fine mesh (circles), CFD medium mesh (squares) and CFD with coarse mesh (triangles) compared to test (solid) with +/-5% tolerance bands (dashed).

The results show large discrepancy between tested torque data and the three CFD mesh sizes (up to 19% at SR=0.5). The difference in impeller and turbine torque between medium and coarse sizes mesh showed only 3% difference (Table 3-7).

Table 3-7 Mesh size tabulated torque discrepancies from test.

Fine mesh Max Error		Medium mesh Max Error		Coarse mesh Max Error	
Impeller	Turbine	Impeller	Turbine	Impeller	Turbine
10%	11%	16%	16%	18%	19%
RMSE 9%	RMSE 10%	RMSE 13%	RMSE 12%	RMSE 14%	RMSE 13%

The fine mesh showed smaller impeller and turbine torque errors followed by the medium mesh (Figure 3-12).

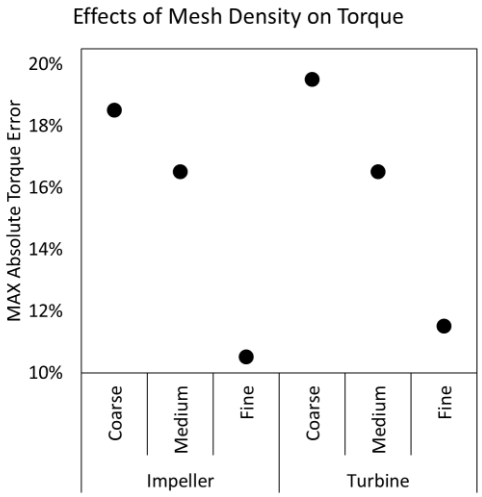

Figure 3-12. Mesh density effect plot for absolute impeller and turbine errors.

So far, fine mesh yields results that are more accurate but the remaining variable combinations are assumed independent of mesh size and will be completed using medium and coarse mesh sizes. Coarse and medium mesh are faster while demonstrating behavior

and trends. With an optimized medium size mesh, solution time and torque prediction errors reduced. It is always best to start with a coarse mesh to understand trends in the result. A coarse mesh can provide a glimpse of the final K-Factor trend in under 3 hours. The implications in such accelerated solution time for a simulation is significant. Once better knowledge of the torque converter architecture is available, subsequent analyses including mesh refinement studies will need to be completed. This approach was used in the present investigation to some extent as will be seen next.

3.6 Turbulence Models Studies

Three turbulence models were studied. Spalart-Allmaras, $k-\varepsilon$ and $k-\omega$. To test accuracy and reduce computational time, a coarse mesh was used for the three turbulence studies (Table 3-8).

Table 3-8. Turbulence model studies CFD model definition.

$k-\varepsilon$	$k-\omega$	Spalart-Allmaras
Coarse	Coarse	Coarse
935,703 elements	935,703 elements	935,703 elements
Without blade ribs	Without blade ribs	Without blade ribs
Tetrahedral	Tetrahedral	Tetrahedral
3000 iterations	3000 iterations	3000 iterations
Standard solver setup	Standard solver setup	Standard solver setup
2nd order pressure	2nd order pressure	2nd order pressure
2.75 hrs to solve 11 SR's	2.75 hrs to solve 11 SR's	2.75 hrs to solve 11 SR's

Results obtained did not show a large difference between all three turbulence models but Spalart-Allmaras raised as the best of the three across the converter drive speed ratio range (SR=0 to SR=0.8) followed by $k-\varepsilon$ (Figure 3-13).

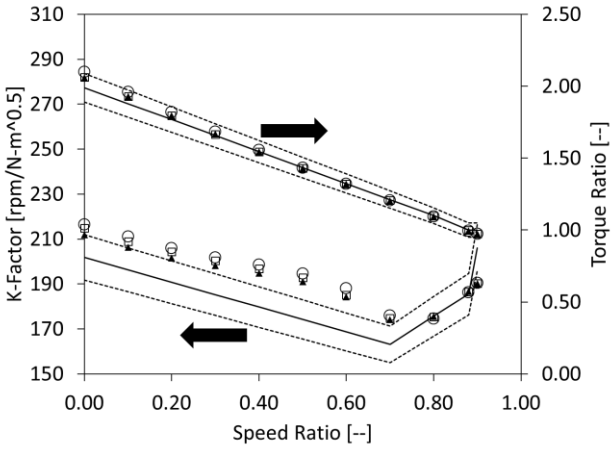

Figure 3-13. Standard solver CFD with three turbulence models, $k-\omega$ (circles), $k-\varepsilon$ (squares) and Spalart-Allmaras (triangles) compared to test (solid) with +/- 5% tolerance bands (dashed).

Discrepancy from test is best observed in a tabulated form (Table 3-9).

Table 3-9. Turbulence models tabulated torque errors from test with standard solver.

$k-\varepsilon$		$k-\omega$		Spalart-Allmaras	
Impeller	Turbine	Impeller	Turbine	Impeller	Turbine
18%	19%	20%	20%	17%	17%
RMSE 14%	RMSE 13%	RMSE 15%	RMSE 14%	RMSE 12%	RMSE 12%

Based on the tested turbulence models, Spalart-Allmaras provided results closer to tested data (Figure 3-14).

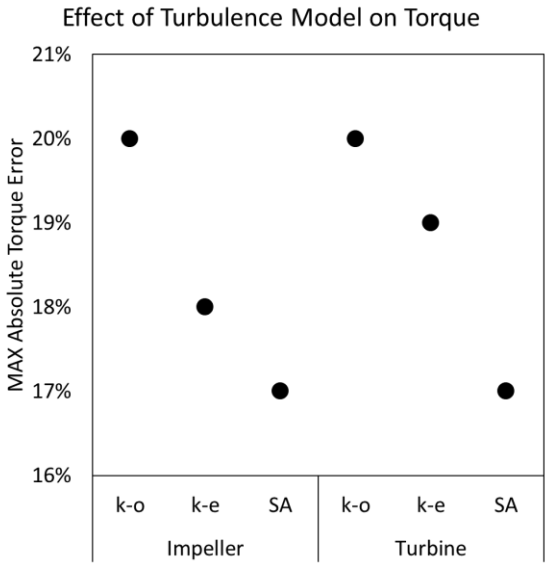

Figure 3-14. Turbulence model effect on impeller and turbine torque.

The significant drop in error levels obtained with the Spalart-Allmaras's turbulence model is of great importance in the torque converter analysis area. Spalart-Allmaras's one-equation model is not used widely in torque converter simulation. Further studies for complex, three dimensional turbomachinery especially in torque converter simulation with different geometries and applications should be done to understand if the reduced error levels are repeatable.

3.7 Solver Setup Studies

To take full advantage of the variable study completed in the previous section with a standard solver and to determine repeatability of the Spalart-Allmaras's one-equation model to some extent, a coarse mesh with the same three different turbulence models explained earlier were run with a coupled solver set up (Table 3-10).

Table 3-10. Solver set up studies CFD model definition.

$k-\varepsilon$	$k-\omega$	Spalart-Allmaras
Coarse	Coarse	Coarse
935,703 elements	935,703 elements	935,703 elements
Without blade ribs	Without blade ribs	Without blade ribs
Tetrahedral	Tetrahedral	Tetrahedral
3000 iterations	3000 iterations	3000 iterations
Coupled solver setup	Coupled solver setup	Coupled solver setup
2nd order pressure	2nd order pressure	2nd order pressure
9 hours to solve 11 SR's	9 hours to solve 11 SR's	9 hours to solve 11 SR's

The coupled solver is more accurate than the standard but at a higher computational time cost (three times higher) (Figure 3-15).

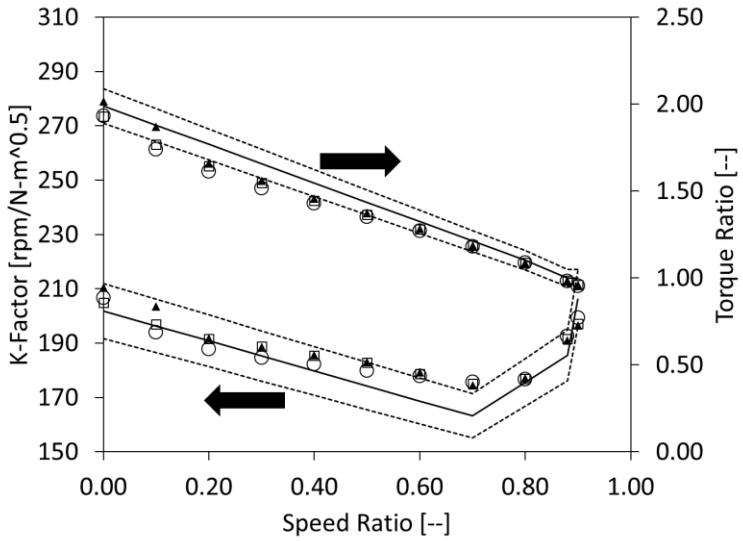

Figure 3-15. Coupled solver CFD with three turbulence models, $k-\omega$ (circles), $k-\varepsilon$ (diamonds) and Spalart-Allmaras (triangles) compared to test (solid) with +/-5% tolerance bands (dashed).

By solving momentum and continuity equations simultaneously, accuracy is improved, number of iterations to converge reduces but solution time per iteration along with computing memory requirements increases. A comparison between the previous section plot and the current one shows the coupled solver as the best choice. It pulls the data down towards the K-Factor test data but unfortunately, the torque ratio is pulled down away from the tested data. Discrepancies between the three models with coupled solver is seen tabulated next (Table 3-11).

Table 3-11. Turbulence models tabulated torque discrepancies from test with coupled solver.

	$k-\varepsilon$		$k-\omega$		Spalart-Allmaras	
Solver	Impeller	Turbine	Impeller	Turbine	Impeller	Turbine
Standard	18%	19%	20%	20%	17%	17%
RMSE	14%	13%	15%	14%	12%	12%
Coupled	13%	15%	14%	16%	16%	14%
RMSE	7%	10%	7%	9%	8%	10%

The results showed a Spalart-Allmaras performed better on both solver type set-ups yielding lower impeller and turbine torque MAX errors each time (Figure 3-16).

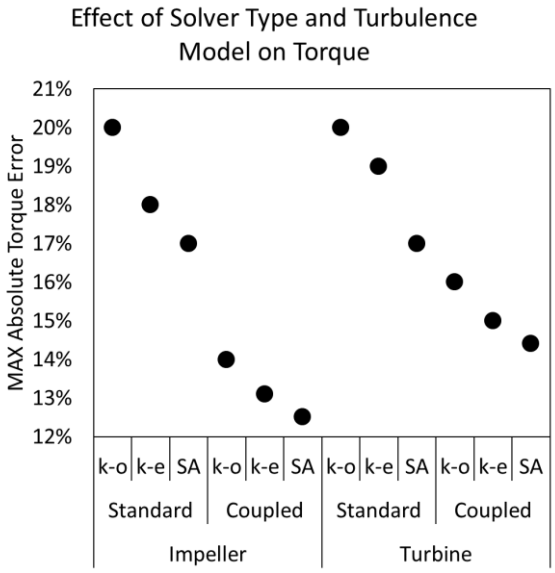

Figure 3-16. Solver type effect on impeller and turbine torque.

CFD errors compared to test data showed Spalart-Allmaras as slightly more accurate of the three analyses again. The coupled solver is more accurate (yet time consuming) than a standard solver. The implications of this understanding are significant. The dramatic reduction in maximum errors with the use of a couple solver in combination with the Spalart-Allmaras's one-equation turbulence model are too advantageous to ignore. It is now confirmed that at least for the torque converter under study, Spalart-Allmaras's turbulence model yields torque predictions that are the most accurate of the three methods studied. It is now recommended that in future studies, the turbulence model be studied further with a variety of torque converter shapes and sizes. Once such studies are done, repeatability of the method in producing accurate results will be fully understood.

3.8 Pressure Computational Scheme

Two pressure numerical schemes were studied as a recommendation from the software vendor. The PRESTO! scheme is better equipped for capturing highly three-dimensional shapes typical of turbomachinery as explained earlier. To understand effects in torque prediction between the two pressure computational schemes, the coarse mesh with ribs was used in this next experiment (Table 3-12).

Table 3-12. Pressure Scheme set up studies CFD model definition.

2nd order pressure	PRESTO! pressure scheme
With blade ribs	With blade ribs
Coarse mesh	Coarse mesh
954,742 elements	954,742 elements
Tetrahedral	Tetrahedral
3000 iterations	3000 iterations
Spalart-Allmaras turbulence model	Spalart-Allmaras turbulence model
Coupled solver setup	Coupled solver setup
9 hours to solve 11 SR's	9 hours to solve 11 SR's

The 2nd order computational scheme for pressure showed more accurate K-Factor than PRESTO! (Figure 3-17).

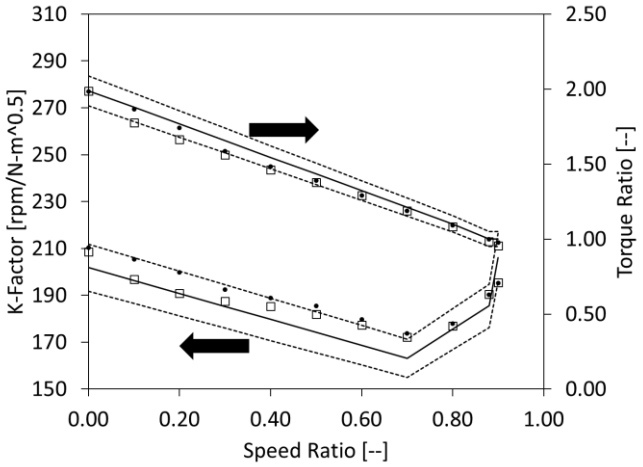

Figure 3-17. CFD results for 2nd order computational scheme for pressure (squares), CFD results for PRESTO! computational scheme for pressure (dots) compared to test (solid) with +/-5% tolerance bands (dashed).

Demonstrating 2nd order scheme superiority over PRESTO!, a look at the impeller and turbine torques is necessary (Figure 3-18).

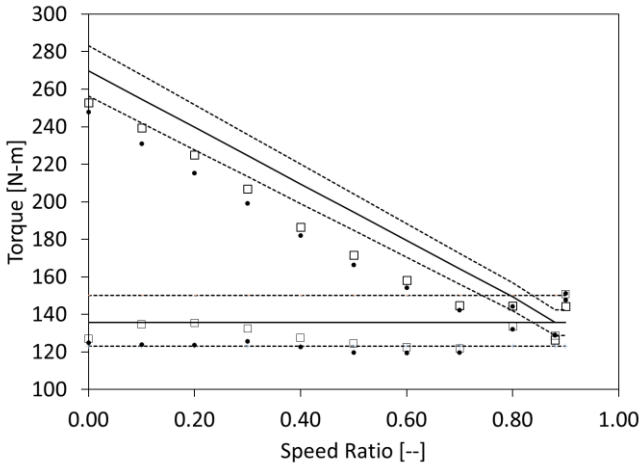

Figure 3-18. CFD torques for 2nd order scheme (squares) and PRESTO! scheme (dots) compared to test (solid) with torque tolerance bands (dashed).

The 2nd order computational scheme shifted the CFD results towards the tested ones for impeller and turbine torques making it a better choice over the PRESTO! scheme. Tabulated results shows the magnitude of the discrepancy with test (Table 3-13).

Table 3-13. Pressure schemes models tabulated torque discrepancies from test (semi-non-dimensional).

2nd order pressure MAX Error		PRESTO! MAX Error	
Impeller	Turbine	Impeller	Turbine
10 %	12%	12%	14%
7%	9%	9%	11%

The results seen in this particular experiment are surprising and unexpected. A reduction in maximum torque errors of up to 2% with the 2nd order scheme merits further analysis and understanding. The results of the pressure computational scheme shows the 2nd order to be superior over the PRESTO! for the torque converter under study (Figure 3-19).

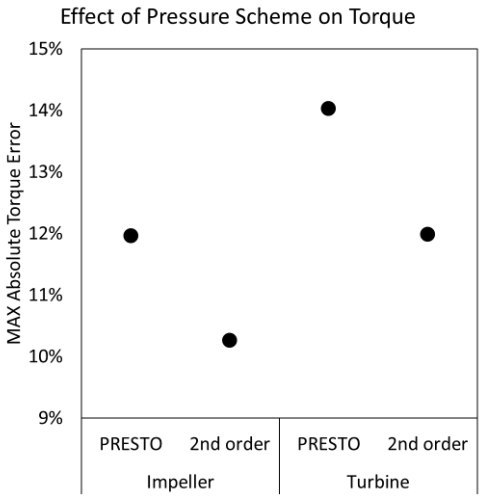

Figure 3-19. Effect of pressure computational scheme on impeller and turbine torques for the coarse mesh.

The clear target at this point should be mesh size. If all other variables with the exception of mesh size are left unchanged, PRESTO! computational scheme becomes the method of choice for finer meshes (Figure 3-20).

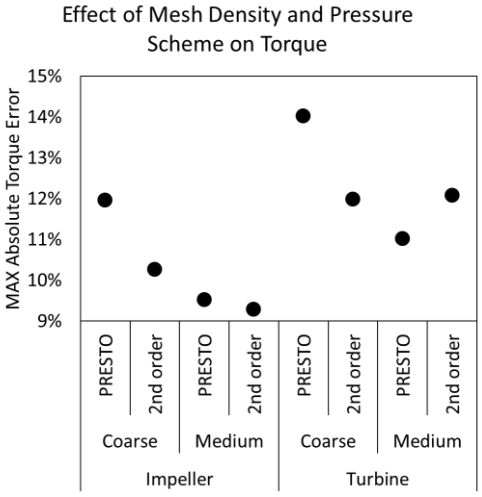

Figure 3-20. Effect of mesh size on pressure computational scheme results.

The further reductions in maximum turbine torque errors obtained when combining medium sized elements with PRESTO! pressure computational scheme makes it the method of choice for the next study targeting number of iterations.

3.9 Number of Iterations Studies

Unfortunately, knowing when to stop a simulation or which speed ratio requires the largest number of iterations to converge can only be done after the fact. For all the simulations ran for the present investigation, only the stall speed ratio required the largest number of iterations to converge. In order to tackle the secondary goal of this investigation (reduced computational time), number of iterations was a clear and easy variable to target.

The number of iterations studied was 300 and 3000. Five different combinations of variables with 300 and 3000 iterations were studied. Running the fine mesh 3000 iterations took 9 hours per speed ratio, reducing the number of iterations to 2500 would have taken 7.5 hours. Still not a very desirable solution time. Simulation for the torque converter stall speed ratio (SR=0) with fine mesh was seen as the speed ratio taking the longest to reach convergence. So far, it has been shown that errors could be reduced by optimizing some of the variables when using either coarse or medium mesh sizes. It has also been shown the reduced solution times, resulting from variable combination optimization and mesh sizes. For the fine mesh for example, 3000 iterations were run but convergence could have been established after only 2500 iterations (Figure 3-21).

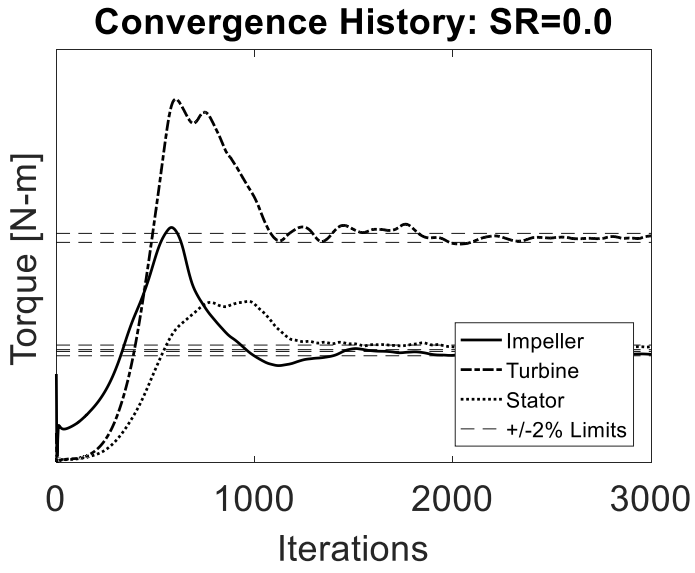

Figure 3-21. Solution convergence for fine mesh with 3000 iterations (SR=0.0).

To better understand the convergence history for the different variable combinations seen so far, a sample case could be studied in detail with the characteristics tabulated below (Table 3-14).

Table 3-14. Number of iterations set up studies CFD model definition.

300 iterations	3000 iterations
With blade ribs	With blade ribs
Tetrahedral	Tetrahedral
PRESTO! pressure scheme	PRESTO! pressure scheme
Medium size mesh	Medium size mesh
3,338,636 elements	3,338,636 elements
Spalart-Allmaras turbulence model	Spalart-Allmaras turbulence model
Coupled solver setup	Coupled solver setup
3.3 hours to solve 11 SR's	33 hours to solve 11 SR's

For all other cases studied with either medium or coarse size mesh, 3000 iterations were run but convergence could have been considered reached after less than 300 (Figure 3-22).

(a)

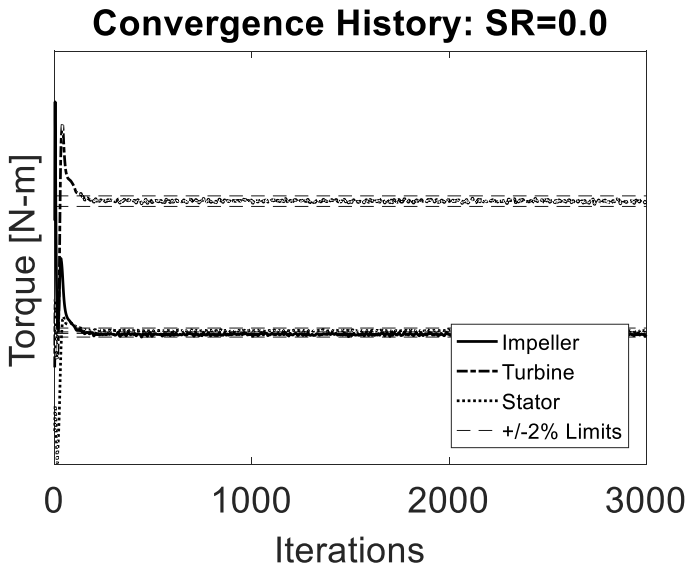

(b)

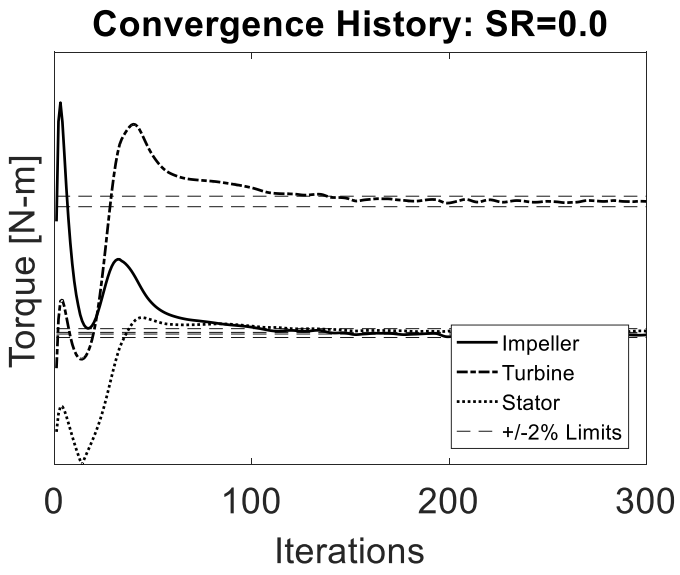

Figure 3-22. Convergence traces for 3000 iterations (a) and 300 iterations (b).

Comparing results for the two cases did not show large discrepancy (Figure 3-23).

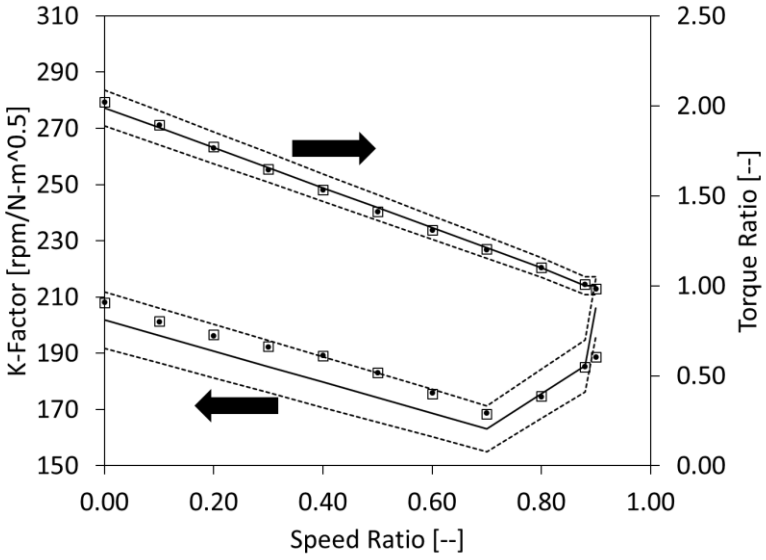

Figure 3-23. CFD results for 300 (squares) and 3000 iterations (dots) compared to test (solid) with +/-5% tolerance bands (dashed).

A look at the tabulated results show the similarity between the studies concerning number of iterations (Table 3-15).

Table 3-15. Iterations studied models tabulated torque discrepancies from test.

300 iterations Max Error		3000 iterations Max Error	
Impeller	Turbine	Impeller	Turbine
9.5%	10.8%	9.8%	11.0%
RMSE 9%	RMSE 8%	RMSE 9%	RMSE 9%

The number of iteration study showed that with the proper variable combination, convergence is achieved faster (under 300 iterations) with a slight better accuracy of torque (Figure 3-24).

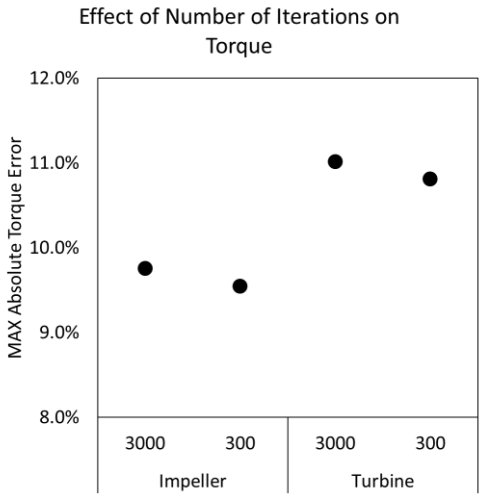

Figure 3-24. Effect of number of iterations on impeller and turbine torque for the medium size mesh.

Another look at the number of iterations with coarse mesh confirms the findings (Figure 3-25).

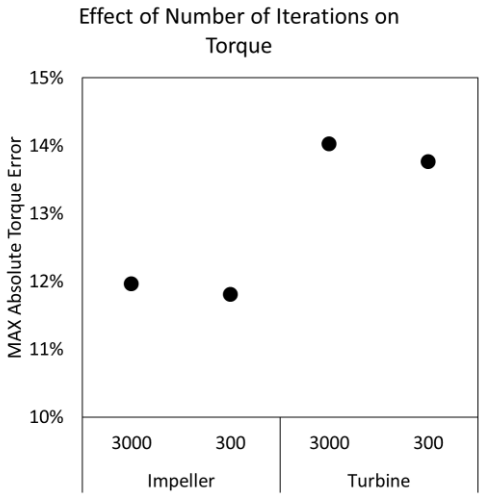

Figure 3-25. Effect of number of iterations on impeller and turbine torque for the coarse size mesh.

For the CFD results, when considering either the medium or coarse mesh sizes, 300 iterations resulted in results that are more accurate than with 3000 iterations. (Figure 3-26).

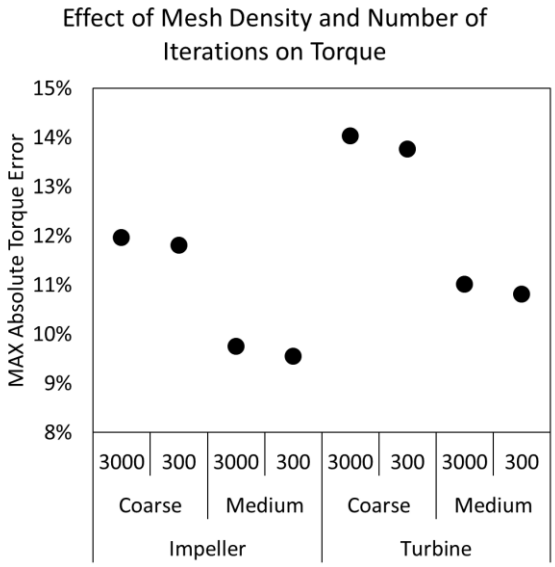

Figure 3-26. Combined view at the effects of mesh density and number of iterations.

Medium size mesh is more accurate than coarse and 300 iterations reduces time by almost 89% (Figure 3-27).

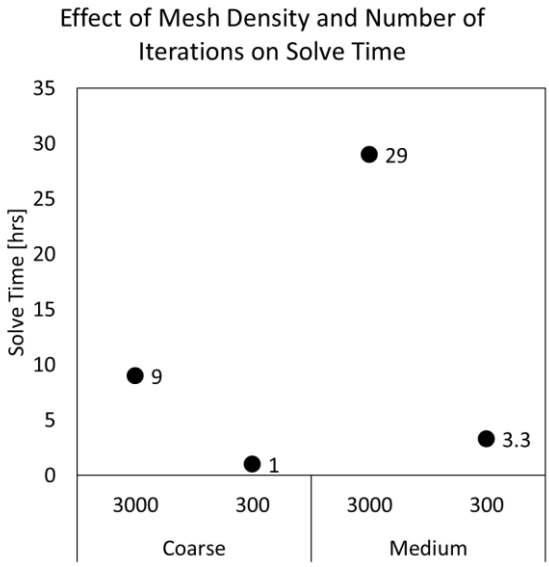

Figure 3-27. Effect of mesh density and iterations on solution time.

Needless to say, the significant reduction in computing time while maintaining or slightly improving accuracy are obvious and must be implemented as part of the optimal parameter selection. It is now obvious that past professional experiences with torque converter simulations completed performed by non-experienced, non-methodical analysts resulted in longer and unnecessary computational time and dollar value associated with delayed and inaccurate results.

3.10 CFD Optimal Parameter Setup for Solution Time

After comparing all 24 analyses, an optimal variable combination was found. On all experiments, medium size mesh proved more accurate than coarse mesh. Accuracy of the results when running 3000 iterations was no different from running 300. Second order pressure scheme was more accurate than PRESTO! for the coarse mesh but not for the medium mesh. After considering all experiments completed, two variable combinations

raised to the top as the ones yielding the most accurate torques and fast solution times for this stage of the investigation (Table 3-16).

Table 3-16. Optimal variable combination found from studies.

Fine mesh	Optimized for accuracy & time
3000 iterations	300 iterations
With blade ribs	With blade ribs
Tetrahedral	Tetrahedral
PRESTO! scheme for pressure	PRESTO! scheme for pressure
Fine size mesh	Medium size mesh
32,978,477 elements	3,338,636 elements
Spalart-Allmaras turbulence model	Spalart-Allmaras turbulence model
Coupled solver setup	Coupled solver setup
33 hours to solve 11 SR's	3.3 hours to solve 11 SR's

The optimal combination maintains good accuracy and a reasonably fast convergence. Fine mesh with ribs was more accurate but solution times (more than 99 hours for 11 speed ratios) may not make it feasible for industry timeframes. Comparing the fine and medium mesh with optimal parameters, the range of difference in the results can be appreciated (Figure 3-28).

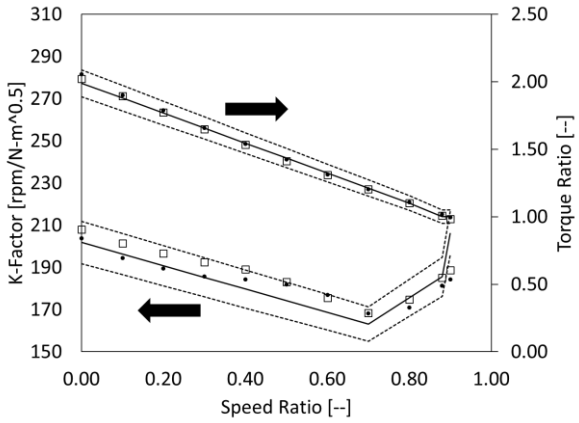

Figure 3-28. Optimal variable combination CFD results (squares) and fine mesh CFD results (dots) compared to test (solid) with +/-5% tolerance bands (dashed).

The tabulated look at the results show the CFD discrepancy from test (Table 3-17).

Table 3-17. Optimal and fine mesh tabulated torque discrepancies from test.

Fine mesh Max Error		Optimal combination Max Error	
Impeller	Turbine	Impeller	Turbine
9%	10%	10%	11%
RMSE 9%	RMSE 9%	RMSE 8%	RMSE 9%

Optimal CFD variable combination showed higher errors for impeller and turbine torque but the solution time makes it more desirable at this part of the experiments. When comparing either the maximum error or the RMSE shows the minimal advantage of the fine mesh over the optimal setting done so far. The significant reduction in solution times (30 times faster) while maintaining the accuracy in the predictions demonstrate the value and implications of a thorough study of all parameters and their combined effects (Figure 3-29 and Figure 3-30).

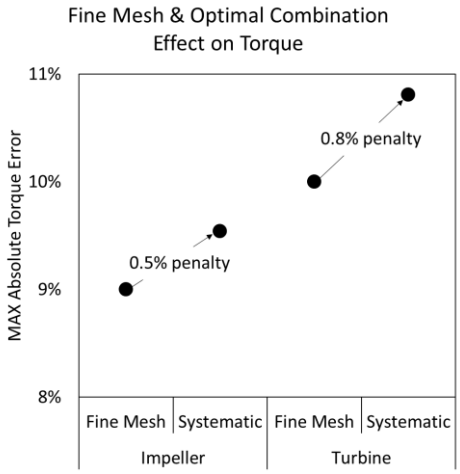

Figure 3-29. Effect of optimal combination of variables in impeller and turbine torque accuracy.

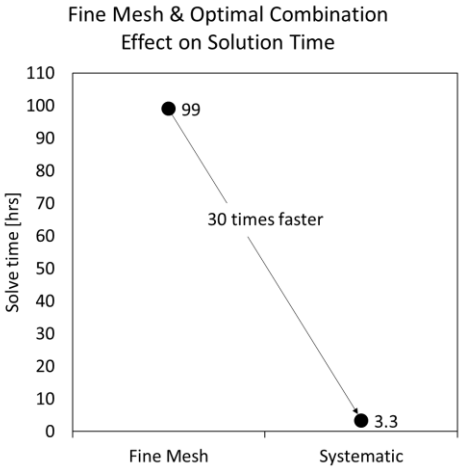

Figure 3-30. Effect of optimal variable combination in solution time.

3.11 CFD Optimal Parameter Setup for Accuracy

Although never tested due to computer limitations, an optimal variable combination can be obtained from the known performances of the different tests completed (Table 3-18).

Table 3-18. Optimal variable combination for accuracy.

With blade ribs
32,978,477 elements (Fine mesh)
Tetrahedral
3000 iterations
Spalart-Allmaras turbulence model
Coupled solver setup
PRESTO! pressure scheme
Estimate of 324 hours to solve full matrix

The reasoning behind the recommendations are simple. A model with blade ribs performed better than the one without ribs. Tetrahedral mesh was better than polyhedral. 3000 iterations provided a more stable convergence for the fine mesh. Spalart-Allmaras turbulence and PRESTO! pressure scheme were more accurate. Finally, a coupled solver accelerates convergence, although not ran, a coupled solver set up with the parameters above requires less iterations than standard solver. Time to solve on the other hand makes it less attractive. It will be shown next that further improvements could be made.

3.12 Further Improvements: 3rd Order MUSCL

To reduce discretization errors, a 3rd order Monotone Upstream-centered Scheme for Conservation Laws (MUSCL) was introduced to the final exercise matrix setup. The scheme was used to solve the equation of momentum and turbulence intensity. A higher order computational scheme should yield results that are more accurate. A third order MUSCL calculates the solution at the edges of each element. Each edge is shared by 2

elements. There will be a "Left-element" and a "Right-element" solution. When an element's edge is evaluated (element "i"), it's left-side edge solution $\left(u^{L}_{i-1/2}\right)$ combined with the right side solution of neighboring element "i-1" $\left(u^{R}_{(i-1)+1/2}\right)$ a possible average of the two solutions could be made which reduces the error in the calculation (Figure 3-31).

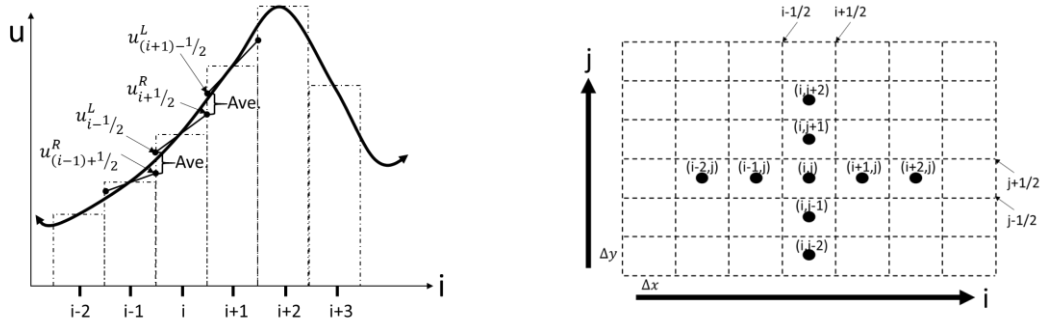

(a) (b)

Figure 3-31. MUSCL scheme numerical approximation of "u" example (a) and cell-centered 2-D grid (b).

The third order MUSCL scheme resembles a very familiar Reimann summation only the MUSCL method is not for approximating the area under the curve but an approximation of the curve itself. For the 3rd Order MUSCL demonstration, the following parameters were set (Table 3-19).

Table 3-19. 3rd Order MUSCL demonstrations variable combination.

300 iterations
With blade ribs
Tetrahedral
PRESTO! scheme for pressure
Medium size mesh
3,338,636 elements
Spalart-Allmaras turbulence model
Coupled solver setup
4.6 hours to solve 11 SR's
MUSCL

The MUSCL computational scheme improved maximum absolute errors over the fine mesh (the one deemed most accurate) at least 0.2% to 0.5% (Figure 3-32).

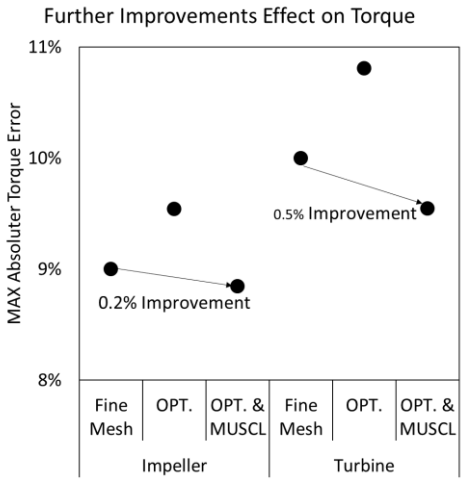

Figure 3-32. Effect of introducing higher order computational scheme in maximum absolute error.

As can be seen, the introduction of the 3rd order MUSCL computational scheme outperformed the variable setups of the previous exercise and closely matched (although

slightly better) the errors of the most accurate combination of variables obtained prior to studying the 3rd order MUSCL computational scheme (Table 3-20).

Table 3-20. Accuracy of the 3rd Order MUSCL scheme compared against Optimal (OPT) and Fine Mesh.

Fine mesh Max Error		OPT Combo Max Error		3rd Order MUSCL Max Error	
Impeller	Turbine	Impeller	Turbine	Impeller	Turbine
9%	10%	10%	11%	9%	10%
RMSE 9%	RMSE 9%	RMSE 8%	RMSE 9%	RMSE 5%	RMSE 6%

Introducing the 3rd order MUSCL computational scheme, although more accurate, it represents a slight penalty in computational time. Such penalty is minimal but must be understood when compared against the variable setups from the exercise (Figure 3-33).

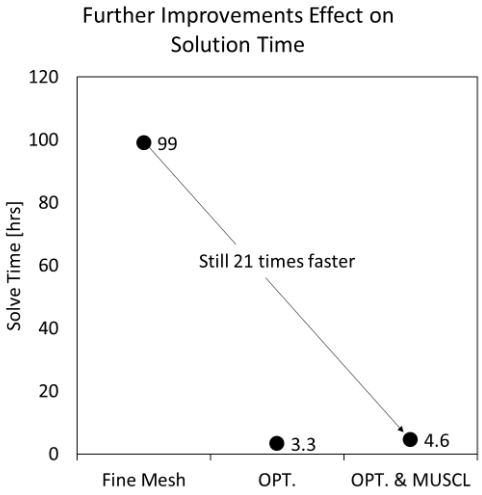

Figure 3-33. Solution time penalty for introducing the 3rd order MUSCL computational scheme.

Solution time for the 3rd order MUSCL computational scheme is still very competitive when compared to the fine mesh results. Although slightly higher solution time is required when compared to the most optimal combination obtained from the exercise, the accuracy outweighs such time penalty. Such computational time penalty could also be reduced further by reducing the number of iterations in the analysis to around 200 iterations for a solution time under 2 hours for all 11 speed ratios studied (Figure 3-34).

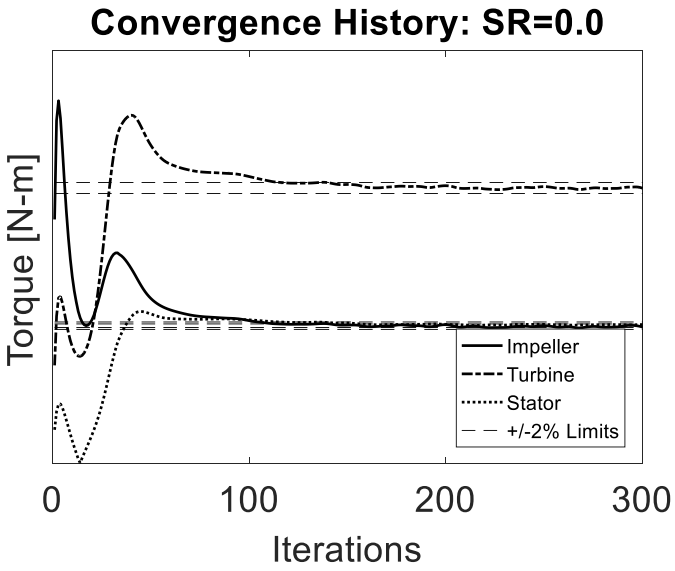

Figure 3-34. Convergence history for the 3rd order MUSCL computational scheme.

3.13 Further Improvements: Full TC Geometry

In addition to introducing the 3rd order MUSCL computational scheme, the torque converter in its entirety must be studied as part of the scope of the present work. All the cavities surrounding the torus were modeled. More information on surfaces, interfaces and individual cavity names can be seen in Appendix E. Sliding mesh was used at the interfaces between all fluid volumes. At the inlet and outlet boundaries of the torque converter fluid

domain, inlet and outlet pressures were applied. The pressures were obtained from values provided by the torque converter manufacturer. Meshing of the new fluid volume followed the same approach as the one already explained. Tetrahedral elements were used. The blades included ribs. The torus walls were meshed with 1.25 mm size elements while the elements in the bulk of the torus fluid volume measured 2.5 mm. The clutch disc wall was meshed with elements 0.625 mm in size to better capture the narrow gap between it and the TC cover. For all other cavities and walls, the element size was 3 mm (Figure 3-35).

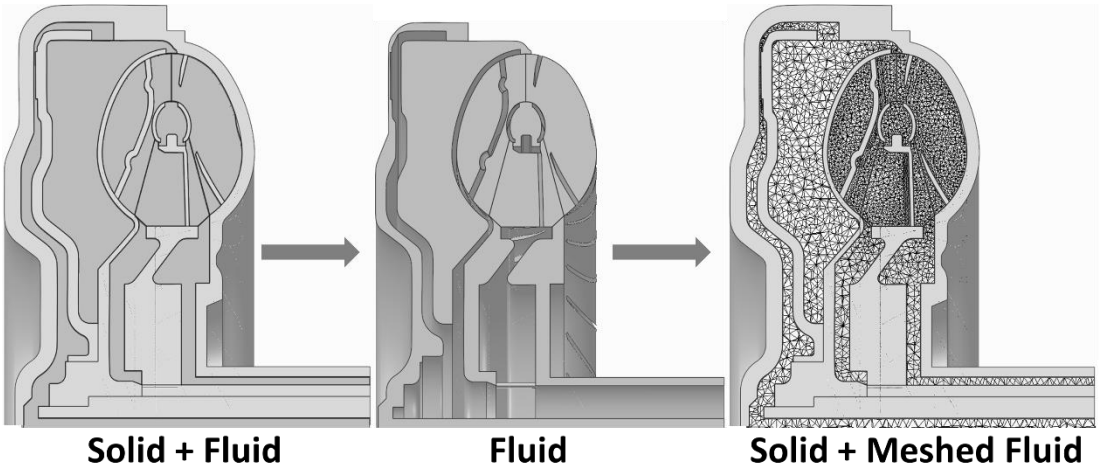

Figure 3-35. Fluid volumes for the entire torque converter model.

The total element count for the torque converter model is still considered a medium size model at 4,586,883 elements. Studying the entire torque converter improved accuracy on the simulated torques by 3% to 4% (Figure 3-36).

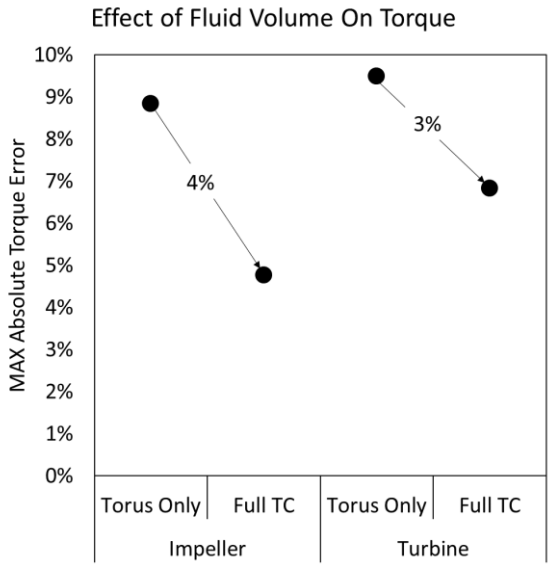

Figure 3-36. Accuracy in predicted torques for the full torque converter model.

The addition of the fluid volumes surrounding the torus resulted in an increase of 2 hours in computational time to solve all 11 speed ratios when compared to the torus only model. Such increase is expected since more elements are being added to the problem. Nonetheless, it still results in very desirable accuracy improvements and the time penalty can be justified and expected given the added complexity (Figure 3-37).

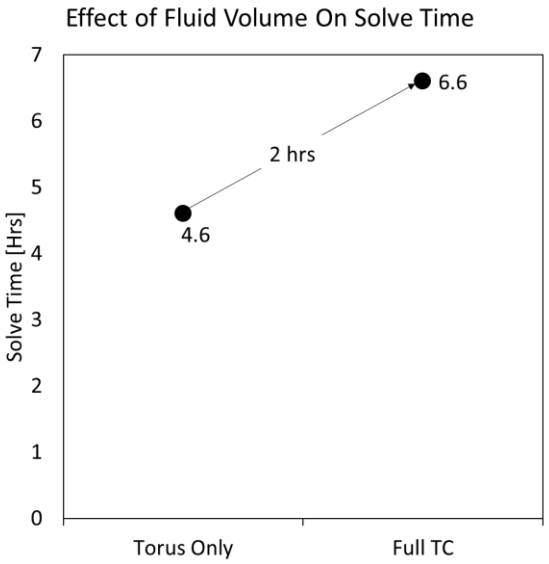

Figure 3-37. Time penalty incurred when modeling the full torque converter cavities.

3.14Further Improvements: ATF Temperature Study

Properties of the working fluid such as density and dynamic viscosity could affect considerably the accuracy of the results obtained. The results presented so far are for working fluid properties representing the properties for the average temperature between oil entering and leaving the torque converter. To gage the impact in accuracy by changing working fluid properties, the full torque converter and the torus only fluid volumes were run for all three possible temperatures (Table 3-21).

Table 3-21. Fluid properties of the ATF at various temperatures.

SR	Inlet		Average		Outlet	
	Dens.	Dyn. Visc	Dens.	Dyn. Visc	Dens.	Dyn. Visc
[--]	[kg/m^3]	[kg/m-s]	[kg/m^3]	[kg/m-s]	[kg/m^3]	[kg/m-s]
0	800	0.00794	799	0.00776	799	0.00759
0.1	800	0.00794	793	0.00644	785	0.00526
0.2	800	0.00794	790	0.00594	780	0.00460
0.3	800	0.00794	789	0.00578	778	0.00440
0.4	800	0.00794	789	0.00578	778	0.00440
0.5	800	0.00794	790	0.00587	779	0.00453
0.6	800	0.00787	791	0.00608	782	0.00484
0.7	800	0.00780	793	0.00651	787	0.00545
0.8	800	0.00780	796	0.00716	793	0.00651
0.88	800	0.00780	797	0.00737	795	0.00694
0.9	800	0.00780	798	0.00744	796	0.00708

In the present study, lower errors were found for ATF representing inlet temperature (Figure 3-38).

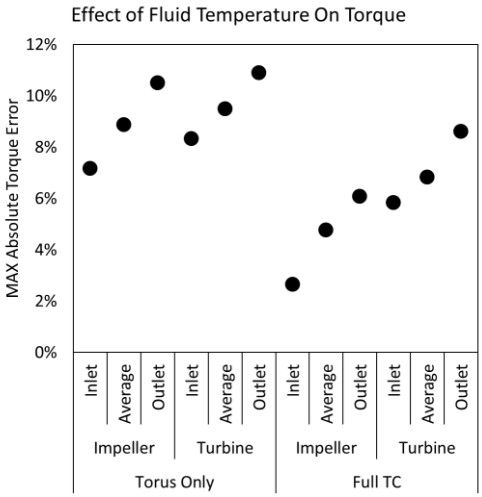

Figure 3-38. Accuracy of the results when studying working fluid temperature effects.

Overall, inlet temperature properties of the working fluid yielded results that are more accurate. Once more, the full torque converter yielded better results than the ones obtained by modeling the torus only.

To summarize the exercise, it has been demonstrated that actively eliminating parameters of a design of experiments is a fast and still valid method. In the torque converter under study, the introduction of higher order computational schemes such as 3rd order MUSCL yielded better results that the ones without it. Modeling the entire torque converter further improved accuracy of the simulations. Finally, the temperature and associated working fluid properties could affect positively or not the accuracy of the simulations. For new designs where test data is not available, it is best not to consider temperature effects and model the problem with average temperatures unless plenty of historical background and experience dictates otherwise.

3.15DOE for Torus Surrounding Cavities

Once the final recommendation of variable resulting from the exercise was completed, an L8, 2 levels-3 factors Taguchi Design of Experiments (DOE) matrix was developed to study sensitivity of selected parameters on the surrounding cavities. Among the parameters studied, a Quadratic Upstream Interpolation for Convective Kinematics (QUICK) was introduced to solve the equation of momentum and turbulence intensity. The QUICK computational scheme is a higher order scheme and reduces numerical errors. All other parameters have been explained earlier. New medium and fine element size mesh were introduced (Table 3-22).

Table 3-22. Additional parameters for DOE sensitivity on the surrounding cavities.

Mesh	2 mm walls & bulk (Medium)
	1.5 mm walls & bulk (Fine)
Turbulence Model	k-ε
	k-ω
Momentum & turbulence intensity computational scheme	MUSCL
	QUICK

The goal for the DOE is to determine impact of the chosen variables on accuracy and solution time. The new DOE matrix produced 8 new experiments. The new experiments were targeted at only three speed ratios (SR=0.3, 0.5 and 0.7). An explanation of the nomenclature for easy follow is tabulated (Table 3-23).

Table 3-23. Experiments nomenclature.

Nomenclature	Meaning
Optimal	Recommended optimal combination as a result of the present work (sub-chapter 3.13).
MedKERQ	New medium mesh, k-ε, QUICK
FinKERQ	New fine mesh, k-ε, QUICK
MedKERM	New medium mesh, k-ε, MUSCL
FinKERM	New fine mesh, k-ε, MUSCL
MedKWSSTQ	New medium mesh, k-ω, QUICK
FinKWSSTQ	New fine mesh, k-ω, QUICK
MedKWSSTM	New medium mesh, k-ω, MUSCL
FinKWSSTM	New fine mesh, k-ω, MUSCL

After running all the new experiments, it was found that solution time worsened (Figure 3-39).

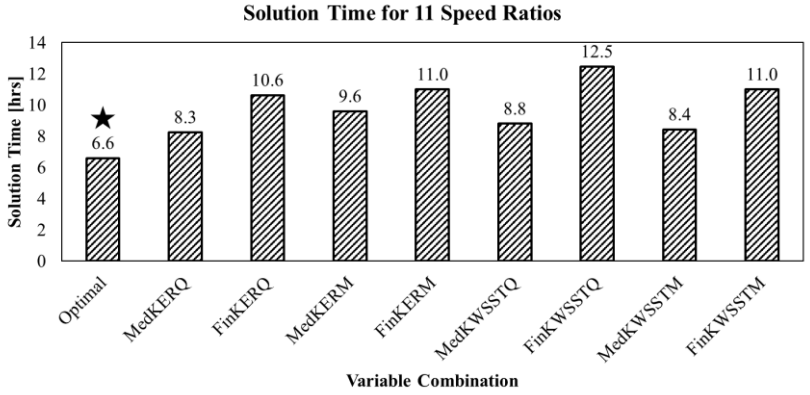

Figure 3-39. Solution time comparison for the surrounding cavity DOE.

The optimal combination of variable presented in sub-chapter 3.13 is still the fastest. A total of 11 speed ratios are solved in 6.6 hours. When comparing accuracy of the new DOE, MedKERM for the lowest speed ratio (SR=0.3) showed improvements. Maximum impeller errors were improved by 2%, turbine maximum errors and root mean square errors by 1% (Figure 3-40).

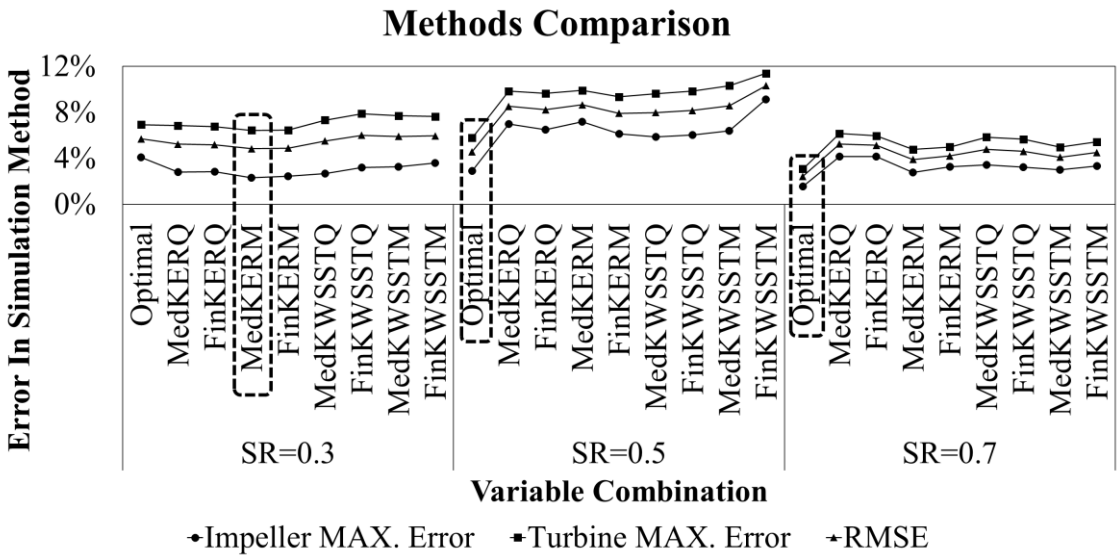

Figure 3-40. Calculation error comparison for the surrounding cavity DOE.

The optimal settings from sub-chapter 3.13 are still the most accurate for the middle and highest speed ratios. The difference in error seen with the optimal method compared to MedKERM for the low speed ratio are insignificant when compared to the error magnitudes obtained with the optimal combination for the last two not to mention the additional 3 hours of computational time needed. This new DOE for the cavities surrounding the torus did not yield reason to deviate from the recommended settings.

If an ANalysis Of Variance (ANOVA) is done, the effect of a set number of variables on the accuracy can be established. ANOVA is a sensitivity study to find out the variables that influence the most in the calculation.

At SR=0.3, the variable that most impact had on impeller and turbine maximum errors and RMSE was the turbulence model. The impeller was slightly affected by the mesh density. Computational schemes MUSCL or QUICK had no effect on the impeller. For the turbine, both mesh density and computational schemes had minor effects. The RMSE showed similar behavior (Figure 3-41).

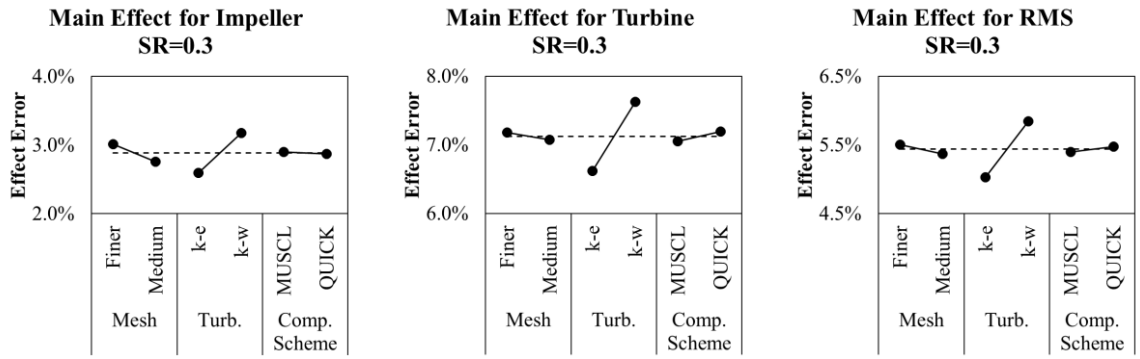

(a) (b) (c)

Figure 3-41. Main effect of new DOE on maximum torque error for the impeller (a), turbine (b) as well as RMSE (c) at SR=0.30.

For SR=0.5, effects of computational scheme across all three errors presented was noticeable (Figure 3-42).

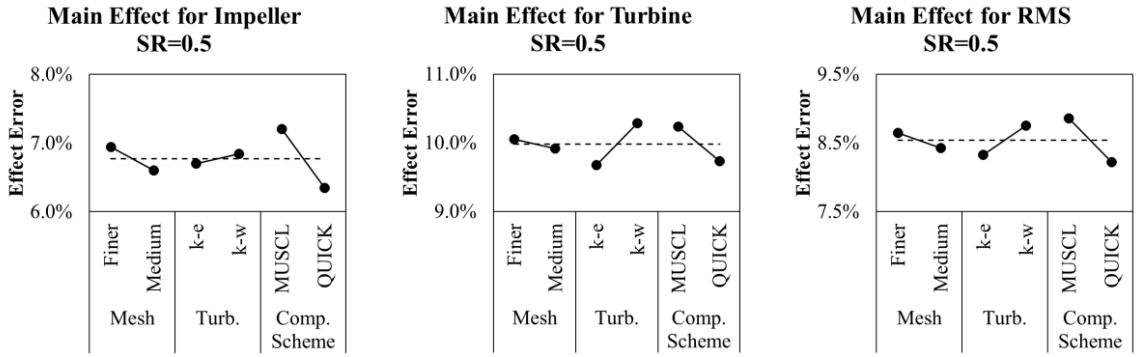

(a) (b) (c)

Figure 3-42. Main effect of new DOE on maximum torque error for the impeller (a), turbine (b) as well as RMSE (c) at SR=0.50.

At SR=0.5, all variables influenced the errors. The mesh density was the least influential of all three groups.

Finally, at SR=0.7, computational schemes had more effect in the results than all the other two variable groups with mesh density being the least influential one. Turbulence intensity had only minor effect in the impeller maximum errors (Figure 3-43).

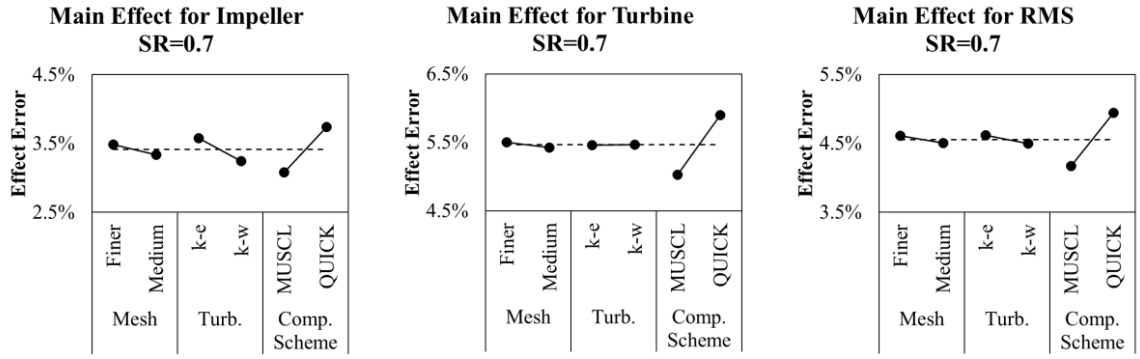

(a) (b) (c)

Figure 3-43. Main effect of new DOE on maximum torque error for the impeller (a), turbine (b) as well as RMSE (c) at SR=0.70.

The DOE exercise to study cavities surrounding the torus demonstrate the validity of the systematic approach presented throughout this chapter. Accuracies did not improve and solution times were worsened with the DOE. The sensitivity pointed out mixed reaction not only by speed ratios but also by individual elements. For the SR=0.3 & SR=0.5, optimal settings will be obtained with the use of the new medium sized mesh, the k-ε turbulence model and the QUICK computational scheme. When such combination for the SR=0.3 & 0.5 is compared to the combination at SR=0.7, conflicting selections are seen for the turbulence and computational scheme variable groups.

With all analyses completed as part of this investigation, several error ranges can be seen per speed ratio. Let us say procedure "A" produced lowest error for "X" speed ratio while procedure "B" produced better results for speed ratio "Y" but degraded accuracy for speed ratio "X". A procedure could be put together to reduce all errors at every speed ratio by picking and choosing among all analyses completed (Table 3-24).

Table 3-24. Procedures investigated as part of this investigation.

Proc.	Mesh	Ribs	Pressure Scheme	Solver	Mesh	Turbulence	Iterations
A	Polyhedral	No	2nd order	Standard	Fine	k-ε	3000
B	Tetrahedral	No	2nd order	Standard	Fine	k-ε	3000
C	Tetrahedral	No	2nd order	Standard	Medium	k-ε	3000
D	Tetrahedral	No	2nd order	Standard	Coarse	k-ε	3000
E	Tetrahedral	No	2nd order	Standard	Coarse	k-ω	3000
F	Tetrahedral	No	2nd order	Standard	Coarse	S-A	3000
G	Tetrahedral	No	2nd order	Coupled	Coarse	k-ε	3000
H	Tetrahedral	No	2nd order	Coupled	Coarse	k-ω	3000
I	Tetrahedral	No	2nd order	Coupled	Coarse	S-A	3000
J	Tetrahedral	No	2nd order	Coupled	Medium	S-A	3000
K	Tetrahedral	No	PRESTO	Coupled	Coarse	S-A	300
L	Tetrahedral	No	PRESTO	Coupled	Coarse	S-A	3000
M	Tetrahedral	No	PRESTO	Coupled	Medium	k-ω	300
N	Tetrahedral	No	PRESTO	Coupled	Medium	k-ω	3000
O	Tetrahedral	No	PRESTO	Coupled	Medium	S-A	300
P	Tetrahedral	No	PRESTO	Coupled	Medium	S-A	3000
Q	Tetrahedral	Yes	2nd order	Standard	Fine	k-ε	3000
R	Tetrahedral	Yes	2nd order	Coupled	Coarse	S-A	3000
S	Tetrahedral	Yes	2nd order	Coupled	Medium	S-A	3000
T	Tetrahedral	Yes	PRESTO	Coupled	Coarse	S-A	300
U	Tetrahedral	Yes	PRESTO	Coupled	Coarse	S-A	3000
V	Tetrahedral	Yes	PRESTO	Coupled	Medium	S-A	3000
W	Tetrahedral	Yes	PRESTO	Coupled	Medium	S-A	300
X	Tetrahedral	Yes	2nd order	Coupled	Medium	S-A	300

The variable setup for obtaining lowest overall errors was obtained by targeting lower errors for the turbine (Table 3-25).

Table 3-25. Optimal parameter selection for reduced errors.

SR	Procedure	Solution Time
0.00	B	9
0.10	B	9
0.20	B	9
0.30	Q	9
0.40	Q	9
0.50	Q	9
0.60	W	0.3
0.70	Q	9
0.80	D	0.25
0.88	M	0.3
0.90	H	1
Total Solution Time		**64.85 hours**

If a variable combination was to be set by targeting lowest errors obtained for each speed ratio using all analyses presented so far, it will take 65 hours of computing time and multiple computer models will have to be built. This is only possible after completing the systematic CFD setup exercise for the geometry under study. Errors could reduce by as much as 6%. It has been learned so far that CFD accuracy is not repeatable. Error magnitudes change due to geometry, torque converter size and blade design and even due to numerical errors introduced by CFD and even by test conditions as will be shown in Chapter 4. Such approach will not be appealing to any analyst and it will not be cost effective for any industry. As a result, it is recommended that the variable combination presented in sub-chapter 3.13 be the one to use for test correlation. To solidify the decision

a comparison can be done with the CFD procedures presented earlier in the literature review (Figure 3-44).

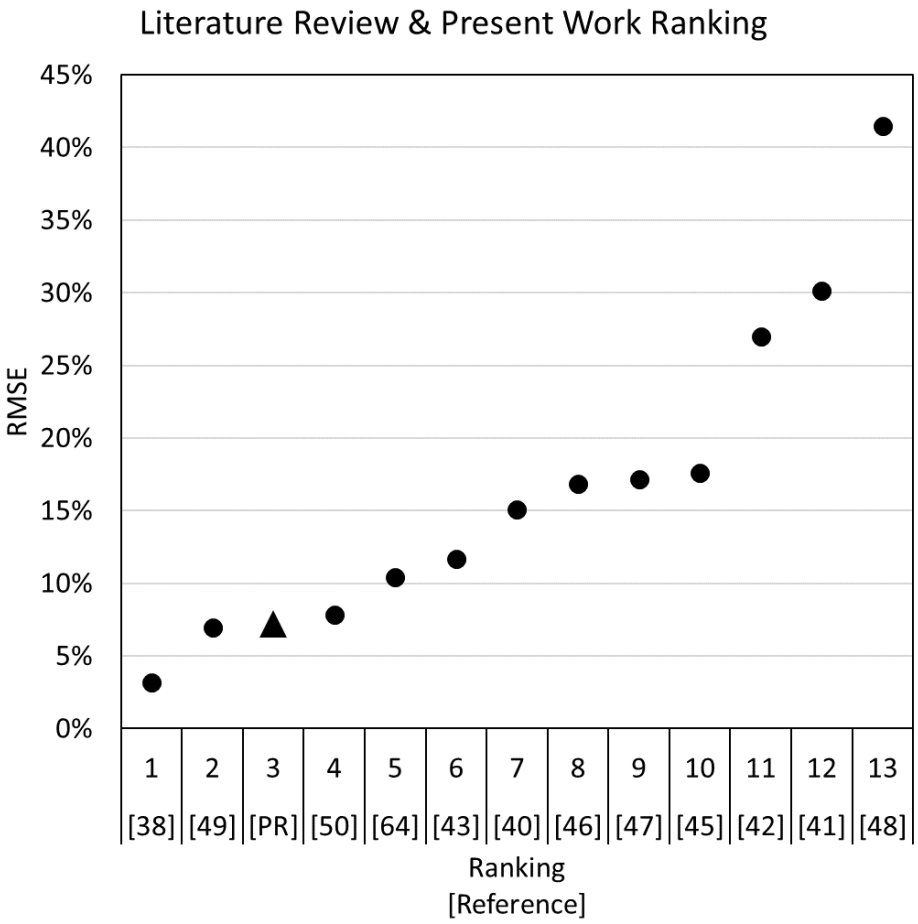

Figure 3-44. Literature CFD torque accuracies (circles) compared to present work (triangle).

Although the procedure developed for the present work was not the best, it is very competitive. A comparison in solution time between the present work and the one in literature is not possible due to unreported values. Statistical parameters between all

reported CFD results in literature also show the competitiveness of the present work (Table 3-26).

Table 3-26. Statistical parameters for literature CFD procedures compared to present work.

Source >>	**Literature**		**Present Work**	
Parameter	**Impeller**	**Turbine**	**Impeller**	**Turbine**
Minimum	0.0%	0.4%	1%	3%
Maximum	48%	49%	25%	31%
STD Dev.	14%	13%	4%	5%
Variance	2%	2%	0%	0%
Mean	14%	13%	5%	6%
Median	9%	8%	4%	5%
Mode	4%	4%	2%	4%

4 CFD vs Test Results

With the full torque converter model established, correlation between experimental and simulated torque and pressure results can be assessed.

4.1 TC CFD Monitor Points Layout

As shown in Chapter 2, 29 pressure transducers were installed inside the torque converter under study. More information about all monitor points coordinates can be found in Appendix D.

Additional monitor points on the toroidal components were added to have continuous pressure patterns on the impeller, turbine and stator (Figure 4-1, through Figure 4-5).

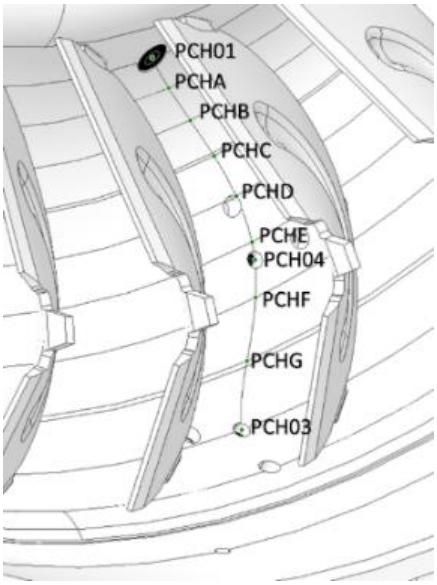

Figure 4-1. Additional monitor points added to the impeller channel.

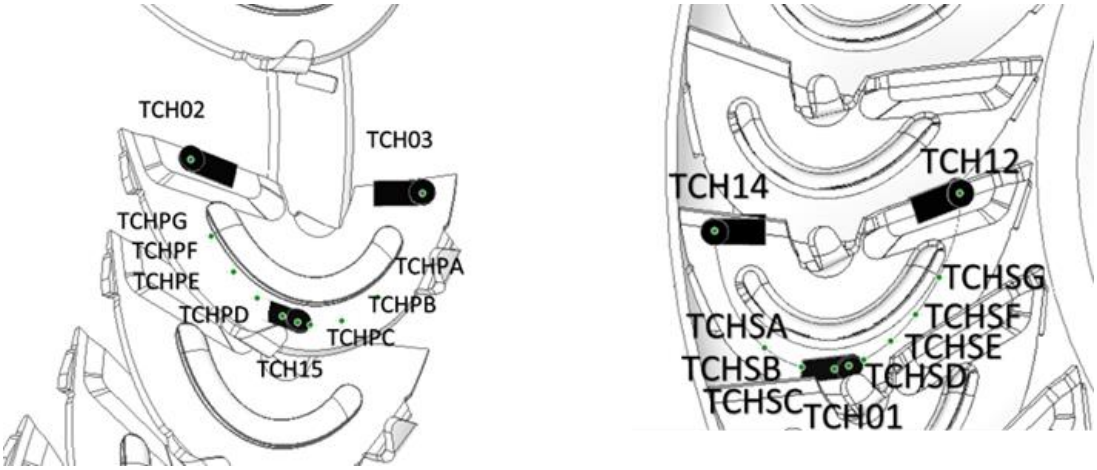

(a) (b)

Figure 4-2. Additional monitor points added to the turbine blade pressure side (a) and suction side (b).

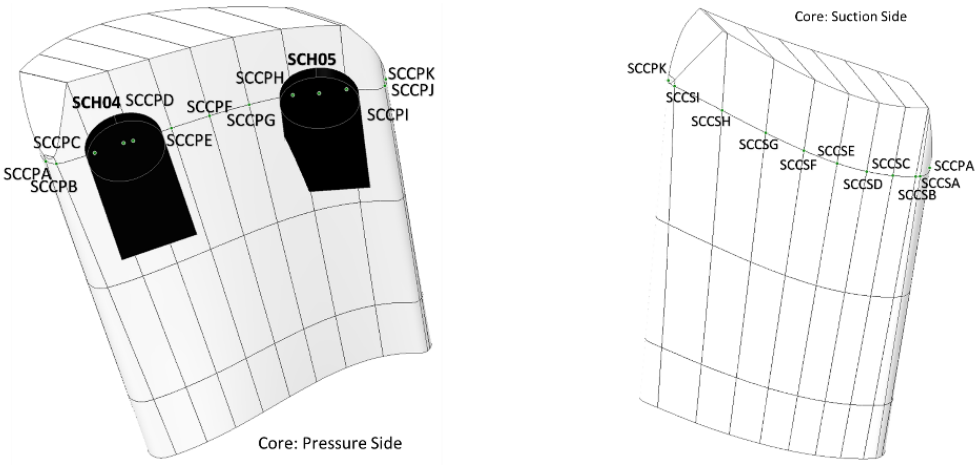

(a) (b)

Figure 4-3. Stator blade monitor points on core streamline pressure side (a), core suction side.

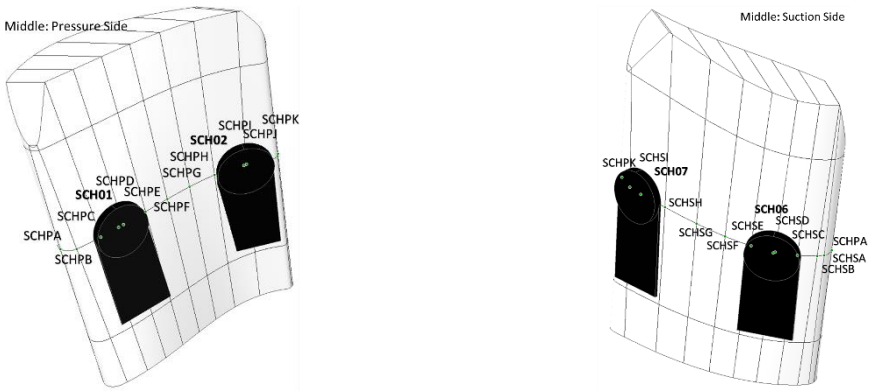

(a) (b)

Figure 4-4. Stator blade monitor points on middle streamline pressure side (a), middle suction side (b).

(a) (b)

Figure 4-5. Stator blade monitor points on shell streamline pressure side (a) and shell suction side (b).

4.2 TC CFD Test Matrix

Stalling of the torque converter was not possible during transmission tests. Only ten speed ratios were acquired, SR=0 was not tested. Nine different test were completed with the instrumented torque converter for 10 speed ratios from 0.1 to 0.90 (Table 4-1).

Table 4-1. Test matrix for the experiments and simulations.

Test Date/Filename	Gear	Target Impeller Torque [N-m]	Target Speed ratios
July 26 2018	5th	75	0.1,0.2,0.3,0.4,0.5,0.6,0.7,0.8,0.88,0.90
August82018	5th	75	0.1,0.2,0.3,0.4,0.5,0.6,0.7,0.8,0.88,0.90
August82018	6th	75	0.1,0.2,0.3,0.4,0.5,0.6,0.7,0.8,0.88,0.90
August82018	6th	75	0.1,0.2,0.3,0.4,0.5,0.6,0.7,0.8,0.88,0.90
Aug212018	5th	75	0.1,0.2,0.3,0.4,0.5,0.6,0.7,0.8,0.88,0.90
Aug212018	6th	75	0.1,0.2,0.3,0.4,0.5,0.6,0.7,0.8,0.88,0.90
Aug232018	5th	75	0.1,0.2,0.3,0.4,0.5,0.6,0.7,0.8,0.88,0.90
Aug232018	6th	50	0.1,0.2,0.3,0.4,0.5,0.6,0.7,0.8,0.88,0.90
Aug232018	6th	75	0.1,0.2,0.3,0.4,0.5,0.6,0.7,0.8,0.88,0.90

Due to limitations on the absorbing dynamometer, torque at the input dynamometer had to be maintained to never exceed 75 N-m on 5^{th} and 6^{th} gear only. The transmission gear ratio could easily make the output torque exceed the dynamometer torque limit. The maximum torque allowable on the dynamometer shafting is 950 N-m. All tests were performed so that no torque on the output dyno would ever exceed 475 N-m (a safety factor of 2).

Multiplexing of the channels required at least 60 seconds of data acquisition in order to capture at least one cycle through all channels of the turbine transmitter. The reason for the 60 seconds was due to the telemetry requirements to energize all transmitters looking for the telemetry marker before it could acquire data. Not only that, once it sees the marker, the telemetry has to go through one complete multiplexing of all channels within one transmitter before starting to acquire data once it sees the marker a second time (Figure 4-6).

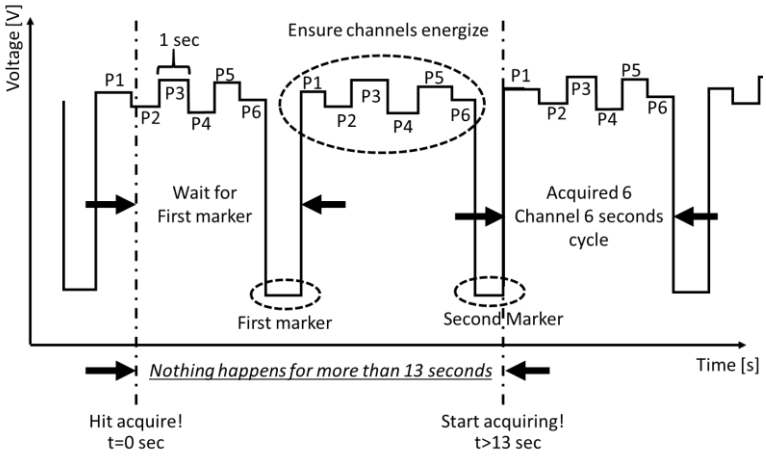

Figure 4-6. Mock view of telemetry system looking for marker.

As an example, typical acquired data is presented in Figure 4-7. It shows multiple 7 channels groupings/cycles for the impeller and stator while the turbine only completed two 15 channels cycles.

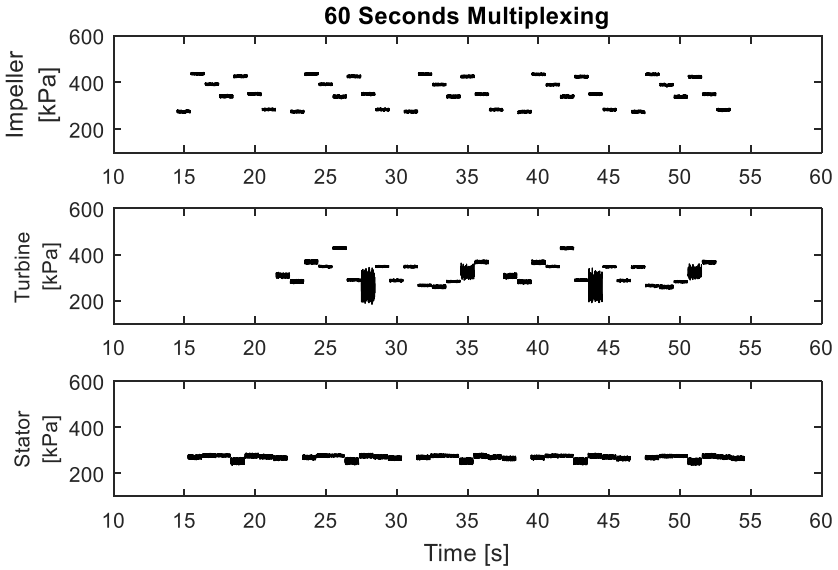

Figure 4-7. Sample 60 seconds of data for the 6th gear with 75 N-m input torque into the impeller when line pressure was set to low on SR=0.9.

The data-free portion of the 60 seconds from t=0 to approximately t=15 seconds on the impeller is due to the telemetry looking for the marker on the signal as explained earlier. In this example, it seems the first marker must have shown up at around t=8 seconds, the system waited for the second marker to show up before starting to acquire data around t=15 seconds. A similar behavior occurred on the stator signal and due to the amount of channels in the turbine transmitter, the turbine started data acquisition around t=22 seconds.

The data shown in Figure 4-7 has been post processed to remove dropouts for pictorial purposes to show typical signal acquired. Measured data will be shown in the next figures starting with the impeller first 7 channels of multiplexed data (Figure 4-8).

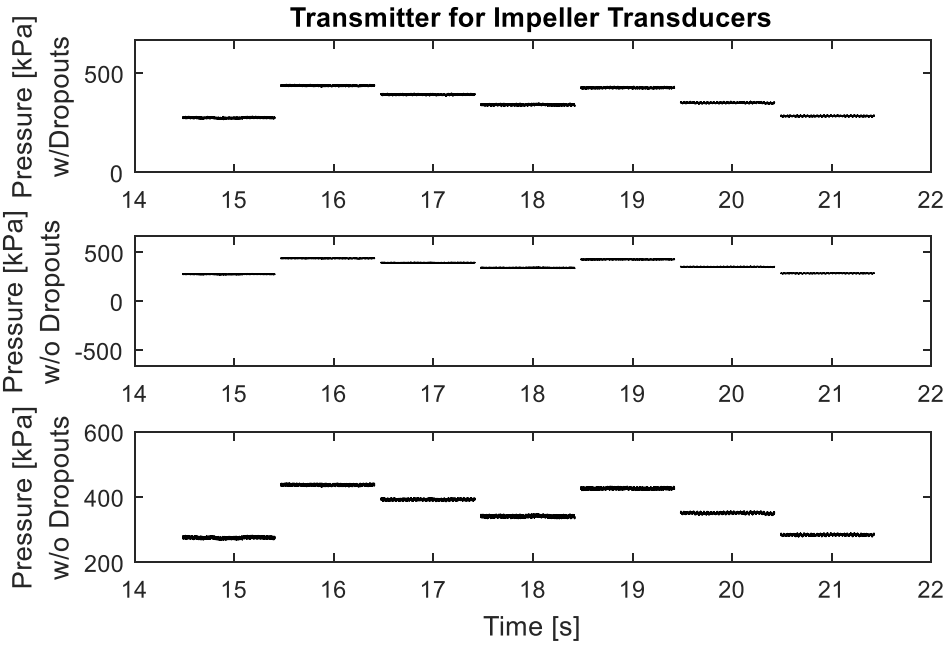

Figure 4-8. Multiplexed impeller channels for 6th gear, 75 N-m input torque SR=0.9 with low line pressure settings.

The first impeller multiplex cycle started with transducer PCH01 at approximately 14.3 seconds ending with PCH07 at approximately 21.5 seconds. The impeller signals for the most part remained dropout free throughout all the experiments. The same cannot be said about the turbine signal (Figure 4-9).

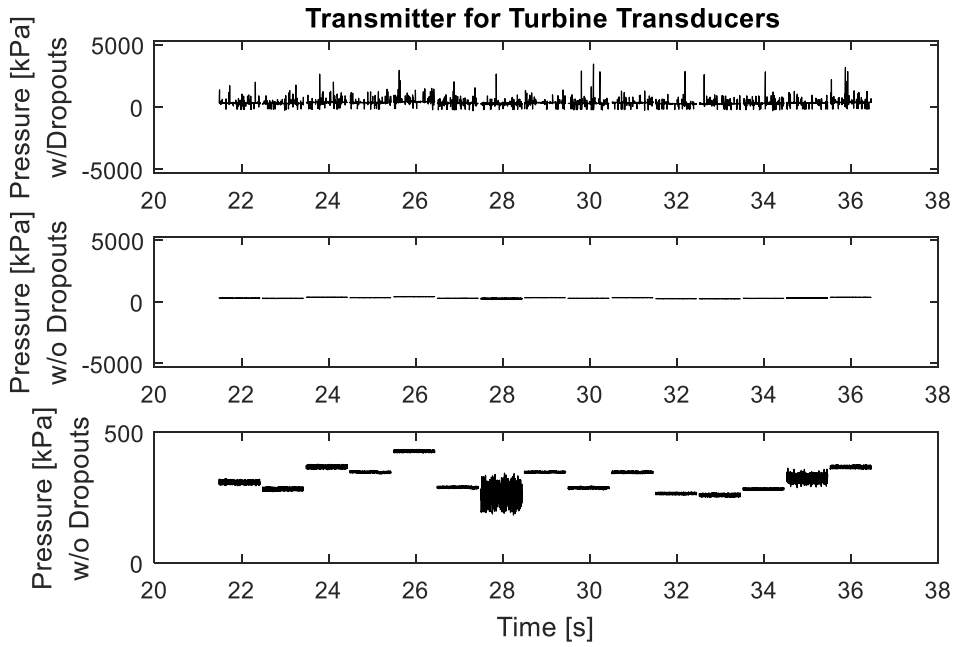

Figure 4-9. Multiplexed turbine channels for 6th gear, 75 N-m input torque SR=0.9 with low line pressure settings.

The turbine signal is the most affected by the dropouts. The reason behind the poor quality of the turbine data is due to the location of its transmitter. It had to travel through several walls before being picked up by the receiver. Turbine channel TCH01 started approximately at the 21 seconds mark ending with TCH15 slightly under 37 seconds.

Finally, a sample telemetry multiplexed data for one stator cycle can be seen in Figure 4-10. The quality of the signal is not as bad as the signals obtained with the turbine. In

order to help reduce the amount of dropouts on the stator signal, the impeller had to be spinning faster than 600 rpm due to the nature of the instrumentation.

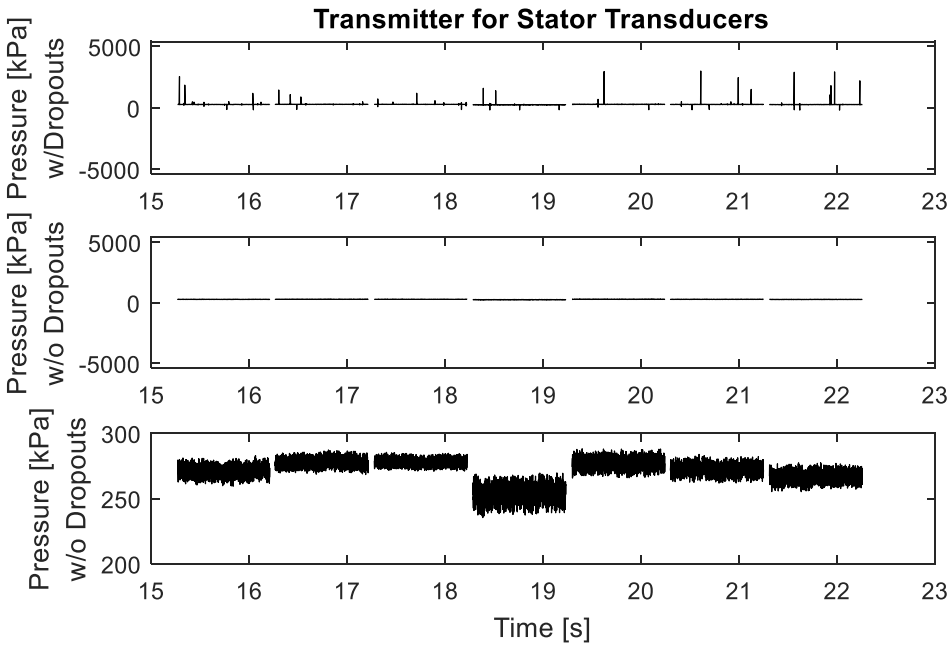

Figure 4-10. Multiplexed stator channels for 6th gear, 75 N-m input torque SR=0.9 with low line pressure settings.

The dropouts contents on the signals remained consistent throughout all the experiments. A Hampel function averaging 1000 points before and after the dropout cleaned the signal. Each transducer on the pictures is represented by one data trace. The stator started right after the impeller at just over the 15 seconds mark for SCH01 and ended its first multiplex cycle approximately at the 21.5 seconds mark. The procedure repeated until the 60 seconds window was completed.

The average of each transducer trace was calculated and used for comparing it to the CFD simulated pressures.

With the data acquired, data for the CFD model was then processed. Impeller and turbine speeds were gathered directly from test data. The input dynamometer speed is the same as the impeller speed. The output dynamometer speed, combined with the transmission gear ratios were used to calculate the turbine speed. Oil density, dynamic viscosity, torque converter inlet pressure (TCH11) and cooler flow were linearized prior to using them in the CFD model (Figure 4-11).

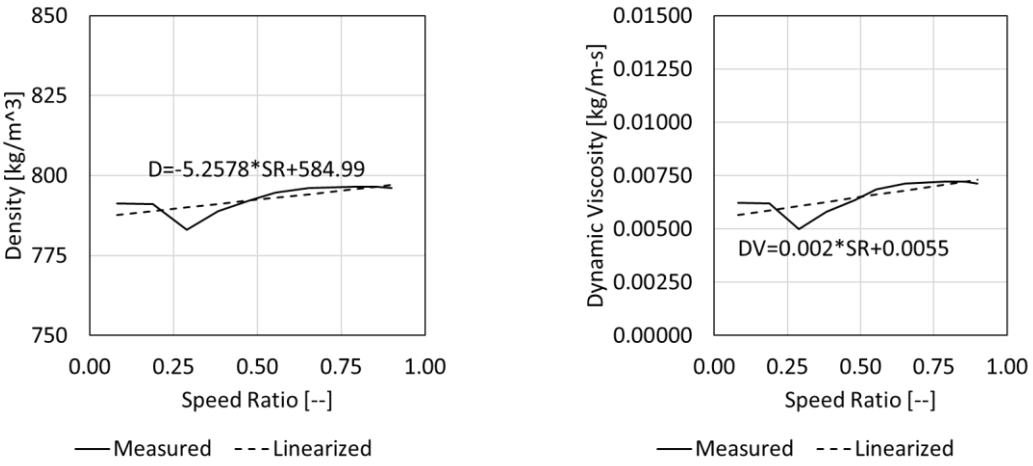

(a) (b)

Figure 4-11. Linearization example for fluid density (a) and viscosity (b).

For the torque converter outlet flow and inlet pressures (Figure 4-12).

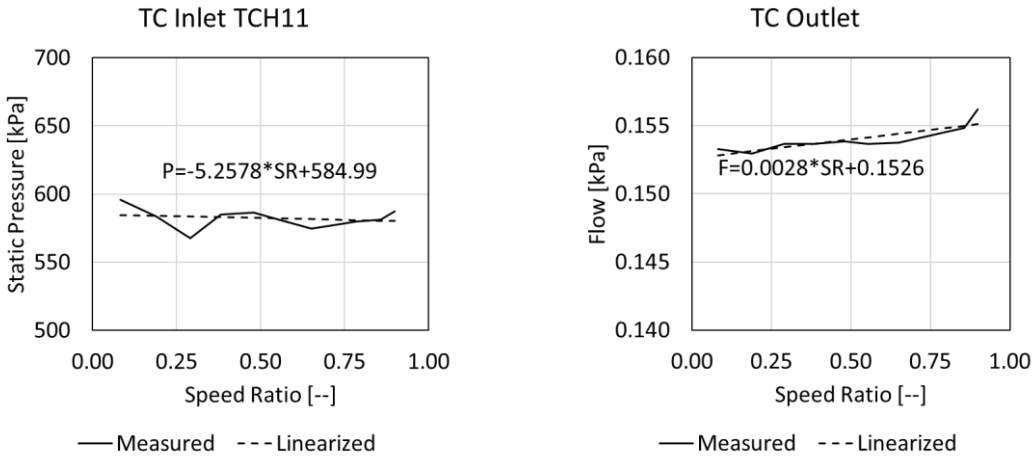

(a) (b)

Figure 4-12. Linearization example for torque converter inlet pressure (a) and outlet flow (b).

The reasoning behind linearization was to eliminate inconsistencies added by the test procedure. The low speed ratios generated more heat than the lower ones, a cooling cycle had to be added in between the tested speed ratios. Once cooling of the oil was completed, a new speed ratio condition was set and tested. Although similar consistent conditions were targeted, differences in temperatures between test points caused different oil density and viscosity resulting in different pressures.

To predict pressures more accurately inside the torque converter, turbine pressure transducer number 11 (TCH11) was used as torque converter inlet pressure due to its proximity to real inlet. TCC Release, although measured and acquired, was considered too far from the inlet when compared to the location of transducer TCH11 as will be seen in the test matrix sub-chapter to follow. For a non-instrumented converter TCC release could be used.

Impeller and turbine speeds gathered from the tests were used on the CFD simulations to match their respective speeds. Torque was monitored in order to establish convergence similar to what was done on Chapter 3. To reach convergence, the full torque converter model was run for 300 iterations. Solution times for the full torque converter increased by 2 hours when compared to the torus only model for a total 4.6 hours to solve all 11 speed ratios presented in Chapter 3

4.3 Torus Only vs. Full Torque Converter Models

To present a complete method for design, both the torus only and the full torque converter CFD models explained in Chapter 3 will be evaluated and compared for all tests previously presented in Table 4-1. The following torque comparisons are for the torus only model and full torque converter geometries cases. For all the studies presented in this chapter, only three speed ratios are presented (Figure 4-13 to Figure 4-21).

July 26 2018 tests

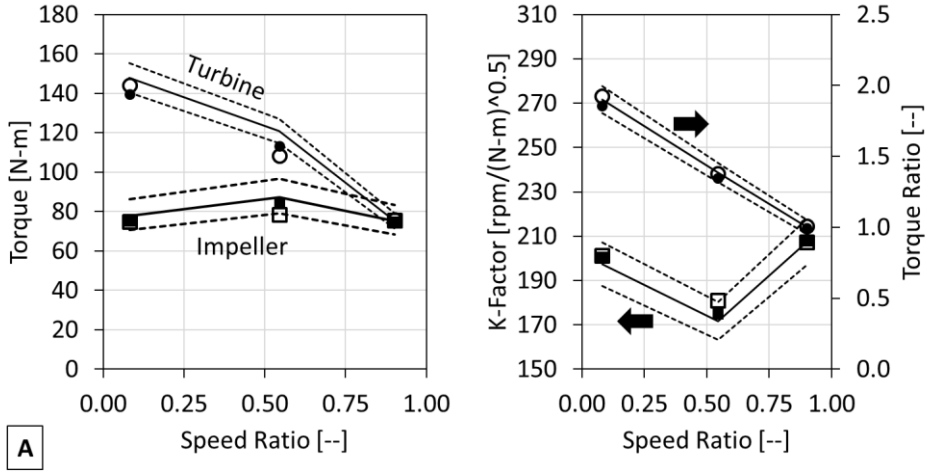

Figure 4-13. Simulated torques vs test for 5th gear with 75 N-m target impeller torque and non-dimensional values for full TC simulation (filled markers), torus only (white markers), test (solid line) and factory tolerance (dashed lines).

August 8 2018 tests

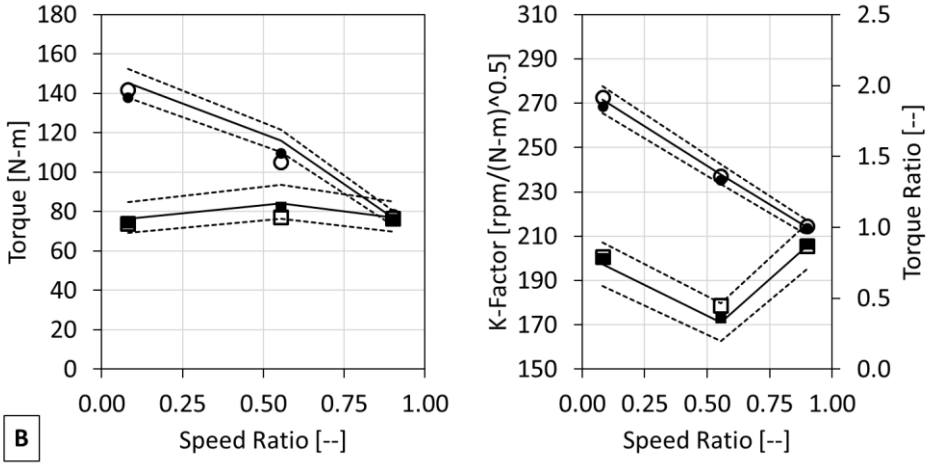

Figure 4-14. Simulated torques vs test for 5th gear with 75 N-m target impeller torque and non-dimensional values for full TC simulation (filled markers), torus only (white markers), test (solid line) and factory tolerance (dashed lines).

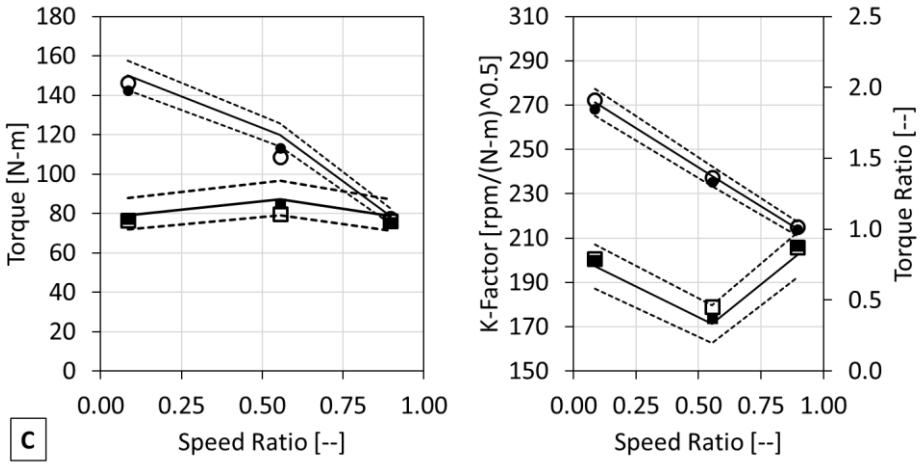

Figure 4-15. Simulated torques vs test for first run on 6th gear with 75 N-m target impeller torque and non-dimensional values for full TC simulation (filled markers), torus only (white markers), test (solid line) and factory tolerance (dashed lines).

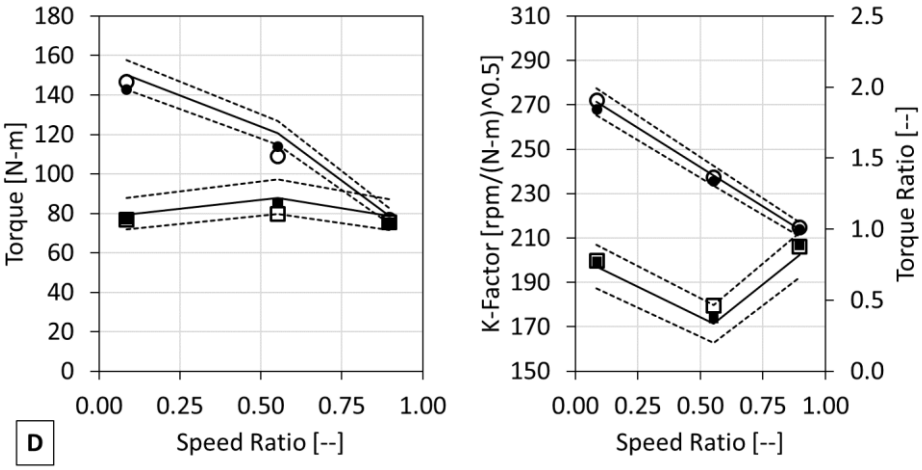

Figure 4-16. Simulated torques vs test for second run on 6th gear with 75 N-m target impeller torque and non-dimensional values for full TC simulation (filled markers), torus only (white markers), test (solid line) and factory tolerance (dashed lines).

August 21 2018 tests

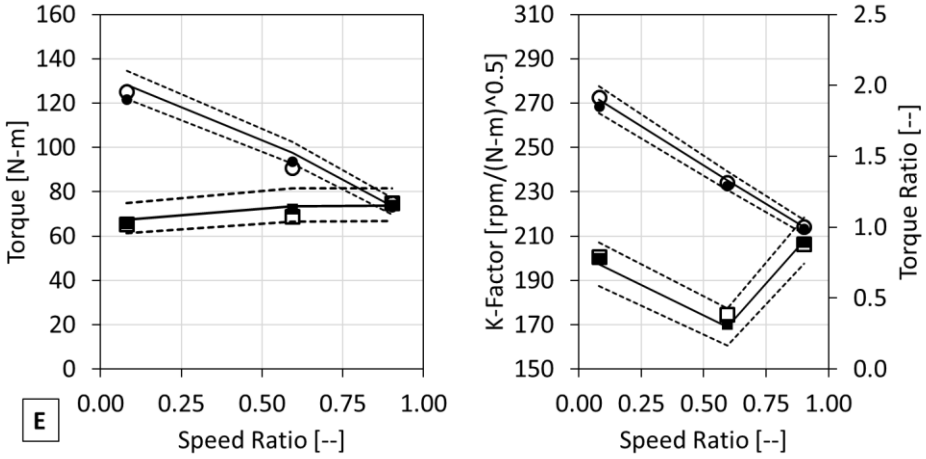

Figure 4-17. Simulated torques vs test for 5th gear with 75 N-m target impeller torque and non-dimensional values for full TC simulation (filled markers), torus only (white markers), test (solid line) and factory tolerance (dashed lines).

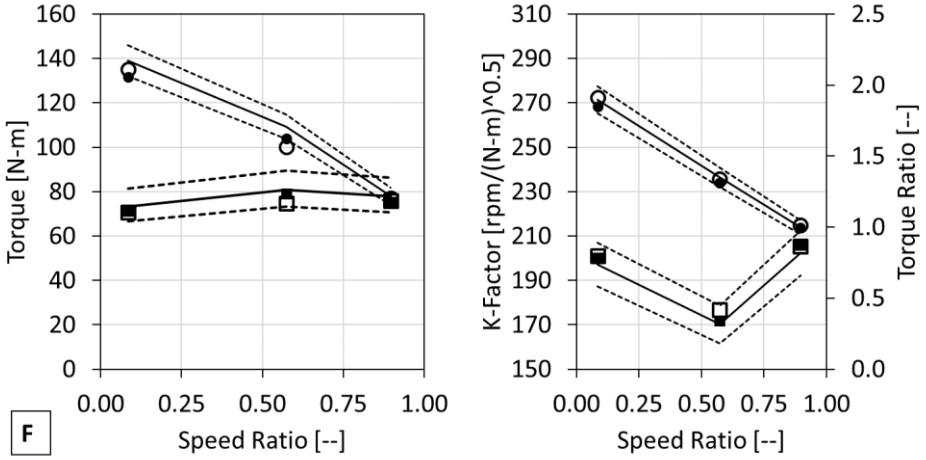

Figure 4-18. Simulated torques vs test for 6th gear with 75 N-m target impeller torque and non-dimensional values for full TC simulation (filled markers), torus only (white markers), test (solid line) and factory tolerance (dashed lines).

August 23 2018 tests

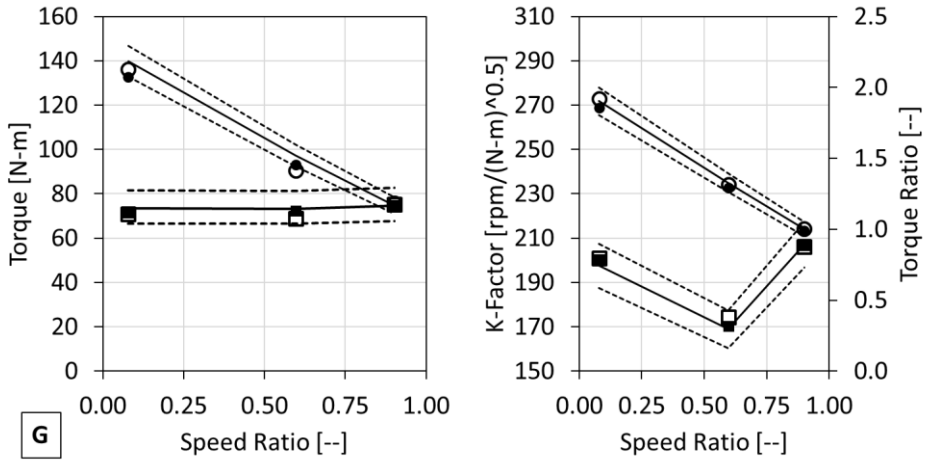

Figure 4-19. Simulated torques vs test for 5th gear with 75 N-m target impeller torque and non-dimensional values for full TC simulation (filled markers), torus only (white markers), test (solid line) and factory tolerance (dashed lines).

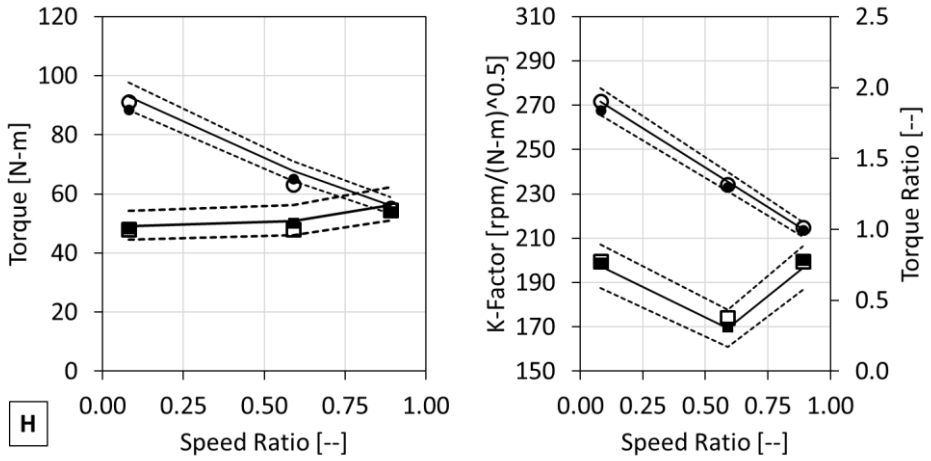

Figure 4-20. Simulated torques vs test for 6th gear with 50 N-m target impeller torque and non-dimensional values for full TC simulation (filled markers), torus only (white markers), test (solid line) and factory tolerance (dashed lines).

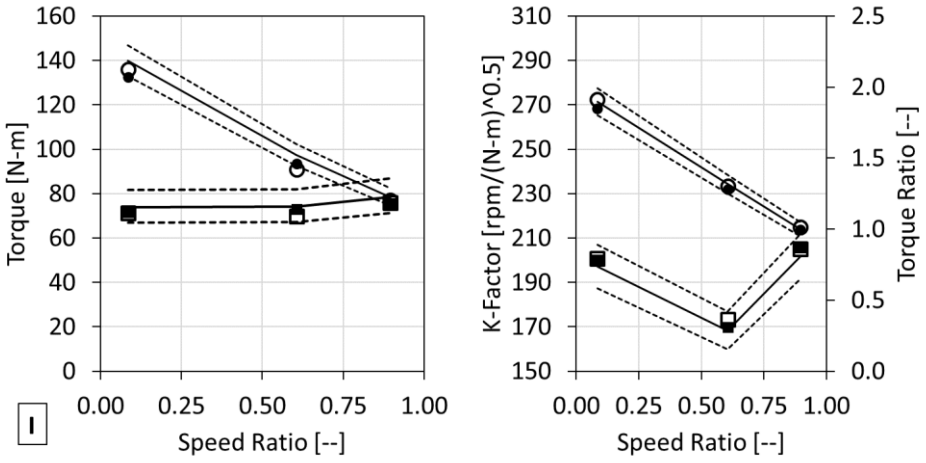

Figure 4-21. Simulated torques vs test for 6th gear with 75 N-m target impeller torque and non-dimensional values for full TC simulation (filled markers), torus only (white markers), test (solid line) and factory tolerance (dashed lines).

Overall, the full torque converter model improved the accuracy of the torque predictions for all speed ratios on the impeller. For the turbine, the torus only model was more accurate on the lower speed ratios. Nonetheless, a torus only model seems like a good first step to take when designing a new torque converter followed by a full 3-D model of the entire converter once the structure of the design is known.

4.4 Turbulence Intensity and Multiphase Effects on Simulation

Pressure transducers inside the torque converter measured absolute pressure while the pressures for the transmission instrumentation measured gauge pressures. For the results presented here, TCH11 was used as torque converter inlet pressure due to its location. An atmospheric pressure of 101,170 Pascals was subtracted from all telemetry channels to maintain commonality with the transmission measurements.

Three different simulation methods will be presented. The first method is a default method with turbulence intensity (TI) of 5%. The second uses multiphase to try to close the gap between test and CFD pressures. The third and last one uses various TI settings to reduce the error between the simulations and the test.

Line pressure in a transmission dictate the pressure settings of the rest of the systems. Line pressure settings ranging from 909 kPa to 2197 kPa were studied. The full torque converter model was used to correlate torque as well as pressures inside the different instrumented cavities. A representation of the low pressure settings and a representation of the high pressure settings for 5^{th} gear and 6^{th} will be used to show the accuracy of the computer model. The chosen tests were performed in August 8 and August 23 2018. Those dates offer a good combination of low and high pressure settings for 5^{th} and 6^{th} gear (Table 4-2).

Table 4-2. Conditions for the 75 N-m input torque at 5th and 6th gear tests with high and low pressure conditions.

Study Variable	5th Gear		6th Gear	
Line [kPa]	2197 (Aug. 8)	960 (Aug. 23)	1697 (Aug. 8)	934 (Aug. 23)
Speed Ratios	0.08 0.55 0.90	0.08 0.60 0.90	0.08 0.55 0.90	0.08 0.61 0.9
TC Inlet [kPa]	595 581 587	306 272 269	482 452 456	297 258 265
TC Outlet [kg/s]	0.153 0.154 0.153	0.098 0.099 0.100	0.135 0.135 0.135	0.097 0.097 0.096
Impeller [rpm]	1725 1572 1802	1693 1446 1790	1754 1600 1795	1694 1449 1788
Stator [rpm]	0 0 300	0 0 300	0 0 300	0 0 300

Turbulence intensity is defined as the root mean square of the fluctuation of the flow speed divided by the average speed (Equation 4-1).

$$TI = \frac{u'}{\overline{U}} = \frac{\sqrt{1/n \sum_{i=1}^{n} (u_i')^2}}{1/n \sum_{i=1}^{n} U_i} = \frac{RMS(u')}{U_{average}} \qquad \text{Equation 4-1}$$

For better understanding the concept, is always best to visualize it graphically (Figure 4-22).

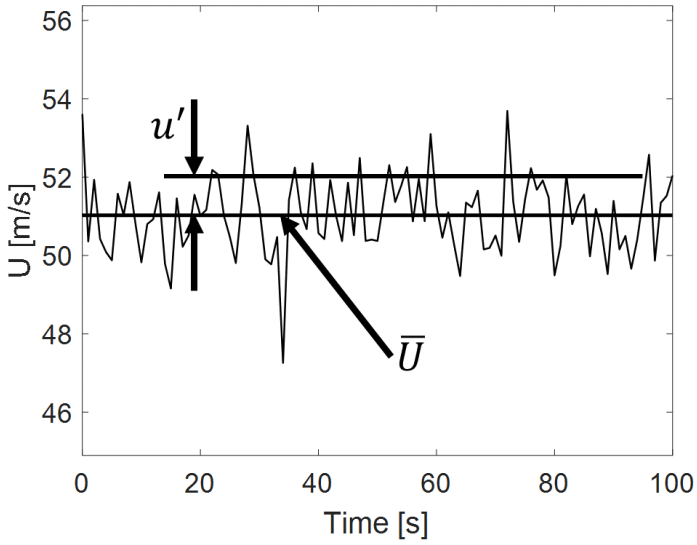

Figure 4-22. Graphic visualization of turbulence intensity.

For the multiphase studies, a Zwart-Gerber-Belamri homogeneous model was used [70]. The reasoning behind the use of a multiphase model is to determine if cavitation occurred during testing. Water vapor properties were used as the gaseous phase in the analysis (Table 4-3).

Table 4-3. Default multiphase model for the model.

Vapor pressure [Pa] [37]	3540
Bubble diameter [m]	1E-6
Nucleation Site volume fraction	0.0005
Evaporation coefficients	50
Condensation Coefficient	0.01
Density [kg/m^3]	1.225
Dynamic Viscosity [Pa-s]	1.7894 e-5

The simulation was set up in such a way that no vapor was entering or leaving the torque converter. Instead, the formation of air cavities will be dictated or determined by the

conditions inside the torque converter during the simulation. If cavitation is present, vapor will form in several locations inside the torque converter. Cavitation bubbles are the result of a sudden local pressure change. Cavitation bubbles will appear once the local pressure drops below the vaporization pressure. Previous cavitation studies inside torque converters have been studied in the laboratories at Michigan Technological University [71-75]. The speeds in which cavitation occurs depends on size and geometry of the torque converter as well as operating speeds and pressures. Onset of cavitation has been reported to occur inside torque converters with impeller speeds as low as 1500 rpm at stall (SR=0) [72]. The use of the multiphase model in the present study is an attempt at studying the aeration and formation of gas pockets in the oil and understand its effects on torque and static pressure.

To help determine what turbulence intensity levels should be considered, a look at average flow velocities can be easily done for the different locations at the torque converter inlet, clutch cavity and inside the torus using average values. Reynolds number will show flow turbulence levels and will help explain the decision to study different turbulence intensities (Equation 4-2).

$$Re = \frac{\rho u D_{hyd}}{\mu}$$ Equation 4-2

Where Re represent Reynolds number (non-dimensional), ρ density in [kg/m^3], u represents the fluid velocity in [m/s], μ is the dynamic viscosity in [Pa-s] and D_{hyd} is the hydraulic diameter in [m] (Equation 4-3).

$$D_{hyd} = \frac{4Area}{Wet\ Perimeter}$$ Equation 4-3

A study on the flow velocity for each of the cavities needs to be done to understand flow conditions. On average, the flow velocity entering the torque converter was 5 m/s. However, by the time it reached locations instrumented in the clutch cavity, the velocity drops dramatically (Figure 4-23).

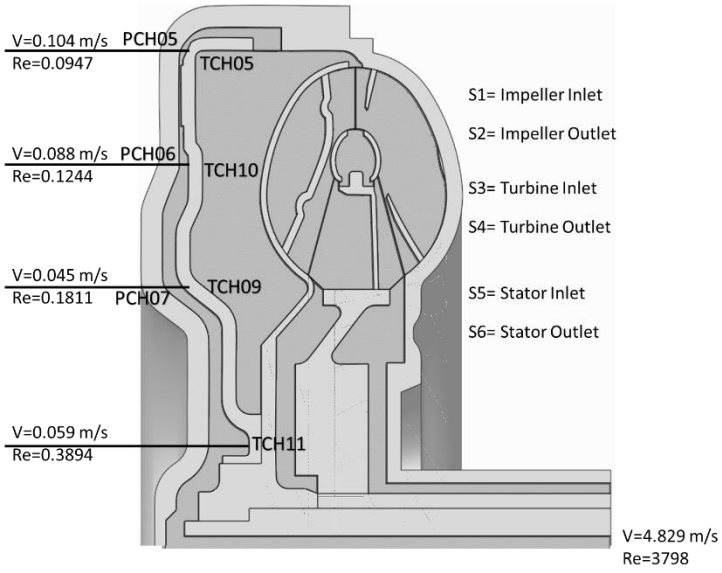

Figure 4-23. Flow velocity in the entrance/clutch cavity of the torque converter.

Conditions inside the torus are more turbulent. On average, flow velocity around the torus was 8 m/s. Other locations such as the turbine exit reached velocities as high as 13 m/s (Table 4-4).

Table 4-4. Average flow velocities [m/s] inside the torus cavity.

	Impeller			Turbine			Stator		
SR [--]	S1	Mid	S2	S3	Mid	S4	S5	Mid	S6
0.08	6.9	5.2	8.8	16.7	8.5	13.3	14.5	7.8	10.5
0.55	7.7	5.6	7.2	13.4	6.7	10.5	6.0	6.3	7.3
0.90	7.4	4.9	7.0	8.6	5.1	7.3	6.0	6.0	6.4

Reynold's numbers for the average flow velocities inside the torus are more turbulent than at the inlet cavities shown in Figure 4-23 (Table 4-5).

Table 4-5. Average Reynold's numbers [--] inside the torus cavity.

	Impeller			Turbine			Stator		
SR [--]	S1	Mid	S2	S3	Mid	S4	S5	Mid	S6
0.08	21400	12076	27943	58850	17083	45972	52875	22402	37404
0.55	20837	11268	19843	40863	11745	31496	19017	15518	22648
0.90	18012	8944	17569	23848	8031	19818	17269	13433	17780

For the present study, two TI settings and the multiphase conditions are in Table 4-6.

Table 4-6. Turbulence intensity and multiphase simulation settings description.

Turbulence intensity studies			
SR	Default	Modified	Multiphase
0.08	5%	50%	OFF
0.60	5%	5%	OFF
0.90	5%	0.50%	OFF
Multiphase study			
SR	Default	Modified	Multiphase
0.08	5%	--	ON
0.60	5%	--	ON
0.90	5%	--	ON

4.4.1 Accuracy of the Predicted Torques

Different turbulence intensity settings and the multiphase models did not affect the accuracy of the predicted torques, K-factor or torque ratio (Figure 4-24).

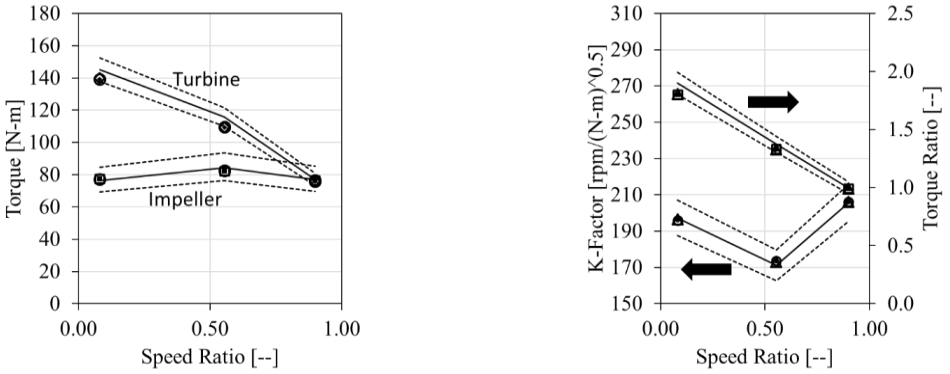

(a) (b)

Figure 4-24. Torque (a), default TI (black squares and diamonds), modified TI (white squares and diamonds), multiphase (white circles). K-Factor and torque ratio (b), default TI (black circles and squares), modified TI (white circles and squares) and multiphase (white triangles) , 5th gear, high pressure settings, black solid and dashed represent experimental values and tolerance bands respectively.

The picture demonstrate that either TI or multiphase affected the torque predictions. The remaining figures confirms the observations about the TI and multiphase settings (Figure 4-25 - Figure 4-27).

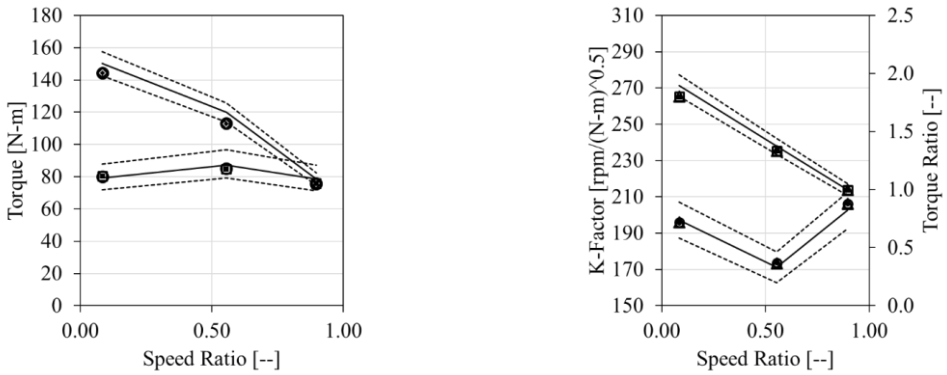

(a) (b)

Figure 4-25. Torque (a), default TI (black squares and diamonds), modified TI (white squares and diamonds), multiphase (white circles). K-Factor and torque ratio (b), default TI (black circles and squares), modified TI (white circles and squares) and multiphase (white triangles) during 6th gear with high pressure settings, black solid and dashed represent experimental values and tolerance bands respectively.

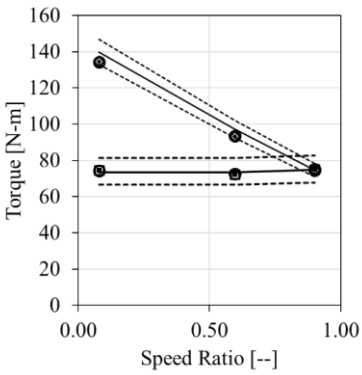

(a)

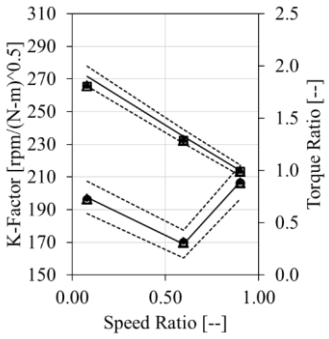

(b)

Figure 4-26. Torque (a), default TI (black squares and diamonds), modified TI (white squares and diamonds), multiphase (white circles). K-Factor and torque ratio (b), default TI (black circles and squares), modified TI (white circles and squares) and multiphase (white triangles) during 5th gear with low pressure settings, black solid and dashed represent experimental values and tolerance bands respectively.

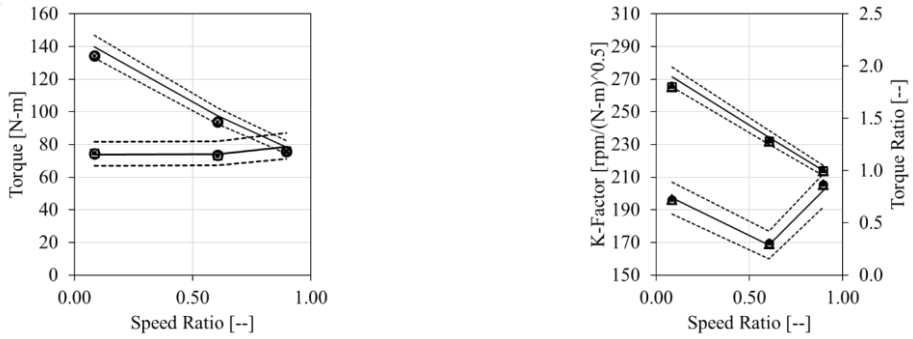

(a) (b)

Figure 4-27. Torque (a), default TI (black squares and diamonds), modified TI (white squares and diamonds), multiphase (white circles). K-Factor and torque ratio (b), default TI (black circles and squares), modified TI (white circles and squares) and multiphase (white triangles) during 6th gear with low pressure settings, black solid and dashed represent experimental values and tolerance bands respectively.

The presented figures in this sub-chapter demonstrates that considering turbulence intensity or multiphase in the simulation do not influence the predicted torques.

Having demonstrated the repeatability of the model to predict torque, it is now time to evaluate the predicted pressures when compared to test measurements.

4.4.2 Accuracy of the Simulated Pressures

The analysis was broken down by monitor points located in the toroidal cavity, TC inlet cavity (below friction disc) and turbine/pressure plate cavity (above friction disc) (Figure 4-28, Figure 4-29 and Figure 4-30).

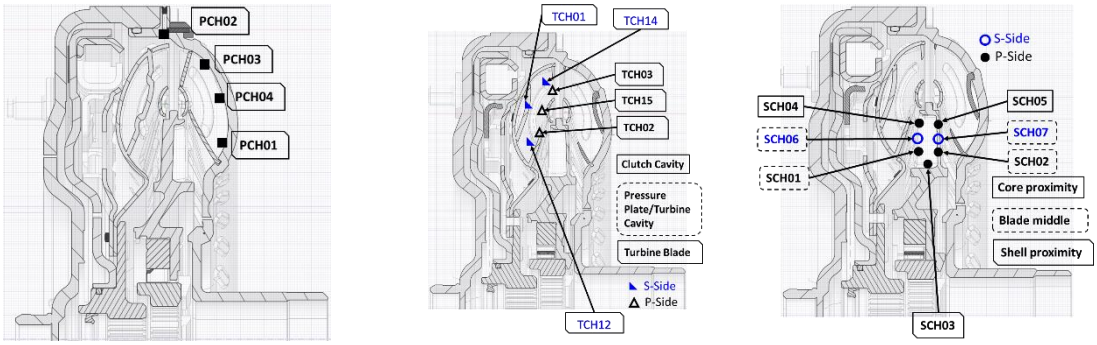

(a) (b) (c)

Figure 4-28. Toroidal cavity monitor points location per transmitter, impeller (a), turbine (b) and stator (c).

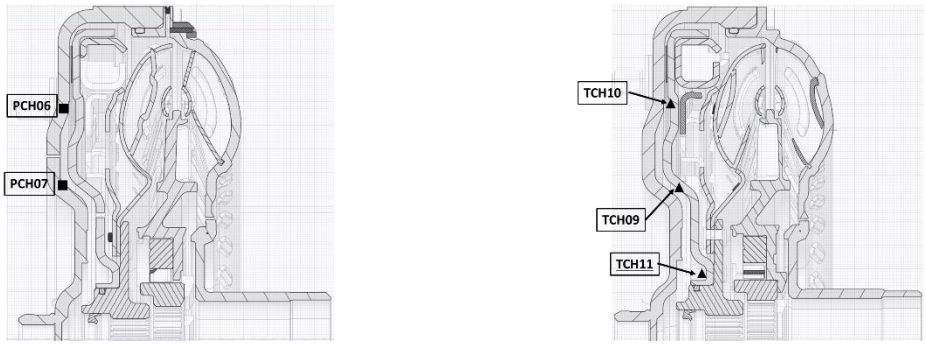

(a) (b)

Figure 4-29. TC inlet cavity monitor points location per transmitter, impeller (a), turbine (b).

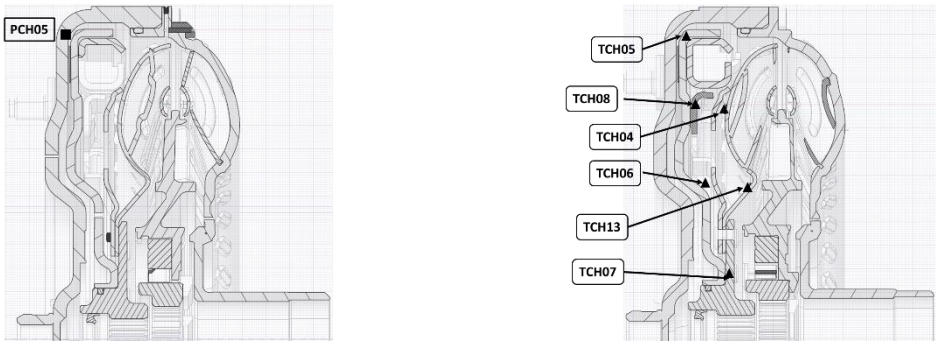

(a) (b)

Figure 4-30. Turbine and pressure plate cavity monitor points location for the impeller (a) and turbine (b) transmitters.

Although TCH07 is shown above, its location in the simulation was not possible since there are no mesh elements in such tight space between the pressure plate and the turbine hub.

August 8 2018 test 5th Gear High Pressure Settings

The experimental conditions were previously presented in Table 4-1 and Table 4-2. The simulated speed ratio conditions were presented in Table 4-6 and the multiphase parameters in Table 4-3. A comparison was then made by over plotting the test and the three simulations to determine if either simulation setting affected the predicted pressures (Figure 4-31).

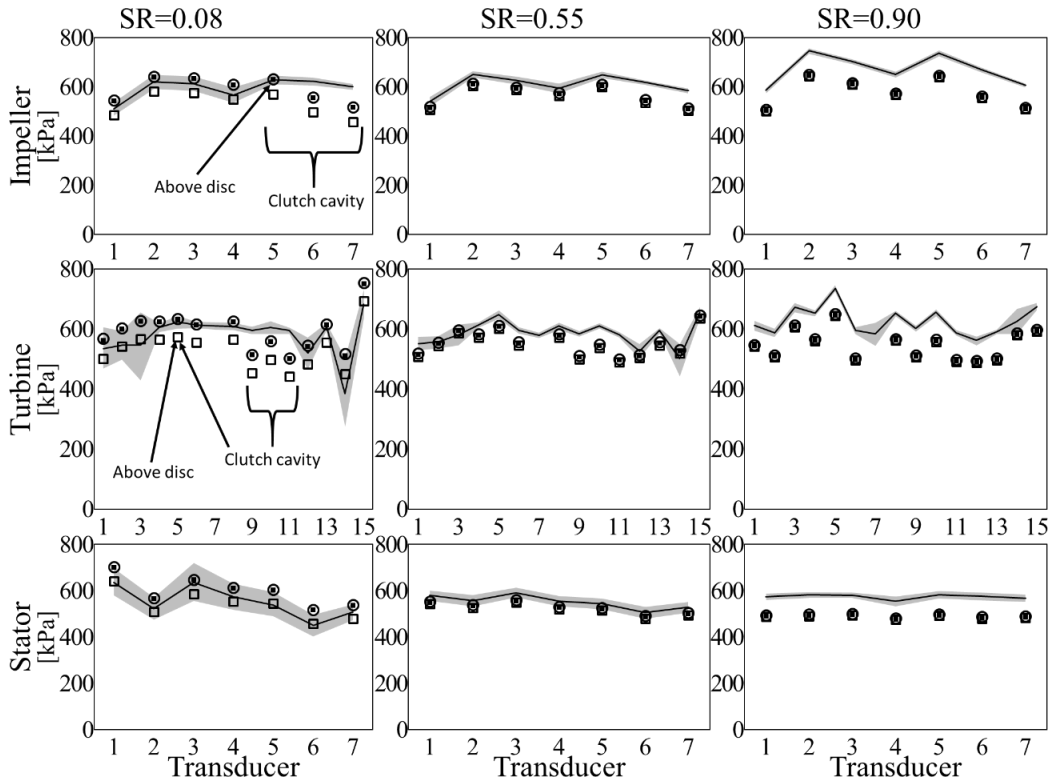

Figure 4-31. Experimental pressures (black line) vs default TI settings (circles), modified TI (squares) and multiphase settings (black squares) for the 5th gear high pressure settings at various SR's, gray areas represent fluctuation in the measurements.

An overall look at the figure shows good correlation between test and simulation at the low and middle speed ratio for all three instrumented groups while the simulation under-predicted pressures at the higher one.

Torus Cavity

Modifying turbulence intensity resulted lower RMSE for the low speed ratio in the torus cavity while default turbulence intensity performed best for the two higher ones (Figure 4-32).

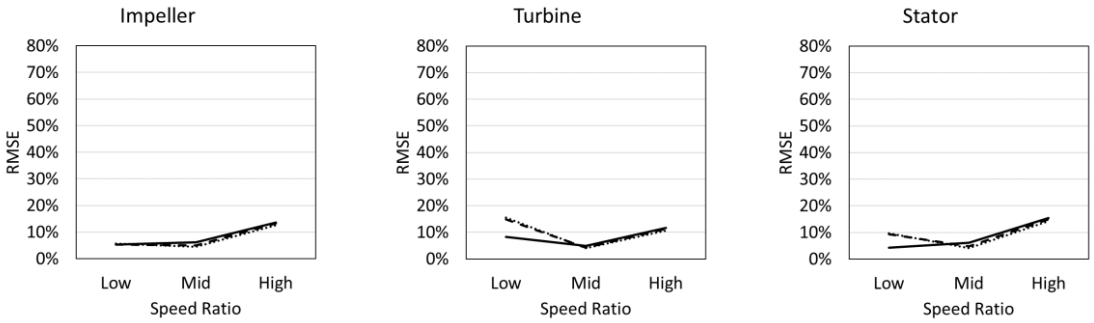

(a) (b) (c)

Figure 4-32. RMSE for toroidal cavity for impeller (a), turbine (b) and stator (c) transmitters, default TI (dashed), modified TI (solid) and multiphase (dotted).

When comparing the three simulation methods, the impeller toroidal cavity performed slightly better with the multiphase settings for all three speed ratios. The turbine toroidal cavity at low speed ratio performed best with the modified turbulence intensity while for the mid and high speed ratio, either method could be used with minor differences. The stator toroidal cavity showed similar behavior as the turbine. The results seen on the first simulation showed better pressure predictions were obtained with a modified turbulence intensity.

A small advantage was seen with the multiphase settings for the mid or higher speed ratios. The simulation is predicting the trends (peaks and valleys) found during testing very closely.

TC Inlet Cavity

When looking at numerical RMSE values, for the torque converter inlet cavity below the clutch disc, default settings and multiphase performed best for all three speed ratios (Figure 4-33).

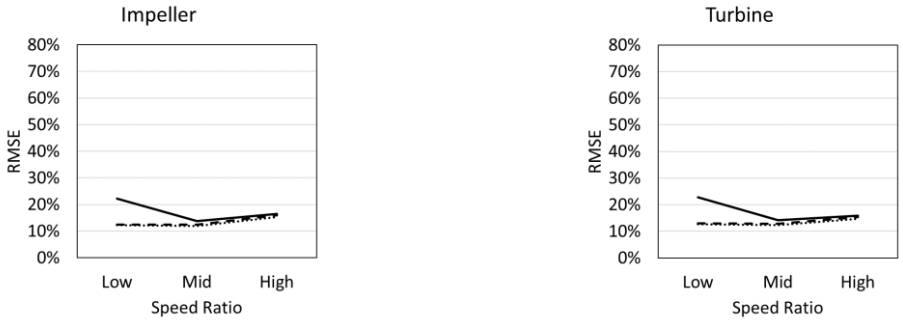

(a) (b)

Figure 4-33. RMSE for TC inlet cavity for impeller (a) and turbine (b) transmitters, default TI (dashed), modified TI (solid) and multiphase (dotted).

Conditions at the torque converter inlet cavity are not as turbulent as inside the torus. The default turbulence intensity or the multiphase resulted in similar pressure predictions. Differences between multiphase and default turbulence intensity may be due to computational or numeric errors.

Pressure Plate/Turbine Cavity

Once more, either default settings or multiphase could be used to predict conditions in the last of the instrumented cavities (Figure 4-34).

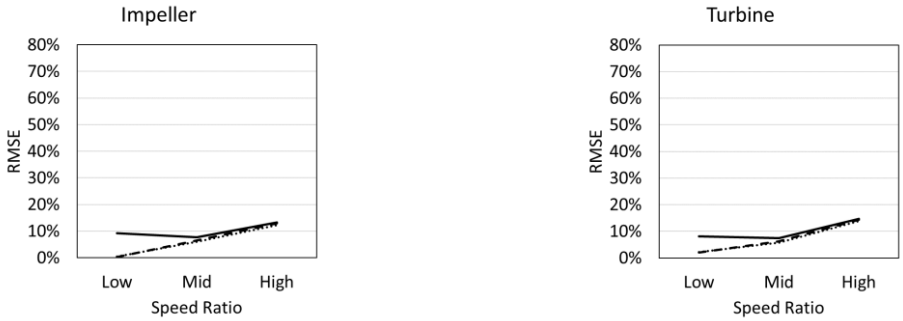

(a) (b)

Figure 4-34. RMSE for the pressure plate/turbine shell cavity on the impeller (a) and turbine (b) transmitters, default TI (dashed), modified TI (solid) and multiphase (dotted).

For all three speed ratios, conditions in the torque converter cavity between the turbine and the pressure plate are better predicted with the default or multiphase settings.

August 8 2018 test 6th Gear High Pressure Settings

A look at the 6th gear experiments with high pressure settings showed similar findings to the 5th gear ones (Figure 4-35).

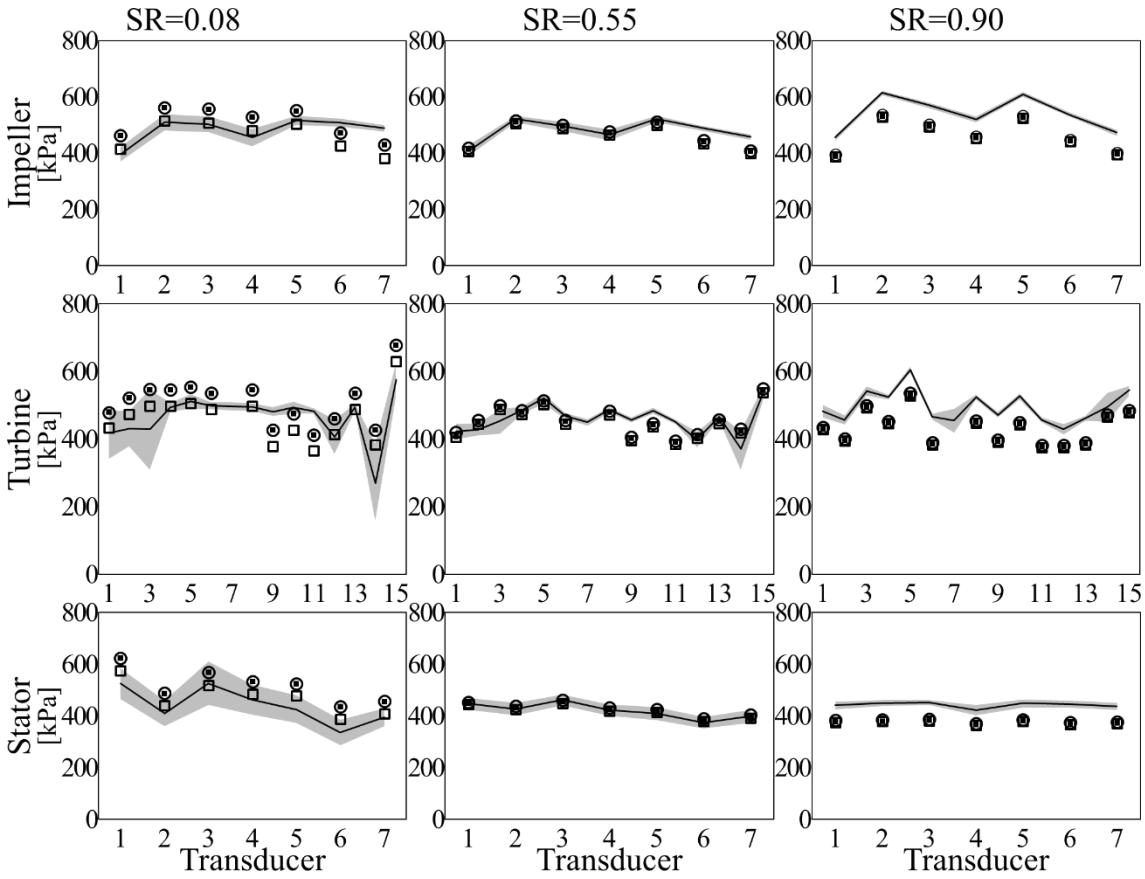

Figure 4-35. Experimental pressures (black line) vs default TI settings (circles), modified TI (squares) and multiphase settings (black squares) for the 6th gear high pressure settings at various SR's, gray areas represent fluctuation in the measurements.

An overall look at this new simulation shows again that better predictions for monitor points located past the friction disc were obtained when the turbulence intensity was modified. Once more, conditions at the mid speed ratio matched closer the ones in the

experiment while the higher speed ratio, although still under predicting pressures, it moved closer to the measurements. Peaks and valleys are still being predicted by the model.

Torus Only Cavity

Pressures inside the torus for the low speed ratio were better predicted with the modified turbulence intensity settings (Figure 4-36).

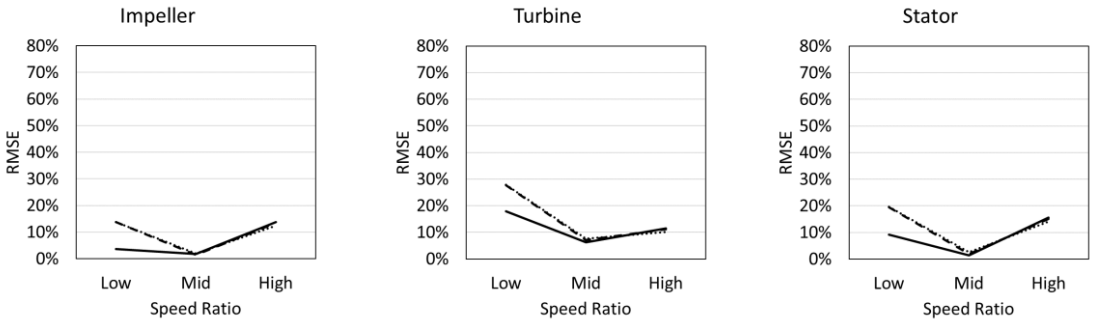

(a) (b) (c)

Figure 4-36. RMSE for toroidal cavity for impeller (a), turbine (b) and stator (c) transmitters, default TI (dashed), modified TI (solid) and multiphase (dotted).

As seen before, no noticeable difference between default and multiphase settings can be seen again. The experiments show more than 100 kPa pressure difference between 5th and 6th gear high pressure settings (Table 4-2). As a result, the torque converter operates at a lower oil "stiffness" promoting conditions that are more turbulent, which is why the modified turbulence intensity better predicted conditions inside the torus at the low speed ratio. The other two speed ratios could be modeled with any of the three methods.

TC Inlet Cavity

As seen in the previous study, flow conditions in the TC inlet cavity are not as turbulent as inside the torus (Figure 4-37).

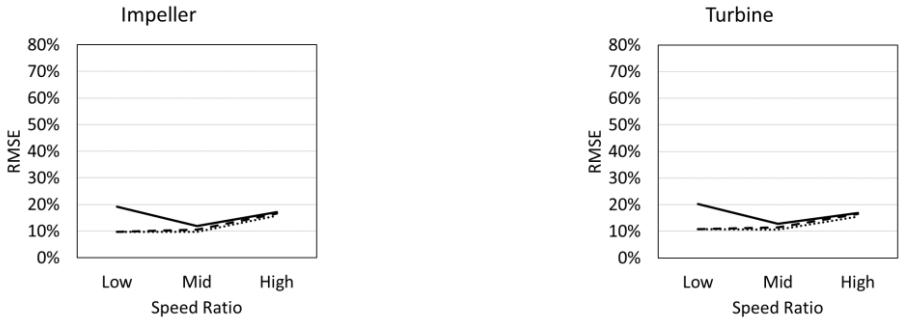

(a) (b)

Figure 4-37. RMSE for TC inlet cavity for impeller (a) and turbine (b) transmitters, default TI (dashed), modified TI (solid) and multiphase (dotted).

The results at the TC inlet are better predicted with either the default settings or the multiphase ones. Out of the three methods studied, the multiphase showed slightly lower errors as seen in the previous study. It is now clear that transducers located below the friction disc are not turbulent when compared to conditions past the friction disc and turbulence intensity could be left at 5% (default) for the low speed ratio or multiphase settings could be used.

Pressure Plate/Turbine Cavity

Opposite to the conditions in 5th gear with high pressure settings. Under this slightly lower pressure setting on 6th gear, the transducers between the turbine and the pressure plate while running at the low speed ratio were better simulated with a modified turbulence intensity (Figure 4-38).

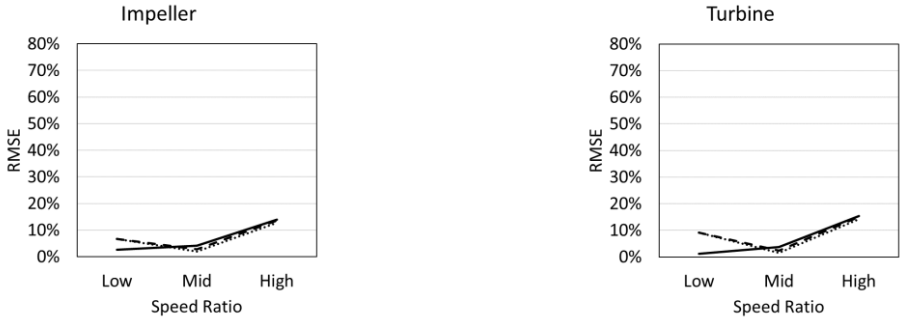

(a) (b)

Figure 4-38. RMSE for the pressure plate/turbine shell cavity on the impeller (a) and turbine (b) transmitters, default TI (dashed), modified TI (solid) and multiphase (dotted).

For the two higher speed ratios, the flow conditions inside the torque converter are not as turbulent as the low speed ratio, for that reason, either the multiphase or the default settings could be used to simulate the pressures inside the cavity.

August 23 2018 test 5th Gear Low Pressure Settings

Under low pressure setting, the modified turbulence intensity moved the predictions closer to the experimental measurements. At the mid speed ratio, the simulation predicted correct pressures while at the higher speed ratio errors between test and simulation reduced when

compared to the simulations for the high pressure settings. The monitor points inside the clutch cavity that are below the friction disc are closer to the measurements and better predicted once more with default settings (Figure 4-39).

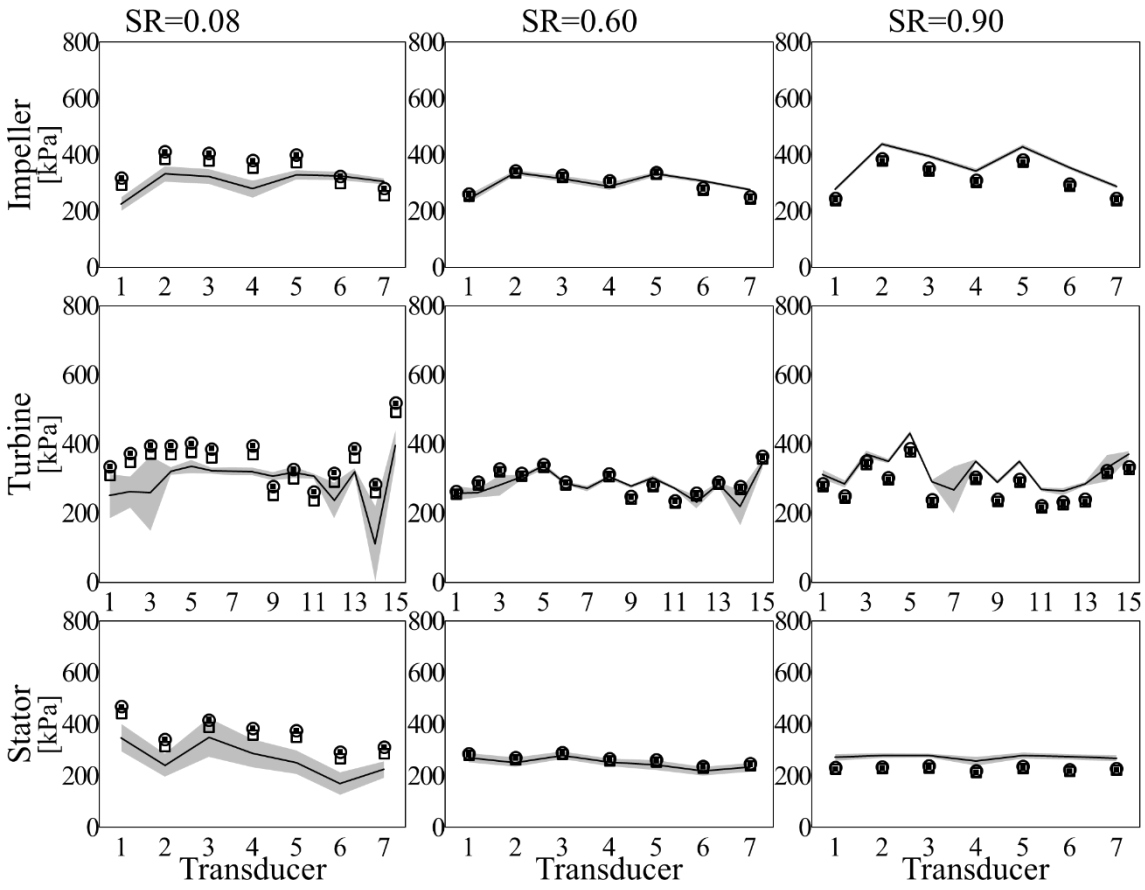

Figure 4-39. Experimental pressures (black line) vs default TI settings (circles), modified TI (squares) and multiphase settings (black squares) for the 5th gear low pressure settings at various SR's, gray areas represent fluctuation in the measurements.

Torus Only Cavity

The RMSE for the monitor points inside the torus cavity shows better predictions when the turbulence intensity is modified for two of the three speed ratios (Figure 4-40).

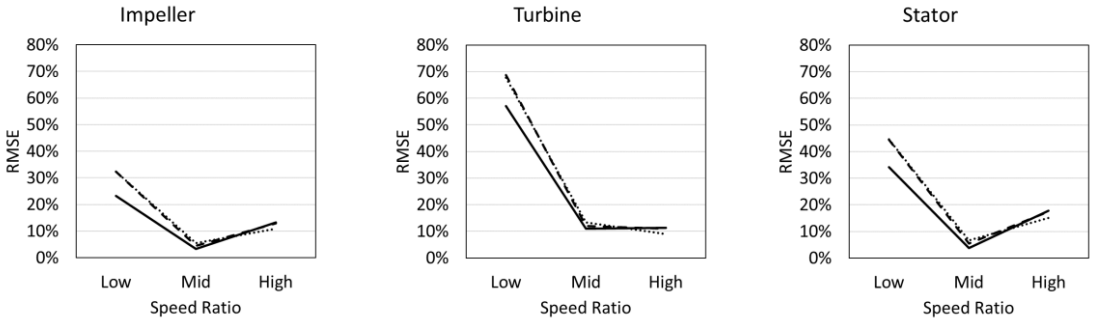

(a) (b) (c)

Figure 4-40. RMSE for toroidal cavity for impeller (a), turbine (b) and stator (c) transmitters, default TI (dashed), modified TI (solid) and multiphase (dotted).

The error magnitudes under low pressure operating points more than tripled for some of the pressure transducers at the low speed ratio. The mid speed ratio once again showed better correlation with experiments while the higher one reduced overall errors when compared to all previous studies. Conditions inside a torque converter with low pressure operating conditions result in increased turbulence and make simulations more difficult.

TC Inlet Cavity

The conditions at the torque converter inlet were better predicted with the default turbulence intensity settings or the multiphase (Figure 4-41).

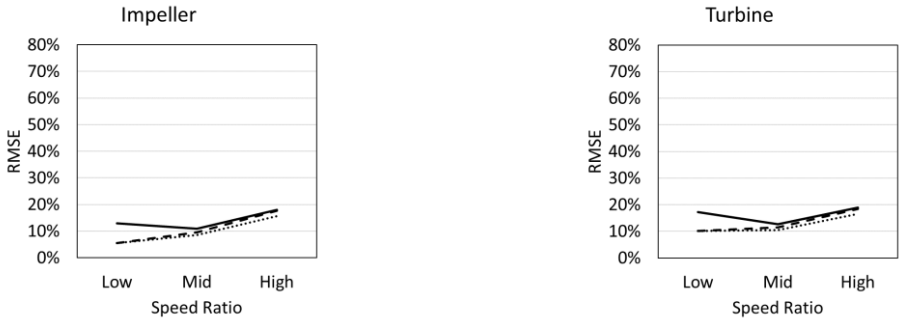

(a) (b)

Figure 4-41. RMSE for TC inlet cavity for impeller (a) and turbine (b) transmitters, default TI (dashed), modified TI (solid) and multiphase (dotted).

The results seen so far confirmed that conditions at the torque converter inlet are best described as low turbulence ones, while inside the torus, the flow is more turbulent.

Pressure Plate/Turbine Cavity

Conditions between the turbine and pressure plate are similar to the ones seen so far for all other experimental setting (Figure 4-42).

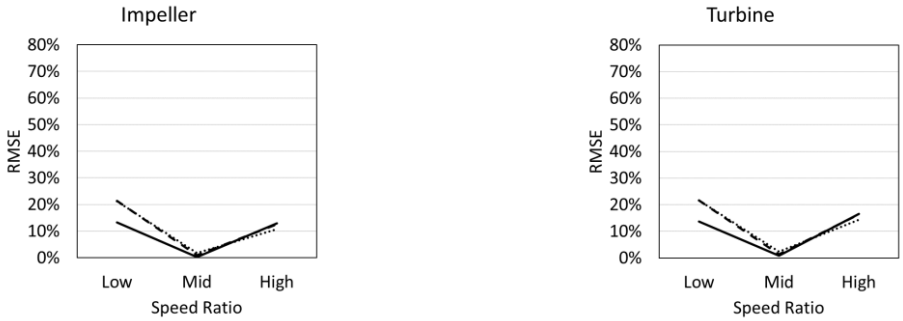

(a) (b)

Figure 4-42. RMSE for the pressure plate/turbine shell cavity on the impeller (a) and turbine (b) transmitters, default TI (dashed), modified TI (solid) and multiphase (dotted).

Under the low pressure settings, the cavity between the turbine and the pressure plate at the low speed ratio are best modeled with a modified turbulence intensity. The mid speed ratio under modified turbulence intensity also showed lower errors while the multiphase showed lower errors at the high one. Under low pressure settings the simulation fails at predicting reasonable errors across all experiments performed, especially inside the torus.

August 23 2018 test 6th Gear Low Pressure Settings

Finally, for the 6th gear low pressure settings, similar observations could be made (Figure 4-43).

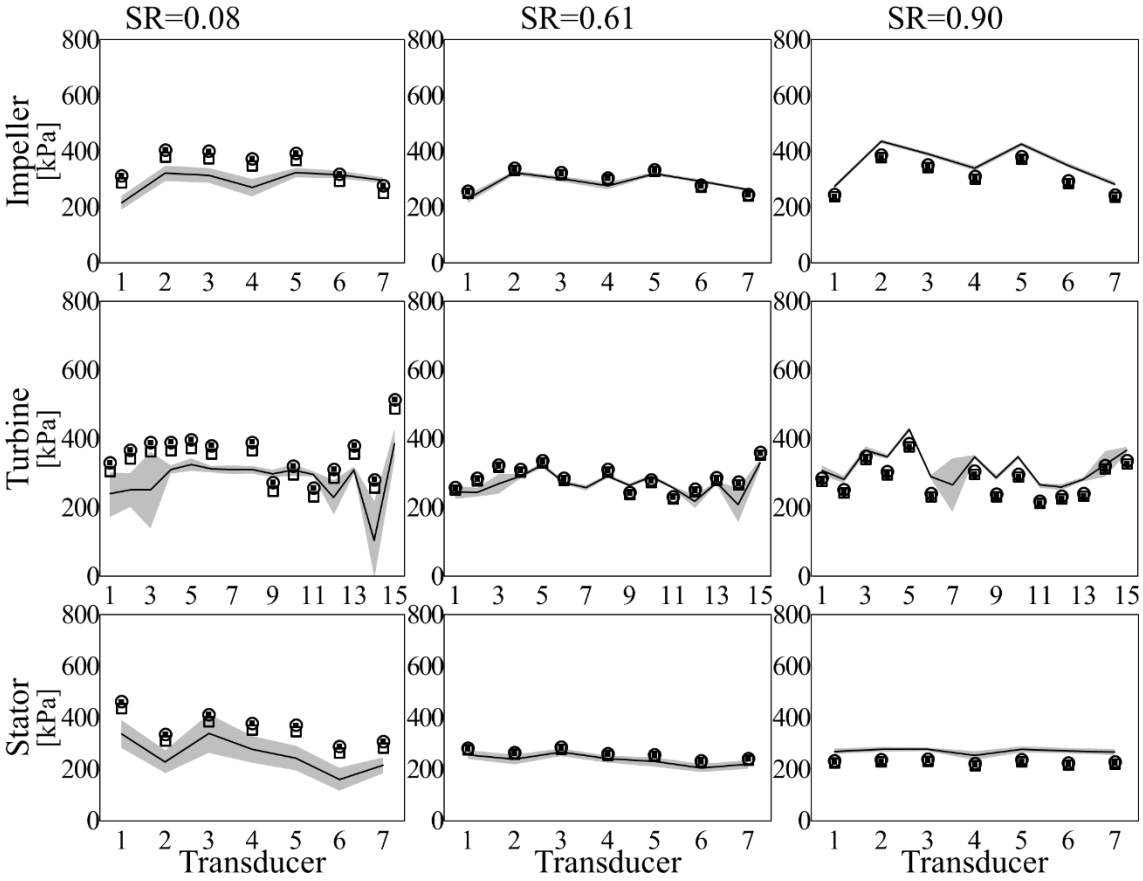

Figure 4-43. Experimental pressures (black line) vs default TI settings (circles), modified TI (squares) and multiphase settings (black squares) for the 6th gear low pressure settings at various SR's, gray areas represent fluctuation in the measurements.

Conditions inside the clutch cavity below the friction disc are again, best predicted with default settings while all other transducers are being influenced by higher turbulence

intensities. The highest speed ratio once again showed better prediction correlation with test when compared to the high pressure settings.

Torus Only Cavity

RMSE for low pressure settings increased by 5 times for the low speed ratio when compared to the high pressure settings (Figure 4-44).

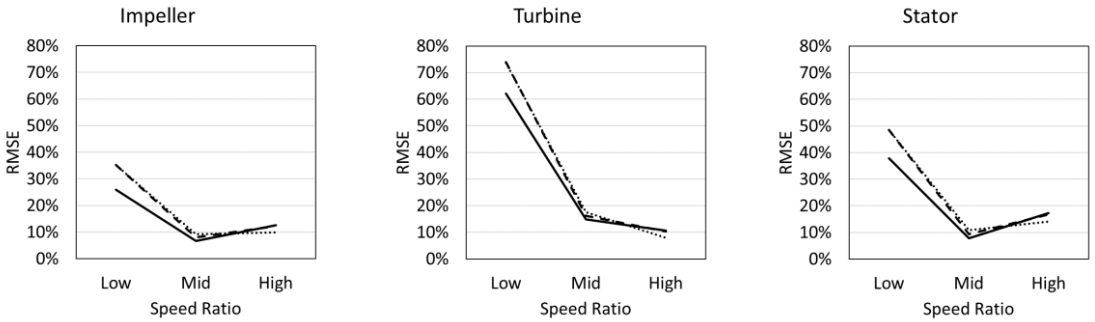

(a) (b) (c)

Figure 4-44. RMSE for toroidal cavity for impeller (a), turbine (b) and stator (c) transmitters, default TI (dashed), modified TI (solid) and multiphase (dotted).

The modified turbulence intensity best predicted conditions inside the torus again. The middle speed ratio showed better correlations with test once more. The higher speed ratio predictions have fewer errors for the low pressure tests when compared to the high pressure ones.

TC Inlet Cavity

As previously seen, the torque converter inlet flow conditions are not as turbulent as in the rest of the converter. Either multiphase or default settings could be used (Figure 4-45).

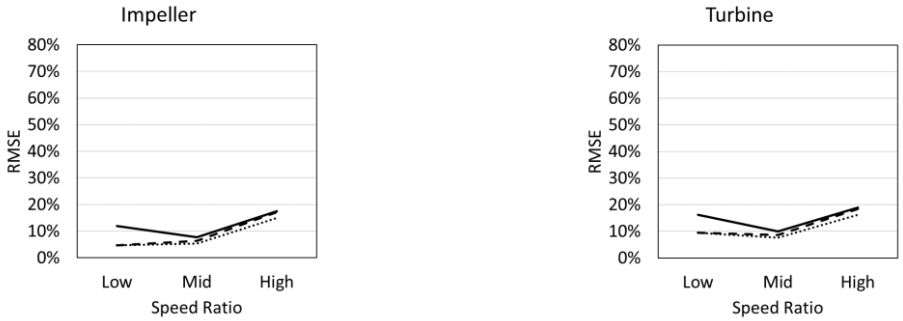

(a) (b)

Figure 4-45. RMSE for TC inlet cavity for impeller (a) and turbine (b) transmitters, default TI (dashed), modified TI (solid) and multiphase (dotted).

Pressure prediction errors are in the same order of magnitude as the ones seen so far for the inlet cavity below the clutch disc.

Pressure Plate/Turbine Cavity

This final pressure comparison confirms the findings seen so far for all simulations. Conditions in this cavity for low speed ratios are best simulated with turbulence intensity modifications (Figure 4-46).

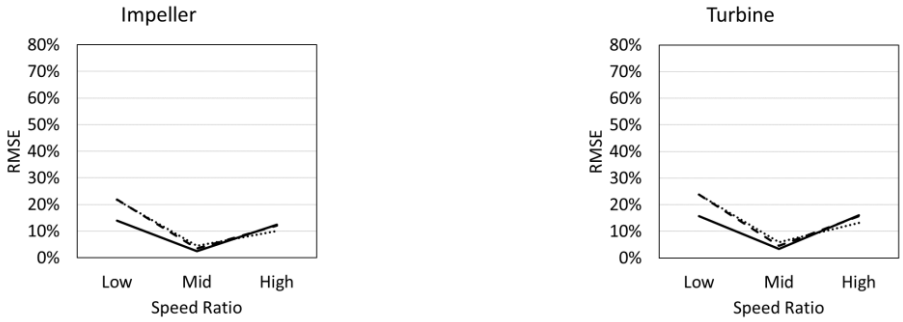

(a) (b)

Figure 4-46. RMSE for the pressure plate/turbine shell cavity on the impeller (a) and turbine (b) transmitters, default TI (dashed), modified TI (solid) and multiphase (dotted).

The mid speed ratio once again showed the best correlation. While the higher speed ratio had reduced errors when compared to the high pressure settings for 6th gear.

Overall, best pressure predictions were made at the middle speed ratio studied. For the low speed ratios, the computer model yields more accurate results with higher pressure settings than when lower pressure settings were used. The opposite was observed at the higher speed ratio, pressure predictions were best for the low pressure settings.

To help reduce errors between experiment and predictions inside the torus, an increased turbulence intensity is needed for the low speed ratios. This behavior is consistent with the high turbulent flows caused by the shearing of the oil under low speed ratio conditions inside the torus. Such turbulence, affect the pressures in the nearby cavities.

The study demonstrated that there is never a single recipe to model the conditions inside the torque converter. Areas of interest must be modeled to fit the conditions in those cavities.

The study also shows that higher turbulence inside the torus affected the conditions in the rest of the cavities in its proximity.

4.5 Cavitation Study

With the multiphase settings, cavitation inside the torque converter could be studied. An iso-baric surface (referred to as simply iso-surface) for the 3540 Pascals range will highlight areas affected by cavitation if any.

A brief study in search of a possible cavitation speed for the torque converter under study with the multiphase model set in Table 4-3 shows low pressure pockets at SR=0.08 for impeller speeds of 2000 and 3000 rpm. Areas of low pressure at the 2000 rpm condition are affecting scatter stator blades while at 3000 rpm, all blades show low pressure regions starting to develop and grow (Figure 4-47).

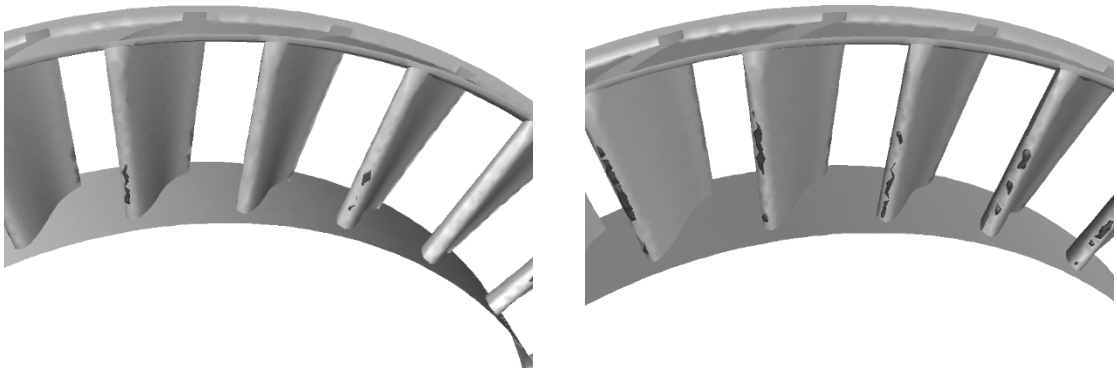

(a) (b)

Figure 4-47. Low pressure pocket formation on stator blades leading edge at impeller speeds of 2000 rpm (a) and 3000 rpm (b) during SR=0.08.

A look at the pressure contours can help visualize the areas of low and even negative gage pressures (Figure 4-48).

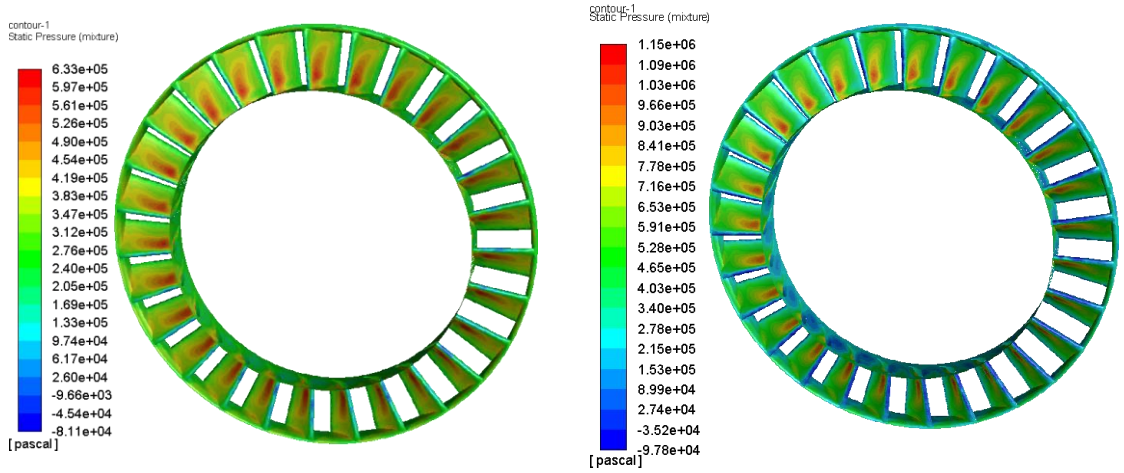

(a) (b)

Figure 4-48. Pressure contour on stator blades leading edge at impeller speeds of 2000 rpm (a) and 3000 rpm (b) during SR=0.08.

The contour plots show areas of low pressure that include the cavitation ranges (pressures around 3540 Pascals) for both impeller speeds. At 3000 rpm, even larger low pressure

regions can be appreciated. It is now clear that in order to start seeing cavitation formation for the torque converter under study, an impeller speed well above 3000 rpm is needed while at SR=0.08.

In order to confirm that cavitation was not present during the experiments completed, a look at the color maps for the tests of August 23 2018 at low pressure settings can be done. The reason for choosing the low pressure settings over the high pressure ones is because low operating pressures inside the torque converter help promote cavitation and its occurrence may be at lower speeds [72, 73]. The highest impeller speed during the August 23, 2018 experiments at SR=0.08 never exceeded 1694 rpm. Based on the results seen by the CFD, cavitation during the experiments is unlikely (Figure 4-49).

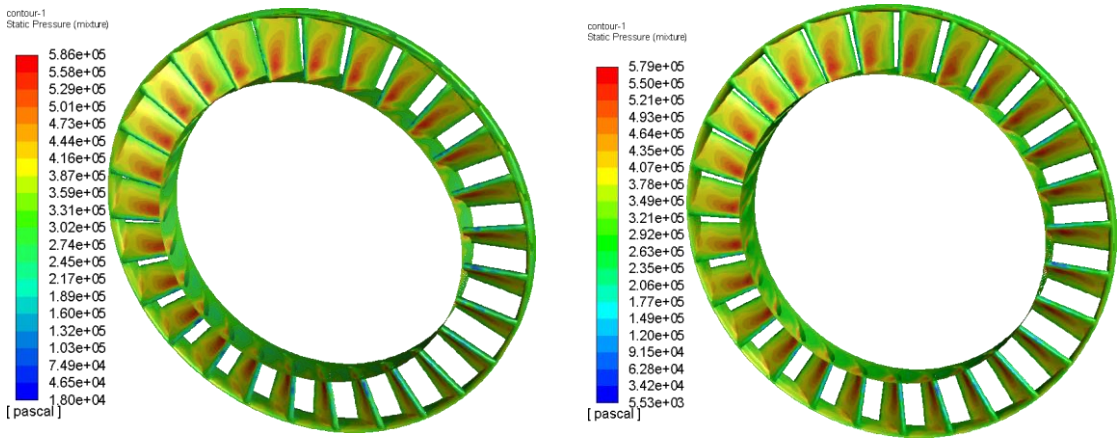

(a) (b)

Figure 4-49. August 23 2018 test in search of cavitation for low pressure settings on 5th gear (a) and 6th gear (b) during SR=0.08.

When looking at the pressure ranges as a result of the study, it can be seen the lowest pressure on the contour map is above 5530 Pascals. Above cavitation vapor pressure (3540

Pascals). From the findings it is confirmed, none of the measurements was affected by cavitation.

A proper CFD model to study cavitation will have to be carried out during future investigations to study this phenomenon in the torque converter under study. Cavitation studies was out of scope for the present investigation and the model presented was not optimized to study it.

4.6 Pressure Correlation, Blade Loading and Contours

Flow visualization for every test completed is redundant and pointless. For that reason, the flow visualization section will be completed for the analysis with the lower error levels. Simulations for the test completed on August 8 under high pressure conditions in 5th gear had lower error levels between tests and simulations.

4.6.1 Torus Cavity Pressure Correlation

Impeller Channel Pressures

Pressure patterns inside the impeller channel showed expected behavior for all three speed ratios (Figure 4-50).

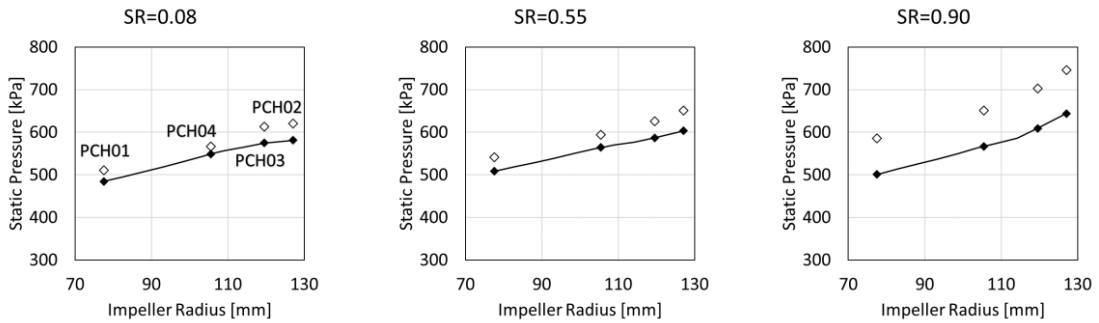

Figure 4-50. Impeller channel radial pressure distribution with the modified TI CFD settings for the CFD (black line & markers) and test (white markers).

Higher pressures were seen as the impeller radius increases as expected due to the impeller pumping mechanism. The trend seen on the experiments is repeated by the simulation. The magnitudes of the pressures for all three speed ratios remained relatively the same. That is also expected since the impeller maintained its rotational speed relatively similar across the three speed ratios. Under this particular experiment with high pressure settings, it can be seen that pressure is being under-predicted at the higher speed ratio. The lowest speed ratio had the best correlation of the three, while the mid speed ratio falls in second best. A look at the pressure contours for the impeller shows the gradient inside the impeller with higher pressures and tighter lines as the ATF moves outwards (Figure 4-51).

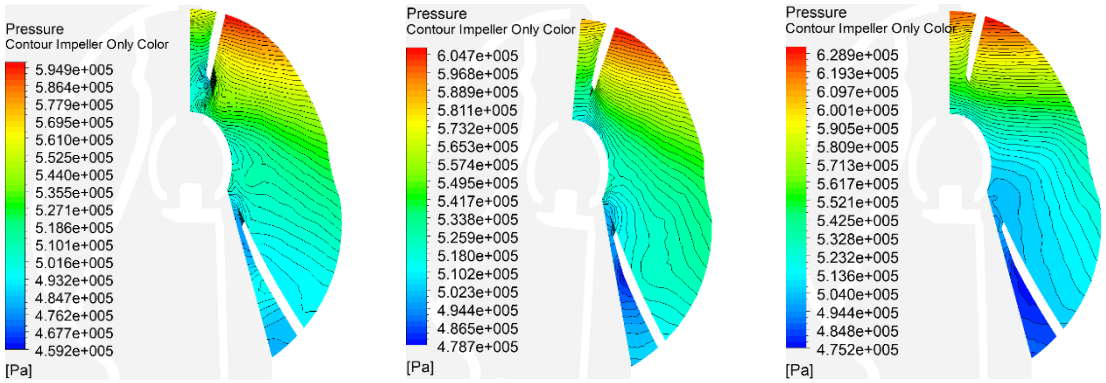

(a) (b) (c)

Figure 4-51. Impeller pressure contour for the August 8 2018 simulated pressures at SR=0.08 (a), SR=0.55 (b) and SR=0.90 (c).

The similarity of the contour plots for the impeller is expected. As explained earlier, the impeller ran without much speed variation throughout all tests. With the pressure contours is easier to see the rapid pressure changes across the impeller for the low speed ratio when compared to the other two higher speed ratios. Much of the pressure is gained after the second half of the impeller channel as seen with the pressure contours.

Turbine Blade Loading

The instrumentation on the turbine blade was done on the mid-stream as seen earlier in the chapter. The turbine blade was normalized in length from 0 to 1. The leading edge is represented by 0 meaning and 1 represents the trailing edge (Table 4-7).

Table 4-7. Normalized turbine blade.

Blade Side	Blade Length [mm]	IRT Nom.	Normalized Blade Length
Pressure	69.6587	TCH03	0.03
		TCH15	0.51
		TCH02	0.97
Suction	75.4824	TCH14	0.03
		TCH01	0.49
		TCH12	0.92

The pressure prediction trends inside the turbine matched the ones obtained with the measurements (Figure 4-52).

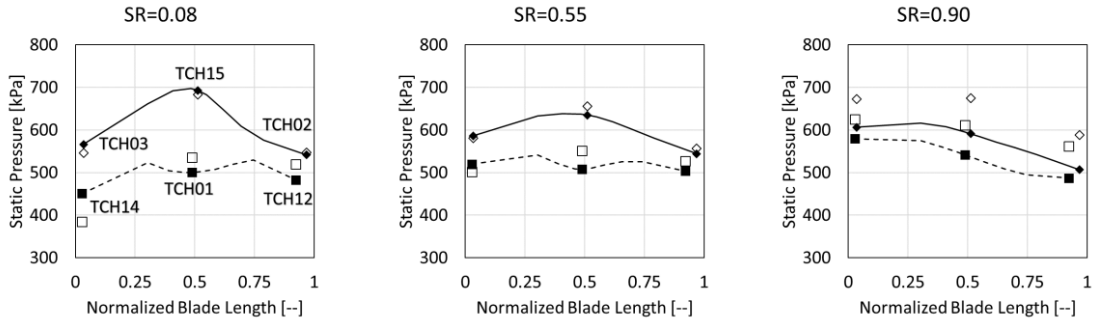

Figure 4-52. Turbine blade pressure distribution with the modified TI CFD settings at various speed ratios.

Higher pressures mid-span of the blade when compared to the leading edge for the lower 2 speed ratios is typical for high incidence angles. The restriction caused by the flow recirculation region occurring on the suction side has a Venturii effect on the turbine channel and affects both sides of the blade. This restricted flow results in low pressure regions occurring at the leading edge of the blades. Once the incidence angle of the flow decreases, the pressure pattern stabilizes as seen for the SR=0.9 where pressures at the leading edge are higher than downstream. This has been observed in previous studies [65].

A look at the pressure contours between blades show rapid pressure changes occurring as the ATF moves through the turbine near the pressure side more than near the suction side (Figure 4-53).

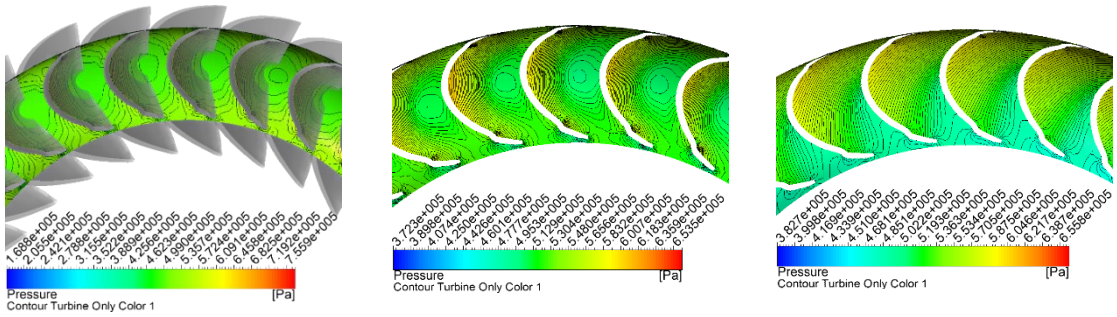

(a) (b) (c)

Figure 4-53. Turbine blade middle streamline pressure contour for the August 8 2018 simulated pressures at SR=0.08 (a), SR=0.55 (blades hidden) (b) and SR=0.90 (blades hidden) (c).

The circular patterns occurring at the mid-chord streamlines for the two lower speed ratios are caused by recirculation occurring inside the turbine passages leaving a very narrow gap near the pressure side of the blade (hidden) and the shell surface (Figure 4-54).

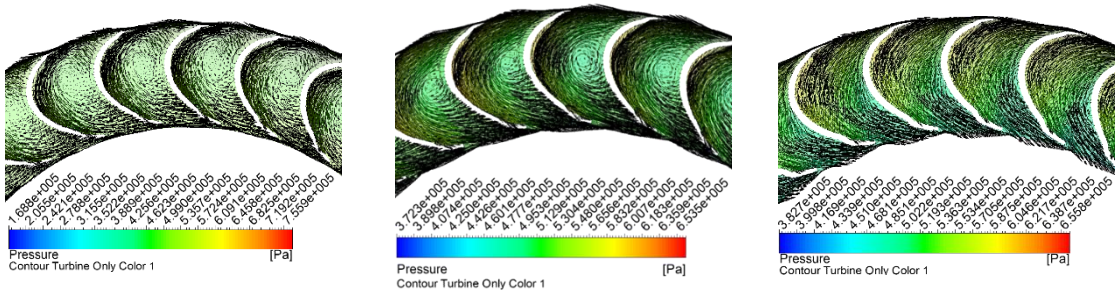

(a) (b) (c)

Figure 4-54. Turbine blade middle streamline pressure contour and recirculation vectors for the August 8 2018 simulated pressures at SR=0.08 (a), SR=0.55 (blades hidden) (b) and SR=0.90 (blades hidden) (c).

At the higher speed ratio, there is no recirculation region. The pressure contours and vector field show correct orientation from blade to blade indicating the toroidal flow enters the turbine inlet location and exits at the turbine exit as expected. The flow has the entirety of the area available without blockage and an iso-surface is not possible. An iso-surface for a constant pressure on the lower two speed ratios help visualize the size covered of the recirculation region across all three speed ratios (Figure 4-55).

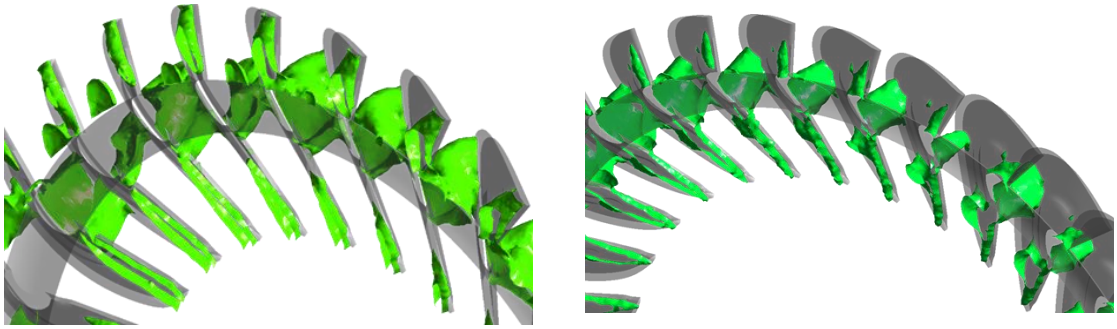

(a) (b)

Figure 4-55. Turbine iso-surface for constant 496 kPa pressure shows size of recirculation region at SR=0.08 (a), 509 kPa for SR=0.55 (b).

The recirculation region covers the corner between the core and suction sides of all blades as well as the leading and trailing edges of the turbine blade on the suction side. For the SR=0.55, the flow through the turbine channel increases as a result of the reduced circulation.

Stator Blade Loading

The stator blade was instrumented on streamlines close to the core, midstream and close to the shell. The mid-stream was instrumented on both sides of the blades while the core and shell streams were only instrumented on the pressure side. The stator blade was normalized as well from 0 to 1 (Table 4-8).

Table 4-8. Normalized stator blade.

Core Streamline			
Blade Side	Blade Length [mm]	IRT Nom.	Normalized Blade Length
Pressure	18.7128	SCH04	0.24
		SCH05	0.79
Middle Streamline			
Pressure	17.3940	SCH01	0.26
		SCH02	0.84
Suction	18.6913	SCH06	0.25
		SCH07	0.86
Shell Streamline			
Pressure	16.5487	SCH03	0.56

The test under study reflects the 5th gear under high pressure settings from August 8 2018. The CFD simulation helps to complete the gap and is complimented and validated by the instrumentation. Incidence angle affected the pressures seen by each side of the blade (Figure 4-56)

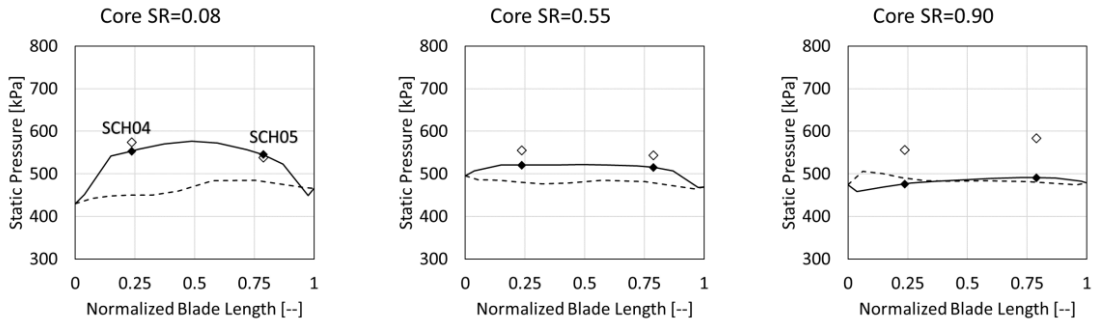

Figure 4-56. Stator blade simulated pressures for the pressure side (black diamonds), suction side (dashed squares) compared against experiments (white diamonds for the pressure side and white squares for suction) at various speed ratios for the streamline closer to the core.

The simulation for the core streamline predicted the trends seen by the measurements. Similar to the turbine, a separation region caused by high incidence angle reduces the available flow area resulting in low pressures closer to the leading edge when compared to the trailing edge of the streamline. On the higher speed ratio, the flow impacts the stator blade at the leading edge precisely on the suction side. This causes the pressure profiles for more than 25% of the blade to be inverted. This is due to the transition from multiplication to freewheel range. Past investigations have shown similar behavior for the stator blade [69].

The size of this inversion changes when moving from core to mid-stream of the stator blade. At the middle streamline, the flow impacts the suction side for a little under 25% of the blade. The CFD was also able to predict the trend observed with the experiments, high pressure difference across blade side for the low SR, middle size difference at the mid SR and essentially no pressure difference at the high SR (Figure 4-57).

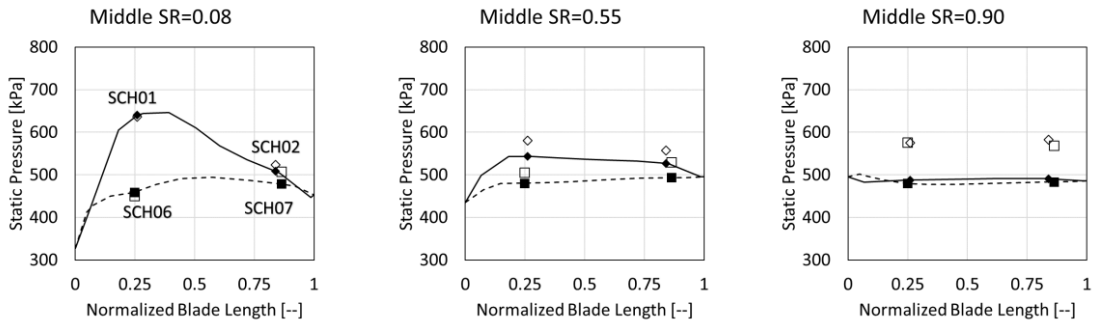

Figure 4-57. Stator blade simulated pressures for the pressure side (black diamonds), suction side (dashed squares) compared against experiments (white diamonds for the pressure side and white squares for suction) at various speed ratios for the middle streamline.

At the low speed ratio, the pressure difference across blade side is more noticeable than on the streamline closer to the core. The pressure difference across blade side, when integrated over the area could be used to calculate the torque [69].

On the streamline closer to the shell, the inverted pressure profile is not present for the SR=0.9 as seen with the core and middle streamline (Figure 4-58).

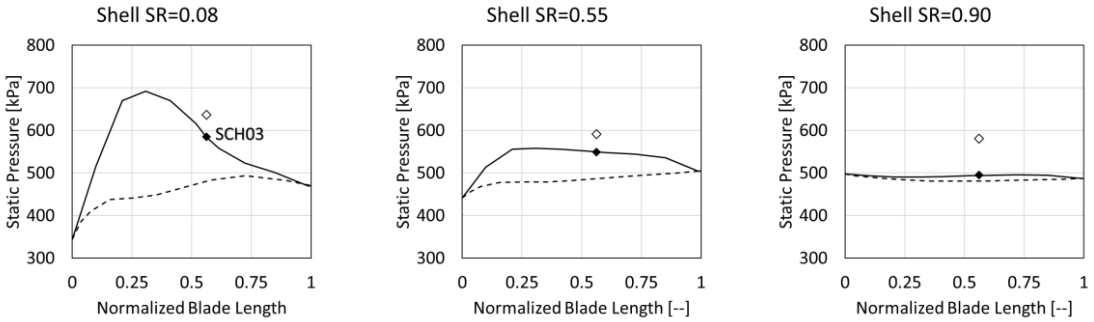

Figure 4-58. Stator blade simulated pressures for the pressure side (black diamonds), suction side (dashed squares) compared against experiments (white diamonds for the pressure side and white squares for suction) at various speed ratios for the streamline closer to the shell.

The pressure difference across blade side is larger on the shell than it was on the middle or core streamlines (Figure 4-59).

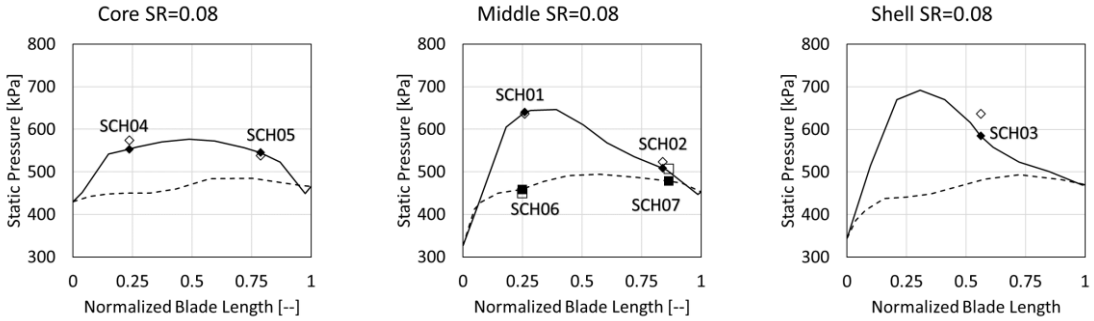

(a) (b) (c)

Figure 4-59. Pressure difference across blade surface for core (a), middle (b) and shell (c) streamline at SR=0.08.

A view at the contour lines show a very tight grouping at the leading edge of the blade at SR=0.08 compared to the other two speed ratios (Figure 4-60).

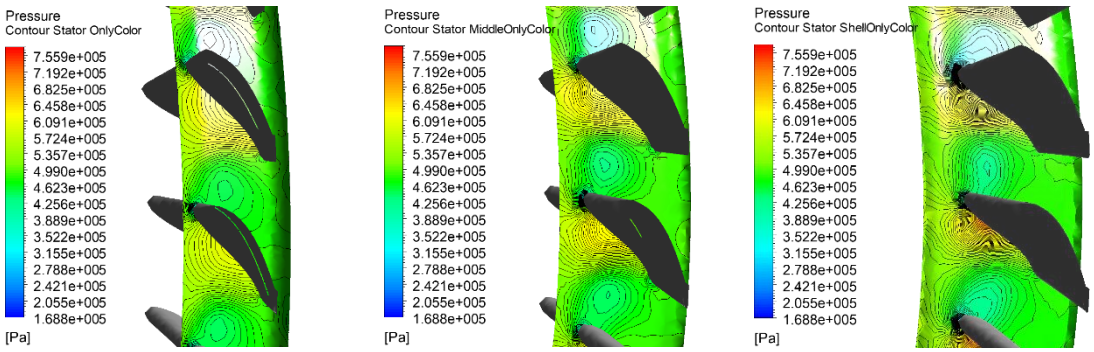

(a) (b) (c)

Figure 4-60. Stator pressure contour for the streamlines at the core (a) middle (b) and shell (c) at SR=0.08.

The high gradient can also be seen at the mid-span between blades where the flow finds its way through the stator (Figure 4-61).

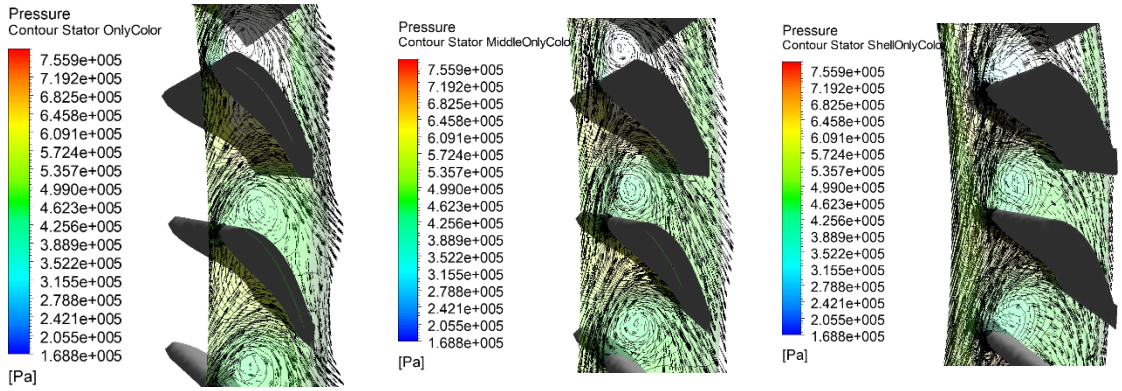

(a) (b) (c)

Figure 4-61. Stator pressure contour with flow vectors for the streamlines at the core (a) middle (b) and shell (c) at SR=0.08.

The circular contour lines seen at SR=0.08 represent the flow recirculation region occurring as a result of the high flow incidence angle at this speed ratio.

This behavior applies to all three speed ratios and it is created by the three-dimensionality of the flow leaving the turbine (vorticity) as it enters into the stator. A view at the middle speed ratio (SR=0.55) show similar findings (Figure 4-62).

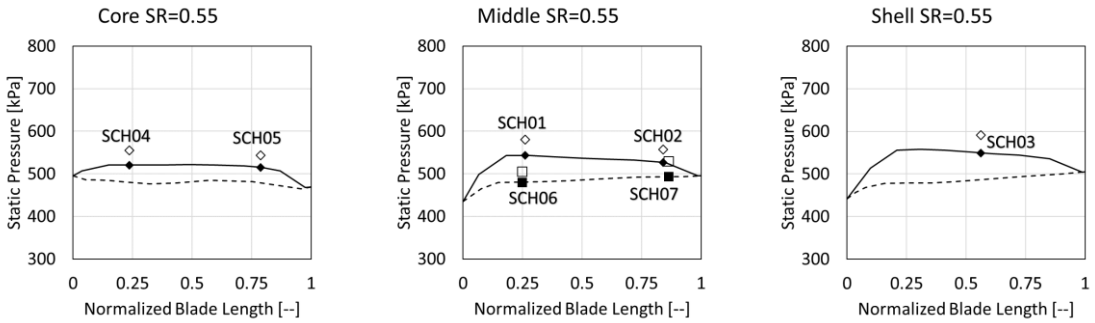

(a) (b) (c)

Figure 4-62. Pressure difference across blade surface for core (a), middle (b) and shell (c) streamline at SR=0.55.

Pressure contours for the SR=0.55 show a more developed flow condition and a reduced recirculation region is observed (Figure 4-63).

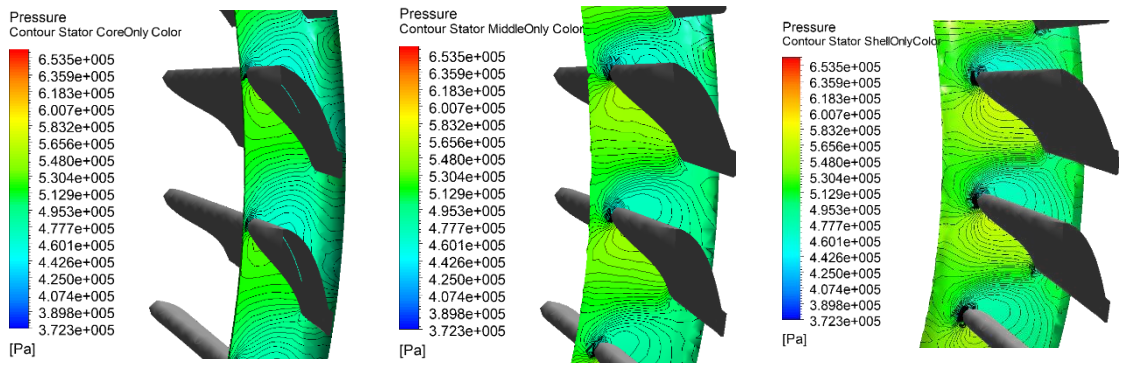

(a) (b) (c)

Figure 4-63. Stator pressure contour for the streamlines at the core (a) middle (b) and shell (c) at SR=0.55.

A look at the vectors at SR=0.55 shows a more even and developed flow through the stator with much increased flow area (Figure 4-64).

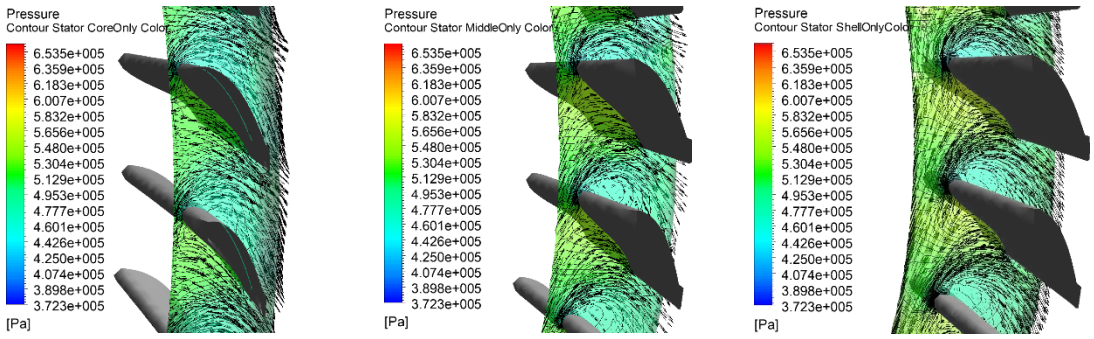

(a) (b) (c)

Figure 4-64. Stator pressure contour with flow vectors for the streamlines at the core (a) middle (b) and shell (c) at SR=0.55.

Finally, at the highest speed ratio (SR=0.90) the size of the inverted region reduces when moving from core to middle and shell (Figure 4-65).

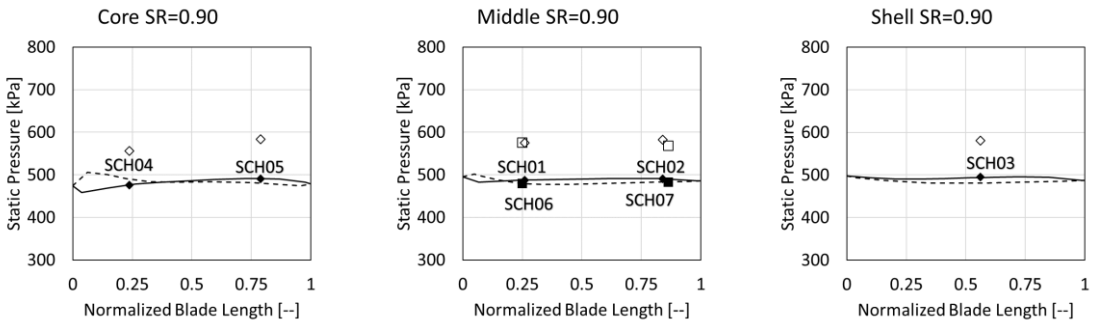

(a) (b) (c)

Figure 4-65. Pressure difference across blade surface for core (a), middle (b) and shell (c) streamline at SR=0.90.

The trends observed and the magnitude of pressure difference across blade side is all the result of the flow incidence angle entering the stator. High incidence closer to the shell and

shallower angles closer to the core. Same applies to the middle and higher speed ratio where the flow impacts the shell streamline in-line with the blade angle, negative incidence angle at the middle streamline and slightly more negative at the core.

Pressure contour plots best show the behavior (Figure 4-66).

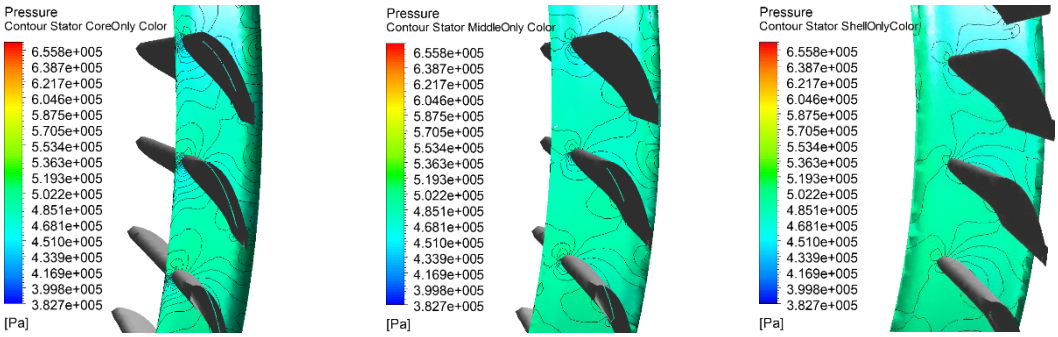

(a) (b) (c)

Figure 4-66. Stator pressure contour for the streamlines at the core (a) middle (b) and shell (c) at SR=0.90.

The vectors confirm the recirculation is no longer present on the suction side (Figure 4-67).

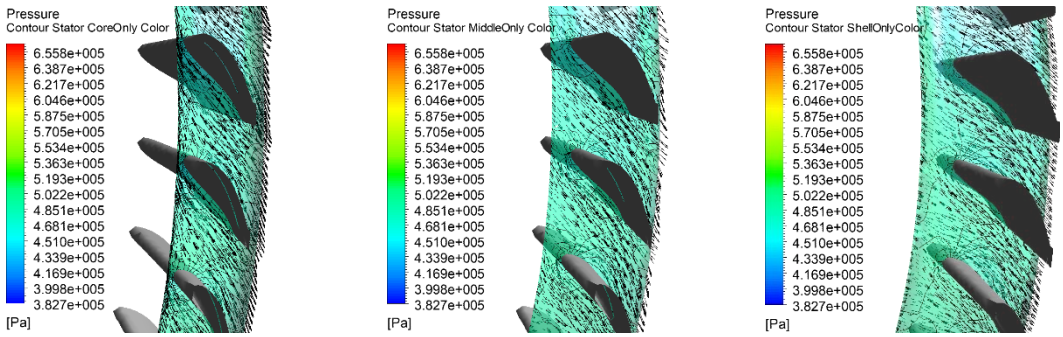

(a) (b) (c)

Figure 4-67. Stator pressure contour with flow vectors for the streamlines at the core (a) middle (b) and shell (c) at SR=0.90.

At the speed ratio SR=0.90, the stator has full area available for flow to go through. No recirculation region occurs at that speed ratio. The flow moves freely without blockage from leading to trailing edge of the blade.

The size of the recirculation region as it moves from core (small) to shell (large) for the low speed ratio can be appreciated better with an iso-surface for a constant pressure. For the middle speed ratio, the recirculation region is uniform and smaller as seen with the iso-surface. For the higher speed ratio, no recirculation is present so an iso-surface is not possible (Figure 4-68).

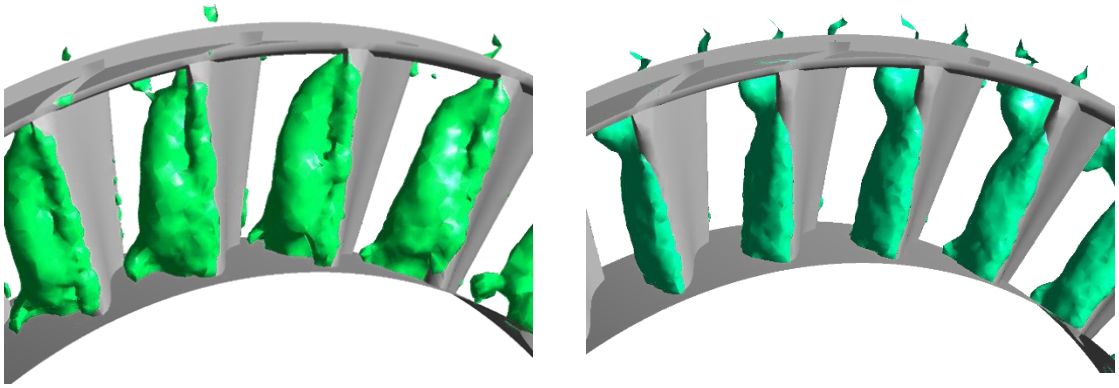

(a) (b)

Figure 4-68. Stator iso-surface for recirculation region at constant 445 kPa pressure at SR=0.08 (a), 485 kPa for SR=0.55 (b).

The reduction in recirculation area is seen thanks to the iso-surface visualization tool. The reduced size occurring at SR=0.55 allows for more flow area through the stator blade channels.

4.6.2 Clutch Cavity Pressure Correlation

TC Cover & Pressure Plate

At the torque converter inlet, higher pressures were found at larger radial locations. This behavior is parabolic in shape, expected and it is due to the centripetal effect added by the spinning converter (Figure 4-69).

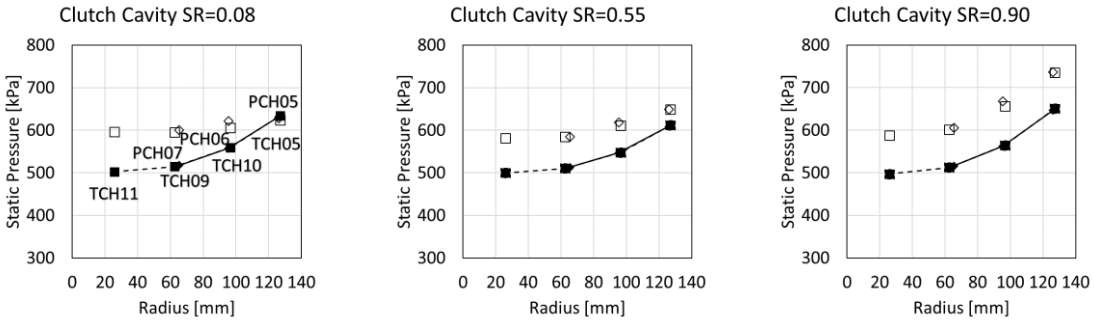

Figure 4-69. Clutch cavity simulated pressure profiles at various speed ratios for the transducers located on the cover (black diamonds) and transducers located on the pressure plate (dashed squares) compared to experimental transducers on cover (white diamonds) and pressure plate (white squares).

Interestingly and somewhat expected, the resultant pressure magnitude is more dependent on radial location than speed of rotation. In other words, when comparing radial locations, both transducers located on the cover or pressure plate have the same pressure magnitude on the CFD as well as on the experimental measurements. The CFD model was able to predict this radial similarity in pressure but not the magnitude or curvature of the parabola seen for the SR=0.08.

Visualization of the pressure contour lines also show a high pressure gradient on the clutch cavity for small radial increments once the flow develops radially once it hits the cover (Figure 4-70).

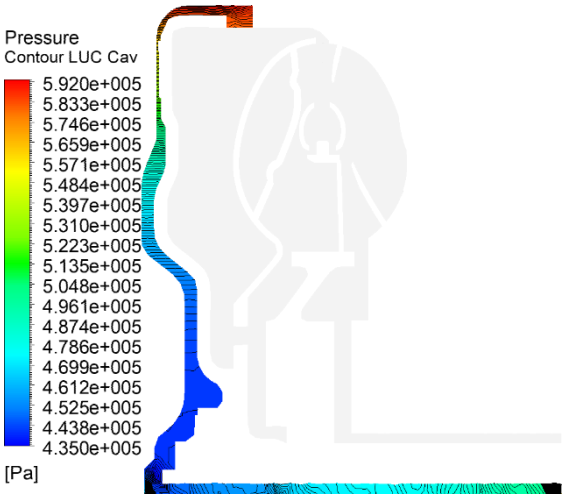

Figure 4-70. Cross sectional pressure contour plot for the clutch cavity at SR=0.08.

For the SR=0.55, conditions in the clutch cavity are similar (Figure 4-71).

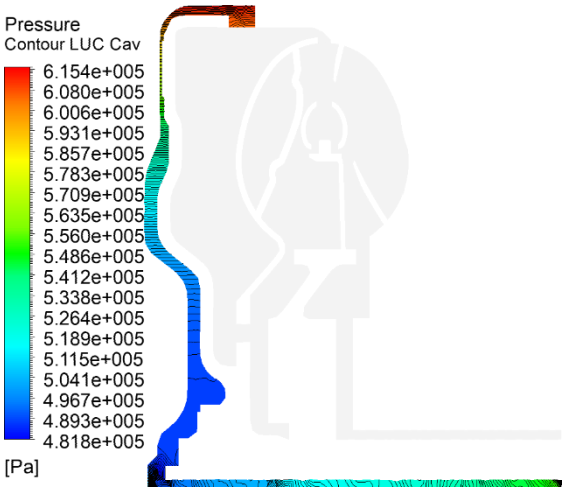

Figure 4-71. Cross sectional pressure contour plot for the clutch cavity at SR=0.55.

Finally, for SR=0.90, repeat (Figure 4-72).

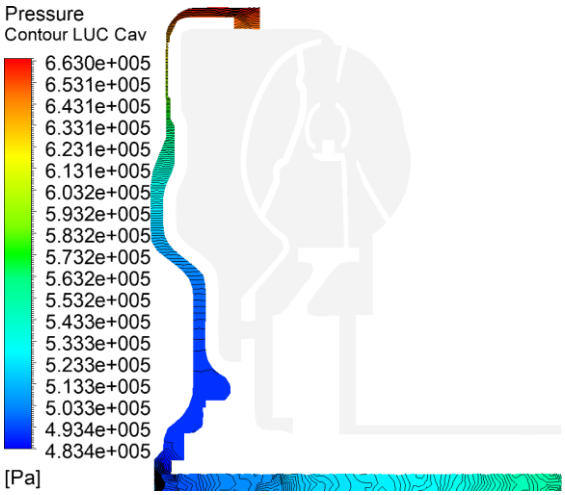

Figure 4-72. Cross sectional pressure contour plot for the clutch cavity at SR=0.90.

The three figures of the clutch cavity demonstrate that flow entering the torque converter is dependent on external conditions external, for similar speeds similar pressures will be seen.

4.6.3 Pressure Plate and Turbine Cavity Correlation

Pressure Plate/Turbine Cavity Flow Visualization

The last of the instrumented cavities to study is between the pressure plate and the turbine shell. This particular cavity had 5 transducers but only 4 monitor points were possible. Adding a monitor point representing TCH07 was not possible due to its location as explained earlier. Radial location was also dominant for this cavity. Transducers located on the same radial location on both surfaces had same pressure magnitude on the experiments as well as in the simulation (Figure 4-73).

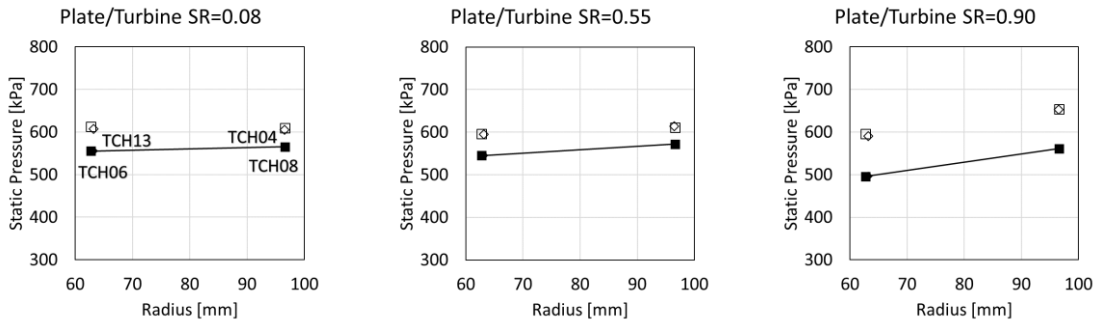

Figure 4-73. Pressure plate/turbine shell cavity simulated pressure profiles at various speed ratios for the transducers located on the turbine shell (black diamonds) and transducers located on the pressure plate (dashed squares) compared to experimental transducers on the turbine shell (white diamonds) and pressure plate (white squares).

Once more, the CFD was able to predict the trends seen with the measurements. For that particular cavity, radial pressures differences at the lowest speed ratio are almost horizontal. This is due to almost having no centripetal effect added to the pressure due to the low turbine speed. Once the turbine gain speeds for the higher speed ratios (SR=0.55 & SR=0.90), radial differences in pressure are visible.

The pressure gradient for this cavity is not as pronounced as the pressure gradients found inside the torus or clutch cavities (Figure 4-74 to Figure 4-76).

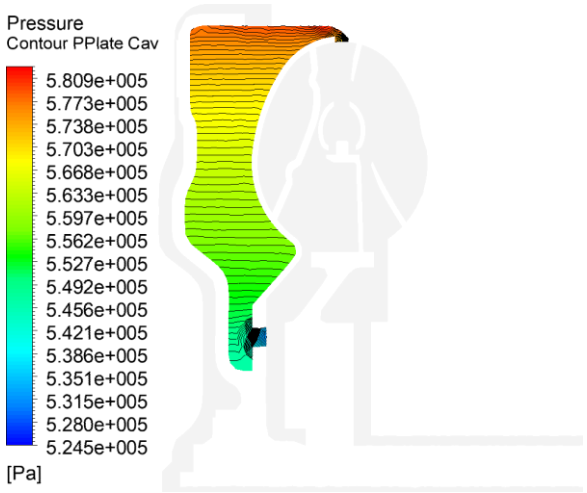

Figure 4-74. Cross sectional pressure contour plot for the cavity between the pressure plate and the turbine at SR=0.08.

For the SR=0.55 conditions are similar (Figure 4-75).

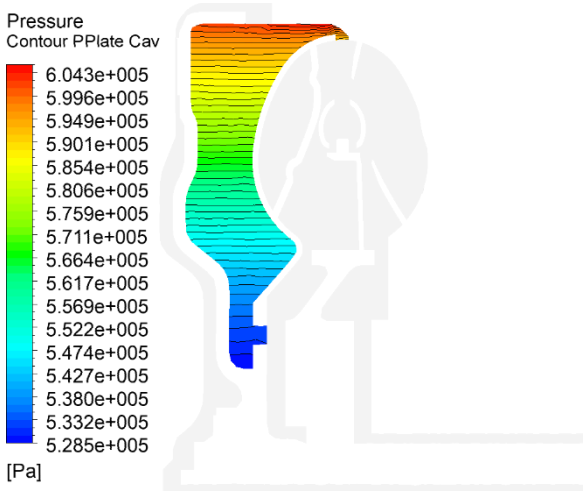

Figure 4-75. Cross sectional pressure contour plot for the cavity between the pressure plate and the turbine at SR=0.55.

Conditions at the inner radius of the cavity changed to some extent but not in a considerable manner when the pressure magnitudes are compared. Similar behavior was seen at SR=0.90 (Figure 4-76).

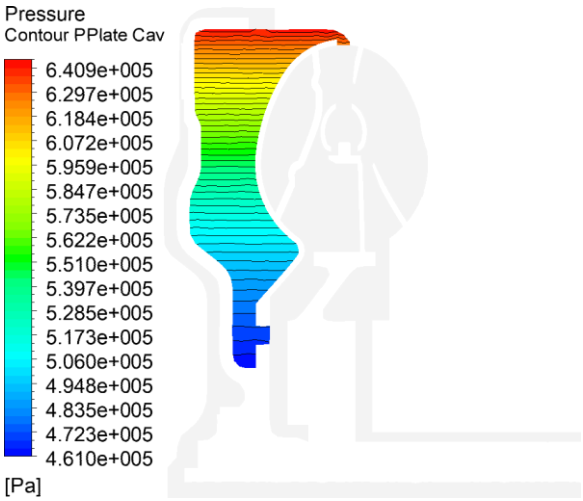

Figure 4-76. Cross sectional pressure contour plot for the cavity between the pressure plate and the turbine at SR=0.90.

The three figures of the pressure plate and turbine shell cavity demonstrate that flow inside that cavity is dependent on conditions external to the torque converter. For similar speeds, similar pressures will be seen.

4.6.4 All Cavities Pressure Contour

A final look for all combined cavities show the pressure gradient difference as the torque converter transitions from low to high speed ratio (Figure 4-77).

(a)

(b)

(c)

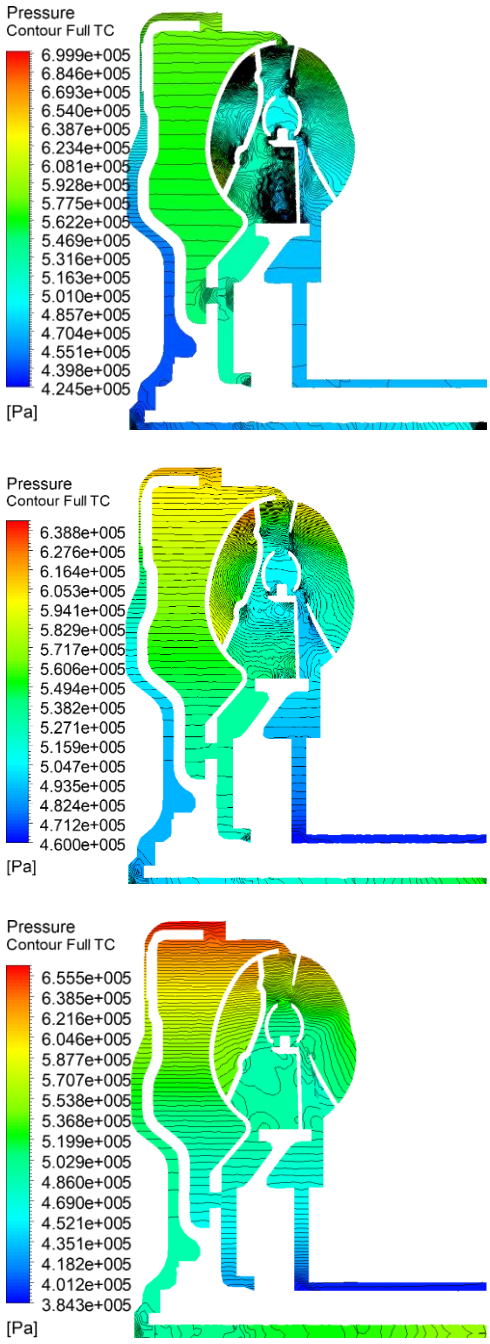

Figure 4-77. Cross sectional pressure contour plot for all converter cavities for SR=0.08 (a), SR=0.55 (b) and SR=0.90 (c).

When looking at the pressure contour, observations about radial similarity per cavity can be seen. Pressure lines are horizontal for the clutch and pressure plate/turbine cavity. Pressure contours inside the torus are chaotic at SR=0.08 and with varied gradient which highlights the ever changing pressure inside the toroidal cavity at this speed ratio. Pressure gradients while increasing speed ratio inside the toroidal cavity reduces, more even pressure gradients are seen at SR=0.55. Once the torque converter operates at high speed ratio (SR=0.90), conditions inside the torus are similar to the rest of the spinning converter. At that speed ratio, all elements are spinning at similar speeds and the flow stabilizes pressures in a radial manner with similar magnitudes.

It has been demonstrated that a properly defined CFD model could be used to study pressures and flow conditions inside the torque converter with a certain degree of accuracy. With future computational advances, the accuracy of the predictions can be improved. As recommended earlier in Chapter 3, subsequent design of experiments could be completed with reducing error in pressure predictions as main objective.

5 Conclusions

Several conclusions and recommendations could be made for the present work. The methods for setting up the simulation model in the commercially available software proved to be very competitive in predicting torques and pressures inside the torque converter when compared to the available test data resulting from the investigations.

5.1 Conclusions to Personal Goals and Lessons Learned

- Proved simulations can more accurately predict torque when compared to results seen in past professional experiences. Error in torque predictions in the present work were in the 6% range for turbine and impeller. The literature review showed errors as high as 49%. Past professional experiences has shown errors as high as 31%.
- Proved simulations can be faster. The present study ran for 300 iterations in under 40 minutes per speed ratio for the full torque converter model. The present method solution times for torque predictions could be reduced to around 13 minutes per speed ratio by reducing the number of iterations even further. Past professional experiences showed a torque converter required months of setup and run time before obtaining results.
- For torque predictions, CFD for torque converters do not need inlet or outlet boundary conditions. Everything can be modeled as enclosed fluids bounded by

walls. Torque calculations rely on pressure differences across blade sides, inlet pressure will only be an offset.

- For the torque converter under study, the available instrumentation useful to the torque converter simulation was TCC Release or any kind of inlet pressure (TCH11) and outlet flow. Outlet pressure instrumentation would have been more advantageous than torque converter outlet flow. The uncontrolled hardware inside the transmission (relief valves, orifices, leak paths) added a level of uncertainty to the problem. Such uncontrolled hardware located before the flow meter like relief valves could be opening to prevent damaging pressures inside the torque converter from occurring resulting in incorrect torque converter through flow assumptions.

5.2 Conclusions for the CFD Simulation Setup Study

- An active or systematic approach of eliminating variables along the way provides a competitive approach at determining variable settings in the commercially available software to model a torque converter.
- For the torque converter under study, errors below 10% were obtained for the torus only model.
- For the full torque converter geometry, errors were further reduced to be below 7%.
- When temperature impact was considered, errors in the torque converter under study were reduced to less than 6% when the inlet temperature ATF properties were used.

- The final CFD model showed a significant solution time reduction to solve 11 speed ratios (from 99 hours to 4.6 hours for the torus only and 6.6 hours for the full converter models).

5.3 Conclusions for the Experiment & CFD correlation

- Stator speed for 75 N-m input impeller torque tests was 300 rpm for SR=0.9.
- Stator speed for 50 N-m input impeller torque tests was 200 rpm for SR=0.9.
- TCC Release, if available, could be used as torque converter inlet pressure.
- Default, modified turbulence intensity as well as multiphase settings did not affect accuracy of the torque predictions.
- Turbulence intensity can be modified as needed to reduce the errors in pressures predictions inside the different cavities of the torque converter.
- Turbulence intensity helped lower errors at the low speed ratios inside the torus.
- Default or multiphase model showed better pressure predictions at the torque converter inlet cavity below the torque converter clutch disc.
- For the mid and high speed ratio ranges, any of the three settings produced similar pressure prediction accuracies.
- Modified turbulence intensity can be used to predict pressures inside the torus cavity or all other cavities with the exception of the torque converter inlet cavity below the clutch disc for the lower speed ratio (SR=0.08).
- The computer model better predicted pressures at the high speed ratio when the experiments were run under low pressure condition.

- The computer model better predicted pressures at the low speed ratio when the experiments were run under high operating pressures.
- No signs of cavitation was observed during the simulations for the tested conditions.
- The operating conditions for all experiments were not affected by cavitation. The highest impeller speed for all experiments at SR=0.08 was 1755 rpm. The required speed for cavitation was shown to be higher than 2000 to 3000 rpm for the same speed ratio.

The study demonstrated that there is never a single recipe to model the conditions inside the torque converter. Areas of interest must be modeled to fit the conditions in those cavities.

The study also showed that higher turbulence inside the torus affected the conditions in the rest of the cavities in its proximity.

6 Recommendations

6.1 CFD model recommendations

- For new designs, the recommended approach would be to use the developed variable combination as a starting point and improve upon it by performing successive DOE's tailored to reducing error and computational time.
- A closer look and possibly a full DOE should be done on the cavities surrounding the torus.
- Consider investing more time into the single blade model CFD to reduce solution time for torque predictions for the torus only model.

6.2 Test recommendations

- It was found that the telemetry system developed for the present work did not give the user the freedom to select the sampling frequency. A recommendation for future projects would be to allow the user to dictate the sampling frequency.
- Previous work demonstrated the ability to acquire up to 8 channels of data simultaneously using telemetry. It is recommended that for research oriented projects, acquiring as many channels as possible simultaneously would open up the possibilities for post processing the data (cross-spectrums, frequency response functions, etc.)
- For future instrumentation, consider adding thermocouples on the three-elements or at least at turbine or stator exit.

- For future transmission instrumentation, it is recommended to locate TCC Release, as close as possible to the torque converter inlet and outlet.
- Understand the type of pressure being measured (absolute vs gage). The CFD model will work with either as long as there is consistency. If TCC release is measuring gage pressure, use gage pressure in the simulations, if is absolute then use absolute. Initial CFD runs were using TCC release as TC inlet in gage and being compared against instrumented absolute pressures. The error was corrected early.

7 Resulting Publications

The titles below were submitted to SAE International Journal of Passenger Cars-Mechanical Systems. At the time of dissertation completion, all the articles were in the editor review stage.

- "Systematic CFD Parameter Approach to Improve Torque Converter Simulation."
- "Torque Converter Conformal Mapping."
- "Torque and Pressure CFD Correlation of a Torque Converter"
- "Torque Converter Simulation for Extreme Operating Conditions"

8 References

1. George F. Wislicenus, “Fluid Mechanics of Turbomachinery”. First edition, 1947, pp. 375
2. Upton, E., “Application of Hydrodynamic Drive Units to Passenger Car Automatic Transmissions.” SAE Technical Paper 610234, 1961, https://doi.org/10.4271/610234.
3. “The Design of a Single-Stage Three-Element Torque Converter.” SAE Technical Paper 610576, 1961, https://doi.org/10.4271/610576.
4. Qualman, J. and Egbert, E., “Fluid Couplings.” SAE Technical Paper 610233, 1961, https://doi.org/10.4271/610233.
5. Walker, F., “Multiturbine Torque Converters.” SAE Technical Paper 610232, 1961, https://doi.org/10.4271/610232.
6. Zarotti, G.L., Nervegna, N. “Hydraulic Torque Converters Design.” 6th Australian Hydraulics and Fluids Mechanics Conference. 5-9 December 1977.
7. A. Whitfield, F.J. Wallace, R. Sivalingam, “A performance prediction procedure for three-element torque converters.” International Journal of Mechanical Sciences, Volume 20, Issue 12, 1978, Pages 801-814, ISSN 0020-7403, https://doi.org/10.1016/0020-7403(78)90006-1.

8. Kotwicki, A., "Dynamic Models for Torque Converter Equipped Vehicles," SAE Technical Paper 820393, 1982, https://doi.org/10.4271/820393.
9. A. Whitfield, F.J. Wallace, A. Patel, "Performance prediction of multi element torque converters." International Journal of Mechanical Sciences, Volume 25, Issue 2, 1983, Pages 77-85, ISSN 0020-7403, https://doi.org/10.1016/0020-7403(83)90001-2.
10. A. Whitfield, F.J. Wallace, A. Patel, "Design of three-element hydrokinetic torque converters." International Journal of Mechanical Sciences, Volume 25, Issue 7, 1983, Pages 485-497, ISSN 0020-7403, https://doi.org/10.1016/0020-7403(83)90041-3.
11. P. J. Strachan, F. P. Reynaud, T. W. von Backström, "The hydrodynamic modeling of torque converters", vol. 8, no. 1, pp. 21-29, 1992.
12. Ma, W., Luo, B., and Wu, S., "The Research on Quasi-Three-Dimensional Flow Design of Hydrodynamic Torque Converter Blades," SAE Technical Paper 912701, 1991. https://doi.org/10.4271/912701.
13. Pritchard, E., Gould, R., and Johnson, R., "A Fluid Model Extension of the Torque Converter into the Overrunning Regime," SAE Technical Paper 2014-01-1752, 2014, https://doi.org/10.4271/2014-01-1752.

14. Aungier RH. "Mean Streamline Aerodynamic Performance Analysis of Centrifugal Compressors." ASME. J. Turbomach. 1995;117(3):360-366. doi:10.1115/1.2835669.
15. Baljé OE. "Axial Cascade Technology and Application to Flow Path Designs. Part I—Axial Cascade Technology." ASME. J. Eng. Power. 1968;90(4):309-328. doi:10.1115/1.3609206.
16. M. P. Boyce, "Principles of Operation and Performance Estimation of Centrifugal Compressors", Proceedings of the Twenty-second Turbomachinery Symposium, 1993.
17. Gong, X.; Chen, R. "Total pressure loss mechanism of centrifugal compressors." Mech. Eng. Res. 2014, 4, 45–59.
18. B.K. Gandhi, S.N. Singh, V. Seshadri, "Prediction of performance characteristic of centrifugal pump handling clear liquid," Indian Journal of Engineering and Materials Sciences, 5 (1998), pp. 91-96
19. J. Gülich, "Disk friction losses of closed turbomachine impellers." Forschung im Ingenieurwesen, 68 (2) (2003), pp. 87-95
20. Mohammed Ahmed El-Naggar, "A One-Dimensional Flow Analysis for the Prediction of Centrifugal Pump Performance Characteristics," International Journal of Rotating Machinery, vol. 2013, Article ID 473512, 19 pages, 2013. https://doi.org/10.1155/2013/473512.

21. Rodgers CC. "The Performance of Centrifugal Compressor Channel Diffusers." ASME. Turbo Expo: Power for Land, Sea, and Air, Volume 1: Turbomachinery ():V001T01A003. doi:10.1115/82-GT-10.
22. BING Hao, TAN Lei, CAO Shuliang, et al. "Prediction method of impeller performance and analysis of loss mechanism for mixed-flow pump"[J]. Science China Technology Science, 2012, 55(7): 1 988–1 998.
23. Gandhi , B. K. , S. N. Singh , and V. Seshadri . 2000 . "Improvement in the prediction of performance of centrifugal slurry pump handling slurries." Proceeding of Intuition Indian Journal of Mechanical Engineers A 214 : 473 – 486
24. C. Gu, Y. Song, P. Li. "A new optimization method for centrifugal compressors based on 1D calculations and analyses." Energies, 8 (2015), pp. 4317-4334 no. 10.3390/en8054317
25. Veres JP. "Centrifugal and axial pump design and off-design performance prediction." Tech rep; NASA; Sunnyvale, United States of America. Technical Memorandum 106745; 1994.
26. Japikse, D., "Turbomachinery Performance Modeling," SAE Technical Paper 2009-01-0307, 2009, https://doi.org/10.4271/2009-01-0307.
27. Thompson, W. E., 1972, "Aerodynamics of Turbines," Proceedings of the First Turbomachinery Symposium, Turbomachinery Laboratory, Texas A&M University, College Station, Texas, pp. 90-104

28. H. Javaniyan Jouybari, M. Eftari, M. R. Shahhoseini, F. Ghadak, M. Rad, "A Method of Performance Estimation for Axial Flow Turbines Based on Losses Prediction." Journal of Mechanical Research and Application, Vol. 4, No.1, 2012, 35- 43
29. Haaland SE. "Simple and Explicit Formulas for the Friction Factor in Turbulent Pipe Flow." ASME. J. Fluids Eng. 1983;105(1):89-90. doi:10.1115/1.3240948.
30. Wiesner FJ. "A Review of Slip Factors for Centrifugal Impellers." ASME. J. Eng. Power. 1967;89(4):558-566. doi:10.1115/1.3616734.
31. Dunham JJ, Came PM. "Improvements to the Ainley-Mathieson Method of Turbine Performance Prediction." ASME. J. Eng. Power. 1970;92(3):252-256. doi:10.1115/1.3445349.
32. Tasaka, T., Oshima, N., Fujimoto, S., and Kishi, Y., "Application of Large Eddy Simulation to a Torque Converter to Predict its Fluid Performance", SAE Technical Paper 2017-01-1116, 2017
33. Abe, H., Tsuruoka, M., Muto, A., Kato, M. et al., "Development of Super Ultra Flat Torque Converter with Multi Plate Lock-up Clutch," SAE Int. J. Engines 2(1):48-55, 2009
34. Hachisuwa, I., Kato, N., Kusamoto, D., Miyata, H. et al., "Development of Compact Torque Converter with New Multiple Disk Clutch for Toyota New FWD Eight-Speed Transmission Direct Shift-8AT," SAE Technical Paper 2017-01-1118, 2017

35. Minato, K., Sakamoto, K., Takagi, M., and Fujitani, K., "A Performance Prediction of Hydrodynamic Torque Converter," SAE Technical Paper 900555, 1990
36. Keisuke Tsutsumi, Satoshi Watanabe, Shin-ichi Tsuda and Takeshi Yamaguchi. "Cavitation Simulation of Automotive Torque Converter Using a Homogeneous Cavitation Model". International Symposium on Transport Phenomena and Dynamics of Rotating Machinery Hawaii, Honolulu April 10-15, 2016
37. Cheng Liu, Wei Wei, Qingdong Yan, Brian K. Weaver, Houston G. Wood. "Influence of Stator Blade Geometry on Torque Converter Cavitation". Journal of Fluids Engineering. ASME APRIL 2018, Vol. 140/041102-1
38. J. Schweitzer, J. Gandham. "Computational Fluid Dynamics in Torque Converters: Validation and Application". International Journal of Rotating Machinery, 9: 411–418, 2003
39. S. Jeyakumar, M. Sasikumar. "Computational Fluid Dynamics Simulation of Hydraulic Torque Converter for Performance Characteristics Prediction". International Journal of Scientific Research in Science, Engineering and Technology (IJSRSET). Print ISSN: 2395-1990. 2017
40. C. Liu, A. Untaroiu, H. G. Wood, Q.D. Yan and W. Wei. "Parametric Analysis and Optimization of Inlet Deflection Angle in Torque Converter", ASME J. Fluid Eng., Vol. 137, pp. 031101, 2015
41. Marcin Migus, Andrzej Kęsy, Zbigniew Kęsy. "Flow simulation in hydrodynamic torque converter". TECHNICAL TRANSACTIONS 7/2017, Mechanics

42. Kathiresan M, Umamageswari A, Subramanian J. “Compatibility and Accuracy of Mesh Generation in HyperMesh and CFD Simulation with Acusolve for Torque Converter” HTC 2012, Valeo publication
43. Cheng Liu, Wei Wei, Qingdong Yan, Brian K. Weaver, “Torque Converter Capacity Improvement Through Cavitation Control by Design”. ASME Journal of Fluids Engineering. April 2017 vol. 139/041103-1
44. J. Ju, J. Jang, M. Choi e, J.H. Baek. "Effects of cavitation on performance of automotive torque converter." Adv. Mech. Eng., 8 (6) (2016), pp. 1-9
45. B. Liu, Q. Yan & W. Wei (2018) “Numerical investigations of the flow induced oscillation of a torque converter” Engineering Applications of Computational Fluid Mechanics, 12:1, 270-281, DOI: 10.1080/19942060.2017.1419149
46. WU Guangqiang, YAN Peng. “SYSTEM FOR TORQUE CONVERTER DESIGN AND ANALYSIS BASED ON CAD/CFD INTEGRATED PLATFORM”. CHINESE JOURNAL OF MECHANICAL ENGINEERING Vol. 21,aNo. 4,a2008
47. Shin, S., Chang, H., and Athavale, M., “Numerical Investigation of the Pump Flow in an Automotive Torque Converter,” SAE Technical Paper 1999-01-1056, 1999
48. Shoab Ahmed Talukder. “Investigation of Fluid Flow in a Torque Converter’s Stator Using Computational Fluid Dynamics Methods”. University of Technology, Sydney, Master's Thesis 2014

49. Wang Songlin, Ma Wenxing. "Computational Fluid Dynamics Simulation Optimization Research Based on Hydraulic Torque Converter". Advanced Materials Research. ISSN: 1662-8985, Vol. 859, pp 48-51
50. Watanabe N., Miyamoto S., Kuba M., Nakanishi J. "The CFD Application for Efficient Designing in the Automotive Engineering" 203-01-1335. SAE 2003
51. Wu, G. and Wang, L., "Multi-Objective Optimization Employing Genetic Algorithm for the Torque Converter with Dual-Blade Stator," SAE Technical Paper 2015-01-1119, 2015, https://doi.org/10.4271/2015-01-1119. https://doi.org/10.4271/2015-01-1119
52. Kubo, M. and Ejiri, E., "A Loss Analysis Design Approach to Improving Torque Converter Performance," SAE Technical Paper 981100, 1998, https://doi.org/10.4271/981100.
53. Shin, S., Chang, H., and Joo, I., "Effect of Scroll Angle on Performance of Automotive Torque Converter," SAE Technical Paper 2000-01-1158, 2000, https://doi.org/10.4271/2000-01-1158.
54. Kim, G. and Jang, J., "Effects of Stator Shapes on Hydraulic Performances of an Automotive Torque Converter with a Squashed Torus," SAE Technical Paper 2002-01-0886, 2002, https://doi.org/10.4271/2002-01-0886.

55. Shin, S., Lee, B., Hong, J., and Joo, I., “Performance Improvement Using a Slotted Stator of an Automotive Torque Converter,” SAE Technical Paper 2003-01-0247, 2003, https://doi.org/10.4271/2003-01-0247.
56. Dong, Y., Korivi, V., Attibele, P., and Yuan, Y., “Torque Converter CFD Engineering Part I: Torque Ratio and K Factor Improvement Through Stator Modifications,” SAE Technical Paper 2002-01-0883, 2002, https://doi.org/10.4271/2002-01-0883.
57. Dong, Y., Korivi, V., Attibele, P., and Yuan, Y., “Torque Converter CFD Engineering Part II: Performance Improvement through Core Leakage Flow and Cavitation Control,” SAE Technical Paper 2002-01-0884, 2002, https://doi.org/10.4271/2002-01-0884.
58. Chen, J. and Wu, G., "Numerical Investigation of Jet-Wake and Secondary Flows in a Hydrodynamic Torque Converter," SAE Technical Paper 2017-01-1335, 2017, https://doi.org/10.4271/2017-01-1335.
59. By, R. and Mahoney, J., "Technology Needs for the Automotive Torque Converter—Part 1: Internal Flow, Blade Design, and Performance," SAE Technical

Paper 880482, 1988, https://doi.org/10.4271/880482.

60. J. D. Anderson. “Computational Fluids Dynamics-The Basics With Applications”. McGraw Hill, Inc. 1995 ISBN 0-07-113210-4
61. B.E. Launder and B.I. Sharma, “Application of the Energy Dissipation Model of Turbulence to the Calculation of Flow Near a Spinning Disc,” Letters in Heat and Mass Transfer, Vol. 1, No. 2, pp. 131-138, 1974
62. D.C. Wilcox, 2006, Turbulence Modeling for CFD, 3rd Ed., DCW Industries, Inc
63. P. R. Spalart and S. R. Allmaras, “A one-Equation Turbulence Model for Aerodynamic Flows”, AIAA Paper 92-439,1992
64. Srinivasan, C., Joshi, D., Dhar, S., and Wang, D., “Dynamic Three-Dimensional CFD Simulation of Closed Circuit Torque Converter Systems,” SAE Int. J. Passeng. Cars - Mech. Syst. 9(1):289-300, 2016
65. De Jesus Rivera, E. “Blade Induced Tip Loading on a 310 mm Torque Converter Turbine Blade”. Master’s Thesis 2003. Michigan Technological University.
66. P. O. Sweger, C. L. Anderson, and J. R. Blough, “Measurements of Strain on 310 mm Torque Converter Turbine Blades,” International Journal of Rotating Machinery, vol. 10, no. 1, pp. 55-63, 2004. https://doi.org/10.1155/S1023621X04000065.
67. C. L. Anderson, L. Zeng, P. O. Sweger, A. Narain, and J. R. Blough, “Experimental Investigation of Cavitation Signatures in an Automotive Torque Converter Using a

Microwave Telemetry Technique," International Journal of Rotating Machinery, vol. 9, no. 6, pp. 403-410, 2003. https://doi.org/10.1155/S1023621X03000381

68. Mekkes, J & Anderson, Carl & Narain, Amitabh. (2004). "Static pressure measurements and cavitation signatures on the nose of a torque converters stator blades."
69. By, R. and Lakshminarayana, B., "Static Pressure Measurement in a Torque Converter Stater," SAE Technical Paper 911934, 1991, https://doi.org/10.4271/911934.
70. Zwart, P.J. & Gerber, A.G. & Belamri, Thabet. (2004). A two-phase flow model for predicting cavitation dynamics. Fifth International Conference on Multiphase Flow.
71. C. L. Anderson, L. Zeng, P. O. Sweger, A. Narain, and J. R. Blough, "Experimental Investigation of Cavitation Signatures in an Automotive Torque Converter Using a Microwave Telemetry Technique," International Journal of Rotating Machinery, vol. 9, no. 6, pp. 403-410, 2003. https://doi.org/10.1155/S1023621X03000381.
72. D. L. Robinette, J. M. Schweitzer, D. G. Maddock, C. L. Anderson, J. R. Blough, and M. A. Johnson, "Predicting the Onset of Cavitation in Automotive Torque Converters—Part I: Designs with Geometric Similitude," International Journal of Rotating Machinery, vol. 2008, Article ID 803940, 8 pages, 2008. https://doi.org/10.1155/2008/803940.

73. D. L. Robinette, J. M. Schweitzer, D. G. Maddock, C. L. Anderson, J. R. Blough, and M. A. Johnson, “Predicting the Onset of Cavitation in Automotive Torque Converters—Part II: A Generalized Model,” International Journal of Rotating Machinery, vol. 2008, Article ID 312753, 8 pages, 2008. https://doi.org/10.1155/2008/312753.

74. Robinette, D., Anderson, C., Blough, J., Johnson, M. et al., "Characterizing the Effect of Automotive Torque Converter Design Parameters on the Onset of Cavitation at Stall," SAE Technical Paper 2007-01-2231, 2007, https://doi.org/10.4271/2007-01-2231.

75. Mekkes J, Anderson CL, Narain A. "Static Pressure Measurements on the Nose of a Torque Converter Stator during Cavitation". ISROMAC. 2004

A. Calibration Curves

A.1 Laboratory Channels

Measurement	Channel Name	DAQ Name	Calibration	Units
Flow	Flow Meter	Flow_Meter	1*V	GPM
Speeds	Input Dyno	DC_Tach	V*1000	RPM
	Output Dyno	AC_Tach	V*-968.06+41.423	RPM
Temperature	Transmission Inlet	Inlet_Temp	45*V+50	F
	Transmission Outlet	Outlet_Temp	45*V+50	F
Torques	Input Dyno	DC_Torque	V*1031.8+1.4867	N-m
	Output Dyno	AC_Torque	V*1002.9-1.0299	N-m

A.2 Transmission Channels

Measurement	Channel Name	DAQ Name	Calibration	Units
Pressures	Trans. Inlet	Trans_IN_Pressure	300/10*V	PSIg
	Trans. Outlet	Trans_OUT_Pressure	300/10*V	PSIg
	Line	LINE_Pressure	300/10*(V+6.75)	PSIg
	TCC Release	TCC_REL_Pressure	300/10*V	PSIg

A.3 Torque Converter Telemetry Channels

A.3.1 Impeller

Ford

(February 7, 2018)

Project # FM059A16 Pump Housing/Cover

For: Transmitter Info : Serial no.- uW69616 / 2490 MHZ / 7.78 KHZ marker

Resonance – 157 KHZ / Switch # 0

Power Ranges – Minimum 40 % Maximum 55 %

Run 50 %

F = Transmitter output frequency in Hertz

Psia = Absolute pressure (see individual channels 1 – 7 below)

Channel / location / description	Equation for pressure	Time per channel in seconds
CH1 – Inner edge between blades on Pump Housing Inlet	Psia= 0.008638029869 (F) -99.44729811	1
CH2 – Outer edge of Pump Housing Outlet	Psia= 0.00701135415 (F) -79.74775415	1
CH3 – Outer edge between blades on Pump Housing Outlet	Psia= 0.008402019543 (F) - 96.12261487	1
CH4 – Center between blades on Pump Housing	Psia= 0.008029549258 (F) -91.98737764	1
CH5 – Outer edge of Cover	Psia= 0.007648388847 (F) -87.14570651	1
CH6 – Middle of Cover	Psia= 0.008258841485 (F) -94.56956628	1
CH7 – Inside edge of Cover	Psia= 0.008821327899 (F) -101.4779555	1

A.3.2 Turbine

Ford

(February 7, 2018)

Project # FM059C16 Clutch Turbine

For: Transmitter Info : Serial no.- uW69516 / 2454 MHZ / 7.84 KHZ marker

Resonance – 157 KHZ / Switch # 0

Power Ranges – Minimum 40 % Maximum 55 %

Run 50 %

F = Transmitter output frequency in Hertz

Psia = Absolute pressure (see individual channels 1 – 7 below)

Channel / location / description	Equation for pressure	Time per channel in seconds
CH1 – Between leading and trailing edge of blade center Low Pressure Side - Turbine	Psia=0.007346794905 (F) -92.28070922	1.006
CH2 – Leading edge center of inside blade High Pressure Side - Turbine	Psia=0.007234039004 (F) -87.06009566	1.006
CH3 – Leading edge center of outside blade High Pressure Side - Turbine	Psia=0.007036300816 (F) - 84.7866518	1.006
CH4 – Apex of outer crown, Clutch Side - Turbine	Psia= 0.007244836899 (F) -91.69237732	1.006
CH5 – Outer side of Clutch, Cover Side - Clutch	Psia= 0.007325661553 (F) -87.63183286	1.006
CH6 – Center of Clutch, Turbine Side - Clutch	Psia= 0.007590939249 (F) -98.35683078	1.006
CH7 – Inside edge, Turbine Side - Clutch	Psia= 0.007457372053 (F) -92.11135513	1.006
CH8 – Beneath Friction Pad, Turbine Side - Clutch	Psia= 0.007519240949 (F) -93.84658565	1.006

CH9 – Center of Clutch, Cover Side - Clutch	Psia= 0.007559261663 (F) -91.88024022	1.006
CH10 – Outer 1/3rd of Clutch, Cover Side Inside of Friction Pad - Clutch	Psia= 0.007370986774 (F) -93.80947637	1.006
CH11 – Inner Trough, Cover Side - Clutch	Psia= 0.007040972919 (F) -85.50849749	1.006
CH12 – Trailing edge center of outlet blade, Low Pressure Side - Turbine	Psia= 0.007380784833 (F) -89.26060051	1.006
CH13 – Inner Trough Clutch side of Turbine - Turbine	Psia= 0.00732142123 (F) -95.08754094	1.006
CH14 – Leading edge center of Inlet blade, Low Pressure Side - Turbine	Psia= 0.007592811246 (F) -90.82487025	1.006
CH15 – Between leading and trailing edge, blade center High Pressure Side - Turbine	Psia= 0.007268036939 (F) -90.75353399	1.006

A.3.3 Stator

Ford

(February 6, 2018)

Project # FM059B16 Stator

For: Transmitter Info : Serial no.- uW79117 / 2395 MHZ / 7.75 KHZ marker

Resonance – 157 KHZ / Switch # 0

Power Ranges – Minimum 40 % Maximum 55 %

Run 50 %

F = Transmitter output frequency in Hertz

Psia = Absolute pressure (see individual channels 1 – 7 below)

Channel / location / description	**Equation for pressure**	**Time per channel in seconds**
CH1 – Leading edge Center High Pressure side	Psia=0.007089516222 (F) -76.30642319	1.013
CH2 – Trailing edge Center High Pressure side	Psia=0.007351435983 (F) -78.51902848	1.013
CH3 – Inside edge Center of blade High Pressure side	Psia=0.007069822953 (F) - 75.45980463	1.013
CH4 – Leading edge Outer edge of blade High Pressure side	Psia= 0.007427144028 (F) -77.90982171	1.013
CH5 – Trailing edge Outside edge of blade High Pressure side	Psia= 0.007536033627 (F) -80.87638293	1.013
CH6 – Leading edge Center of blade Low Pressure side	Psia= 0.007565572238 (F) -79.31249569	1.013
CH7 – Trailing edge Center of blade Low Pressure side	Psia= 0.007701636962 (F) -82.41690216	1.013

B. Selected Matlab Codes

This section only contains examples of selected programming methods not full codes. The examples were deemed important for complex programming tasks.

B.1 Working with directories

The command below assigns the working directory path into a variable named "directory"

```
directory=cd;
```

New folder names are created by typing them into a new variable called SR

```
%%Fill the folder names matrix
SR=['dp03'
'dp04'
'dp05'];
```

Example of the current working directory:

```
directory =

H:\PhD Progress\6-CFD Results\3-CH4_CFD_TEST_CORRELATION\0-
FromDOE\Obsolete\1-Default Turbulence Intensity 5 5 5 Ns 300\4-
August82018TelemetryTest\1-FullTC\4-August82018TestsDATA5thGearRun1
```

A "for" loop loops through the "SR" variables containing the new folder names and concatenates the current working directory

```
%%Concatenate to define full directory path
full_directory=strcat(directory,'\',SR(pp,:));
```

Example of the new concatenated working directory:

```
full_directory =

H:\PhD Progress\6-CFD Results\3-CH4_CFD_TEST_CORRELATION\0-

FromDOE\Obsolete\1-Default Turbulence Intensity 5 5 5 Ns 300\4-
```

```
August82018TelemetryTest\1-FullTC\4-August82018TestsDATA5thGearRun1
```

`\dp05`

Change the working directory to the new one.

```
%%Change the working directory
cd(full_directory)
```

B.2 Working with Excel or .csv formats

B.1.1 Opening or choosing the file

%%%

```
%%%%%%%%%%%%Choose template file BELOW%%%%%%%%%%%%
%%%%%%%%%%%%Choose template file BELOW%%%%%%%%%%%%
%%%%%%%%%%%%Choose template file BELOW%%%%%%%%%%%%
choice = questdlg('Choose Filename Template File', ...
'Template File', ...
'Browse','Cancel','Cancel');
% Handle response
switch choice
    case 'Browse'
        selection = 1;
    case 'Cancel'
        selection = 0;
end
if selection==1
    file_template=uigetfile({'*.*'});
else
    return
end
```

%%%

%%The line below assigns numerical values to variable named “Gear”, text to a variable

%%named “data_names” and everything exactly as it is in the file to a variable named

%%“raw”.

`[Gear,data_names,raw]=xlsread(file_template);`%%**Works for excel & .csv files**

%%%

%%The line below loads the individual files with file names stored in "data_names"

load(char(data_names(pp,1)));

%%

B.1.2 Saving or creating a new excel file

%%The lines below are for saving data into excel files.

```
Pressure_names={'Pressure_STREAM'
'Pressure_LOADING'}; %%Create the column names
Suction_names={'Suction_STREAM'
'Suction_LOADING'}; %%Create the column names
```

%%Create a table out of a variable

```
Pressure=array2table(Matrix_Pressure_sorted,'VariableNames',Pressure_na
mes');
Suction=array2table(Matrix_Suction_sorted,'VariableNames',Suction_names
');
```

%%Create the new file name by adding "_Results.xlsx" to the original file name

```
string_location=strfind(file_template,'.');
post_proc_file=strcat(file_template(1:string_location-
1),'_Results.xlsx');
```

%%Finds out if the file already exists and eletes it

```
if exist(post_proc_file)
    delete(post_proc_file)
end
warning('off')
```

%%Create the new file.

```
writetable(Pressure,post_proc_file,'Sheet','Pressure');
writetable(Suction,post_proc_file,'Sheet','Suction');
```

B.3 Working with text or data files

%%Define the text or data file names by typing them or on an excel file as explained

%%before. The example below is for a variable containing all file names to analyze.

```
%%%Set the working directory
file_names=['ptorque-rfile.out';
    'ttorque-rfile.out';
```

```
    'storque-rfile.out';
    'ppressu-rfile.out';
    'tpressu-rfile.out';
    'spressu-rfile.out'];
```

%%Finds out if the file exists and opens it

```
%%Open the working file
fid1=fopen(file_names(qq,:),'r');
```

%%Reading the data stored inside the files

```
%%Read file content
while ~feof(fid1)
      tline = fgets(fid1);
      %%Only gets the line with numbers and create variable
      data=textscan(fid1,'%f %f');
end
```

B.4 Assigning data into a new variable being looped

From time to time variables names need to be indexed. To achieve that, create a "for" loop.

Complete all the calculations using "worker/temporary" variables then stored the data into

new, indexed variable names using the following command.

```
%%Time vector
assignin('base',strcat(stringieton,'_IMP_Time_CH_',num2str(qq)),worker_
time)
%%Pressure vector with dropouts
assignin('base',strcat(stringieton,'_IMP_kPa_CH_',num2str(qq)),worker_k
Pa)
%%Pressure vector without dropouts
assignin('base',strcat(stringieton,'_IMP_kPa_Clean_CH_',num2str(qq)),wo
rker_kPa_clean)
```

The variable "stringieton" is a string containing the initial part of the new variable name. The string contained in the variable "stringieton" is concatenated with the new string "_IMP_Time_CH_" and indexed numerically from "1" to the end of the "for" loop.

The result of the above time vector commands is a new variable named:

`test004_CN003_IMP_Time_CH_1`

"stringieton" content: `test004_CN003`
New string added: `_IMP_Time_CH_`

Numerical index added at the end: `1`

A new variable array containing all the names of the newly created variable names can be used for later post processing and assigning content to new "worker/temporary" variables.

```
stringieton_Time_IMP{qq,pp}=strcat(stringieton,'_IMP_Time_CH_',num2str(
qq));

stringieton_kPa_Clean_IMP{qq,pp}=strcat(stringieton,'_IMP_kPa_Clean_CH_
',num2str(qq));
```

The variables created are sized {qq,pp} and contains all variables.

B.5 Evaluating data coming from previous calculations

The purpose is to assign data from previously calculated process to be re-used on a new step in the analysis. A "for" loop was used to store the data into indexed variables as explained earlier. Now the stored data is assigned into new "worker" variables also with the use of a "for" loop.

```
%%Assign data into working variables
worker_time=0;
worker_time=eval(stringieton_Time_IMP{pp,1});
worker_kPa=0;
worker_kPa=eval(stringieton_kPa_Clean_IMP{pp,1});
```

The example assigns the data from the first column {pp,**1**} only. The other columns are used similarly for other applications if needed.

C. Selected Test Stand Design Drawings

C.1 Base Plate Assembly

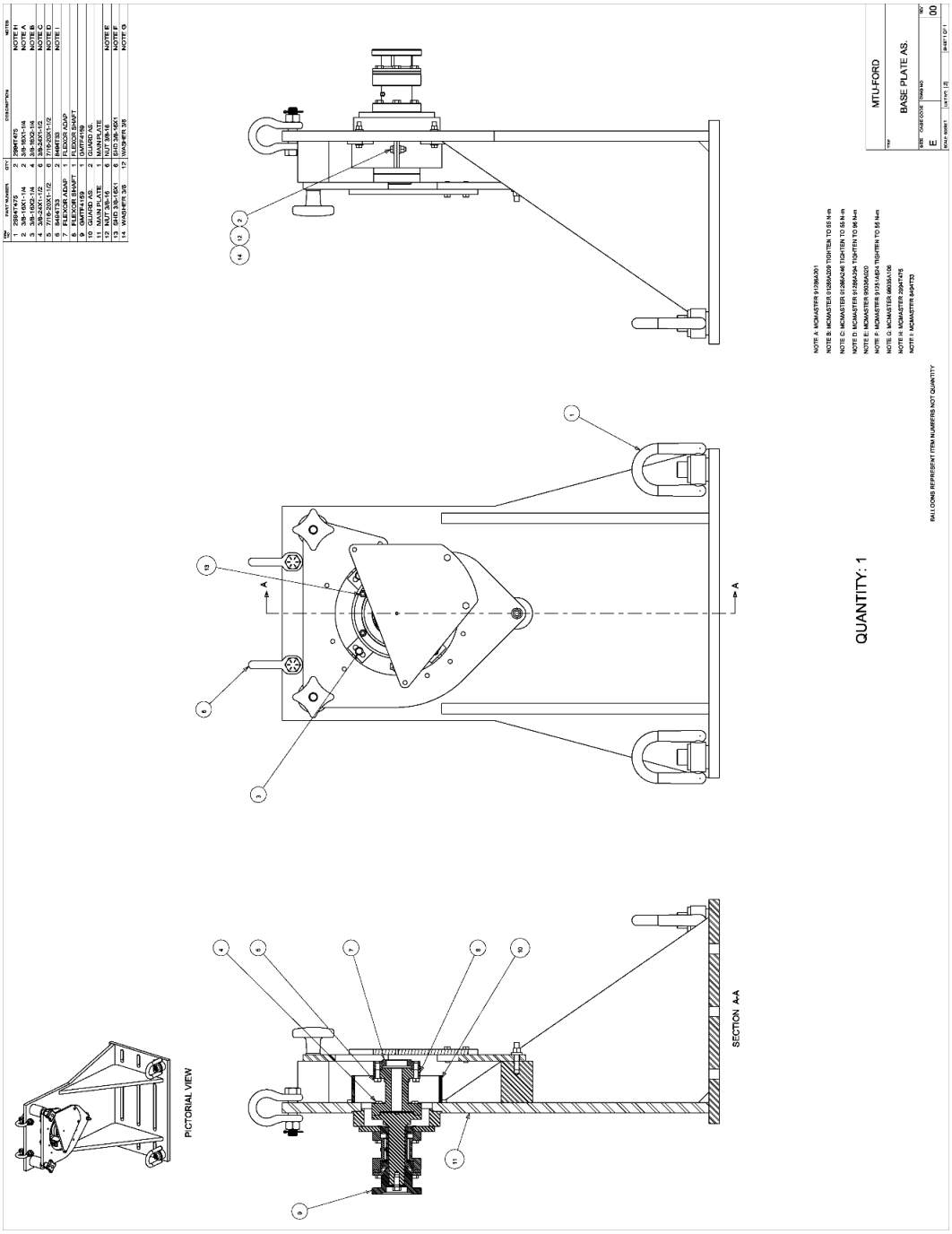

C.2 Bearing Shafting

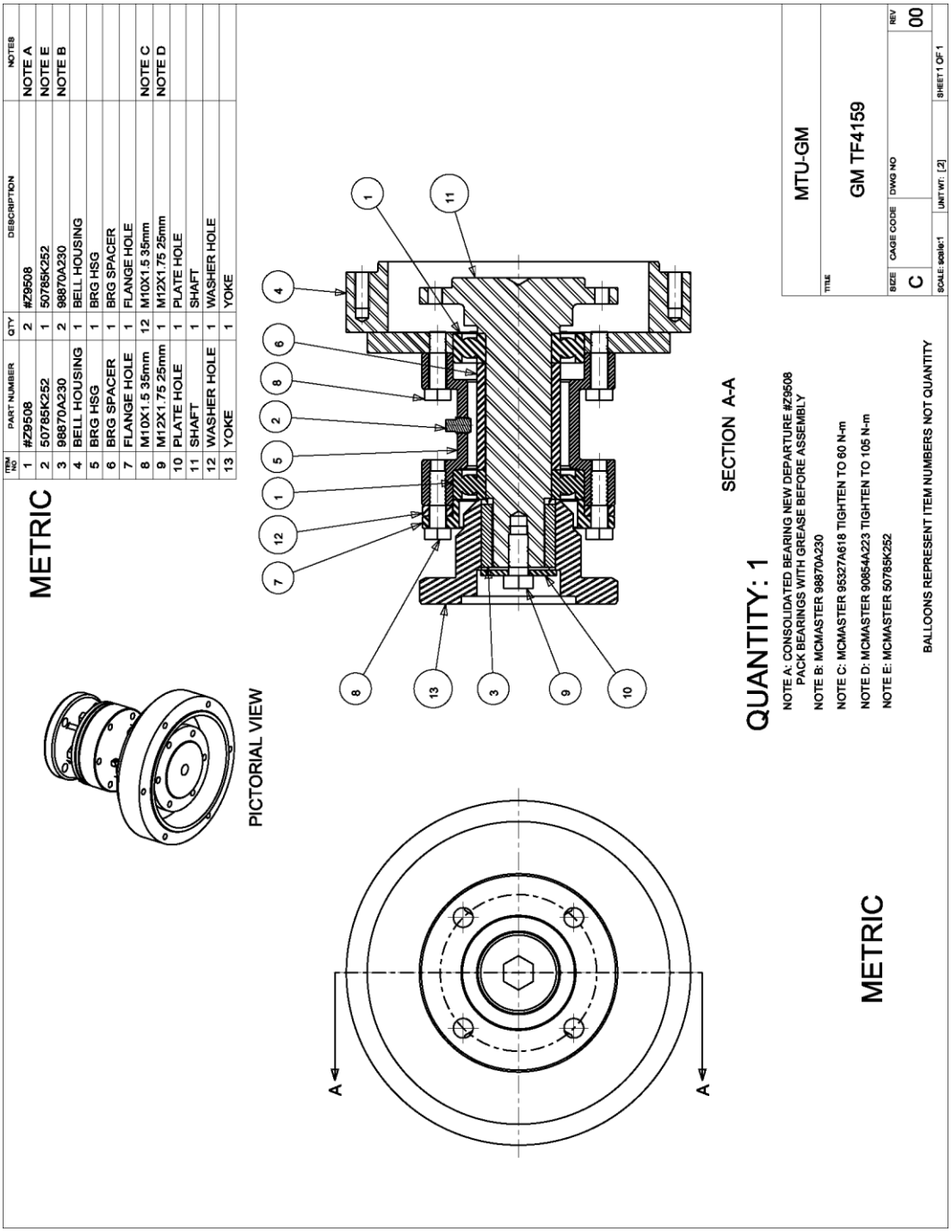

D. CFD Monitor Points Location

CS: Clutch Side

LG: Large

SM: Small

TS: Turbine Side

X direction: Axial

Y direction: Up and down

Z direction: Side to side

D.1 Impeller & Cover Transmitter Monitor Points

Impeller Channel

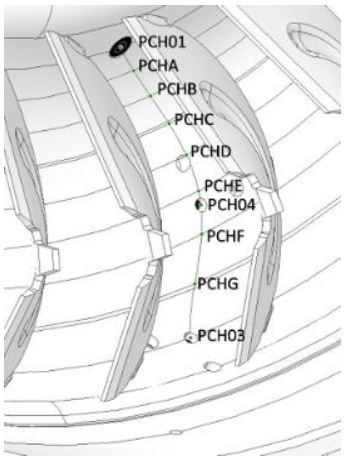

Impeller-Turbine OD

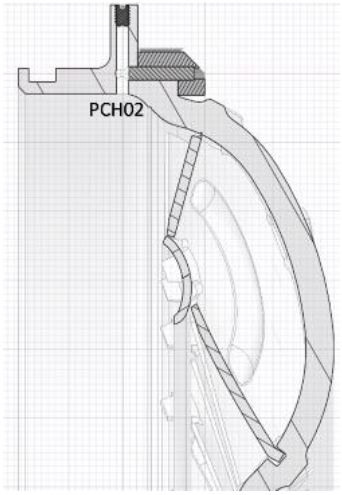

Clutch Cavity

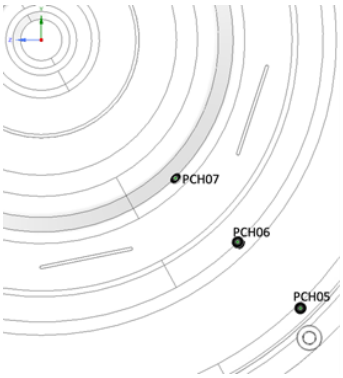

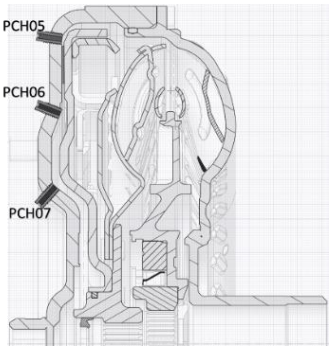

Impeller CFD model monitor points coordinates.

				CFD Location (m)		
Monitor	**Element**	**Location**	**Stream**	**X**	**Y**	**Z**
PCH01	Impeller Channel	Inlet	Shell	0.0734	-0.0750	0.0196
PCH0A	Impeller Channel	Additional	Shell	0.0758	-0.0789	0.0246
PCH0B	Impeller Channel	Additional	Shell	0.0768	-0.0829	0.0291
PCH0C	Impeller Channel	Additional	Shell	0.0768	-0.0871	0.0331
PCH0D	Impeller Channel	Additional	Shell	0.0759	-0.0916	0.0361
PCH0E	Impeller Channel	Additional	Shell	0.0745	-0.0964	0.0379
PCH04	Impeller Channel	Middle	Shell	0.0738	-0.0984	0.0380
PCH0F	Impeller Channel	Additional	Shell	0.0723	-0.1024	0.0374
PCH0G	Impeller Channel	Additional	Shell	0.0694	-0.1089	0.0345
PCH03	Impeller Channel	Exit	Shell	0.0645	-0.1156	0.0305
PCH02	Impeller Channel	OD	Shell	0.0500	0.0636	-0.1100
PCH05	Cover	Large R	--	0.0087	-0.0908	-0.0875
PCH06	Cover	Mid R	--	0.0081	-0.0684	-0.0665
PCH07	Cover	Small R	--	0.0060	-0.0470	-0.0455

Impeller true instrumentation location.

		True Sensor Location (m)		
IRT Nom.	**Element**	**X**	**Y**	**Z**
PCH01	Impeller Channel	0.0734	-0.0747	0.0196
PCH02	Impeller Channel	0.0510	0.0651	-0.1127
PCH03	Impeller Channel	0.0650	-0.1174	0.0301
PCH04	Impeller Channel	0.0761	-0.0984	0.0386
PCH05	Cover	0.0087	-0.0908	-0.0878
PCH06	Cover	0.0081	-0.0684	-0.0665
PCH07	Cover	0.0060	-0.0468	-0.0455

D.2 Turbine Transmitter Monitor Points

Pressure plate (P.Plate) instrumentation

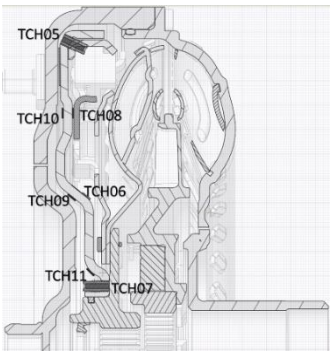

Turbine shell instrumentation

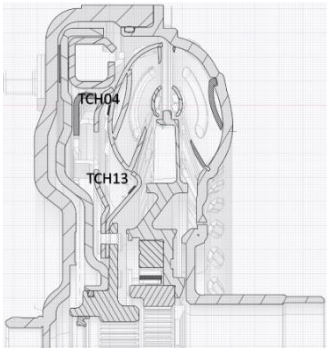

Blade pressure side instrumentation

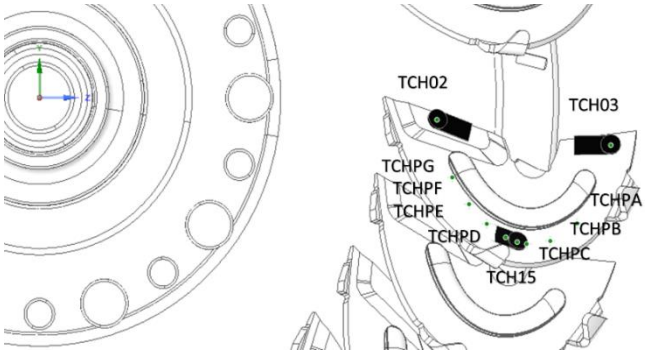

Blade suction side instrumentation.

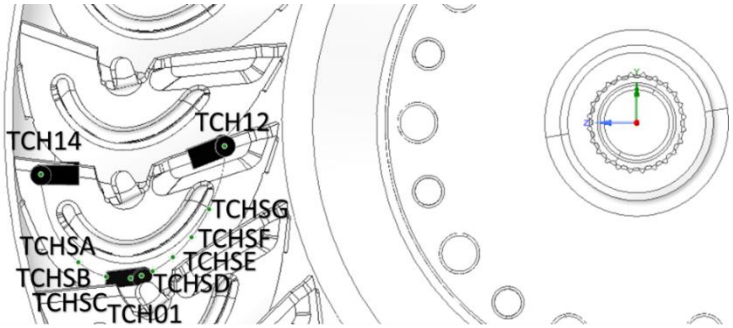

Turbine CFD model monitor points coordinates.

					CFD Location (m)		
Monitor	**Element**	**Location**	**Edge**	**Stream**	**X**	**Y**	**Z**
TCH01	Turbine	SSIDE	Mid	Mid/Shell	0.0373	-0.0297	0.0975
TCH02	Turbine	PSIDE	Trail	Mid	0.0420	-0.0044	0.0815
TCH03	Turbine	PSIDE	Lead	Mid	0.0497	-0.0094	0.1172
TCH04	Turbine	SHELL LG R	N/A	N/A	0.0300	-0.0268	0.0927
TCH05	P. Plate	CS above disc	N/A	N/A	0.0106	0.1239	0.0283
TCH06	P. Plate	TS mid R	N/A	N/A	0.0200	0.0612	0.0139
TCH07	P. Plate	TS small R	N/A	N/A	--	--	--
TCH08	P. Plate	TS large R	N/A	N/A	0.0146	0.0942	0.0215
TCH09	P. Plate	CS Next R	N/A	N/A	0.0145	0.0609	0.0139
TCH10	P. Plate	CS below disc	N/A	N/A	0.0110	0.0942	0.0215
TCH11	P. Plate	CS Small R	N/A	N/A	0.0265	0.0252	0.0058
TCH12	Turbine	SSIDE	Trail	Mid	0.0434	-0.0045	0.0811
TCH13	Turbine	SHELL SM R	N/A	N/A	0.0395	-0.0175	0.0607
TCH14	Turbine	SSIDE	Lead	Mid	0.0513	-0.0100	0.1173
TCH15	Turbine	PSIDE	Mid	Mid/Shell	0.0361	-0.0287	0.0980

Additional CFD monitor points added to the pressure side of the blade.

			CFD Location (m)		
Monitor	**Element**	**Location**	**X**	**Y**	**Z**
TCH03	Turbine	PSIDE	0.0497	-0.0094	0.1172
TCHPA	Turbine	PSIDE	0.0417	-0.0249	0.1103
TCHPB	Turbine	PSIDE	0.0385	-0.0284	0.1048
TCHPC	Turbine	PSIDE	0.0366	-0.0290	0.0999
TCH15	Turbine	PSIDE	0.0361	-0.0287	0.0980
TCHPD	Turbine	PSIDE	0.0357	-0.0277	0.0956
TCHPE	Turbine	PSIDE	0.0355	-0.0251	0.0917
TCHPF	Turbine	PSIDE	0.0361	-0.0212	0.0881
TCHPG	Turbine	PSIDE	0.0378	-0.0158	0.0847
TCH02	Turbine	PSIDE	0.0420	-0.0044	0.0815

Additional CFD monitor points added to the suction side of the blade.

			CFD Location (m)		
Monitor	**Element**	**Location**	**X**	**Y**	**Z**
TCH14	Turbine	SSIDE	0.0513	-0.0100	0.1173
TCHSA	Turbine	SSIDE	0.0422	-0.0272	0.1099
TCHSB	Turbine	SSIDE	0.0395	-0.0298	0.1044
TCHSC	Turbine	SSIDE	0.0378	-0.0302	0.0996
TCH01	Turbine	SSIDE	0.0373	-0.0297	0.0975
TCHSD	Turbine	SSIDE	0.0369	-0.0288	0.0952
TCHSE	Turbine	SSIDE	0.0367	-0.0262	0.0913
TCHSF	Turbine	SSIDE	0.0373	-0.0223	0.0876
TCHSG	Turbine	SSIDE	0.0390	-0.0168	0.0842
TCH12	Turbine	SSIDE	0.0434	-0.0045	0.0811

Turbine true instrumentation location..

					True Sensor Location (m)		
IRT. Nom	**Element**	**Location**	**Edge**	**Stream**	**X**	**Y**	**Z**
TCH01	Turbine	SSIDE	Mid	Mid/Shell	0.0373	-0.0296	0.0975
TCH02	Turbine	PSIDE	Trail	Mid	0.0420	-0.0044	0.0815
TCH03	Turbine	PSIDE	Lead	Mid	0.0497	-0.0094	0.1172
TCH04	Turbine	SHELL LG R	N/A	N/A	0.0300	-0.0268	0.0927
TCH05	P. Plate	CS above disc	N/A	N/A	0.0106	0.1238	0.0283
TCH06	P. Plate	TS mid R	N/A	N/A	0.0200	0.0609	0.0139
TCH07	P. Plate	TS small R	N/A	N/A	0.0297	0.0252	0.0058
TCH08	P. Plate	TS large R	N/A	N/A	0.0146	0.0942	0.0215
TCH09	P. Plate	CS Next R	N/A	N/A	0.0146	0.0609	0.0139
TCH10	P. Plate	CS below disc	N/A	N/A	0.0110	0.0942	0.0215
TCH11	P. Plate	CS Small R	N/A	N/A	0.0266	0.0252	0.0058
TCH12	Turbine	SSIDE	Trail	Mid	0.0434	-0.0045	0.0811
TCH13	Turbine	SHELL SM R	N/A	N/A	0.0395	-0.0175	0.0607
TCH14	Turbine	SSIDE	Lead	Mid	0.0512	-0.0100	0.1173
TCH15	Turbine	PSIDE	Mid	Mid/Shell	0.0361	-0.0287	0.0980

D.3 Stator Transmitter Monitor Points

Core: Pressure side.

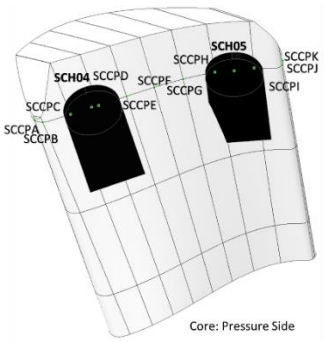

Core: Suction side.

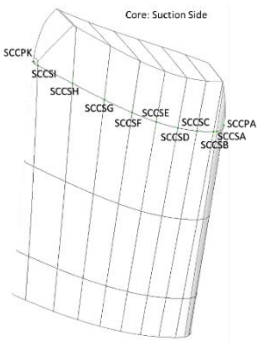

Middle: Pressure side.

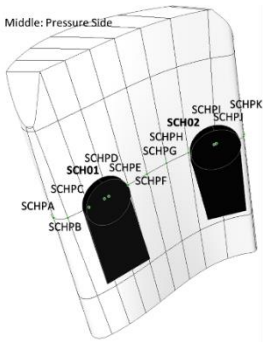

Middle: Suction side.

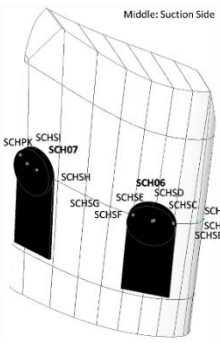

Shell: Pressure side.

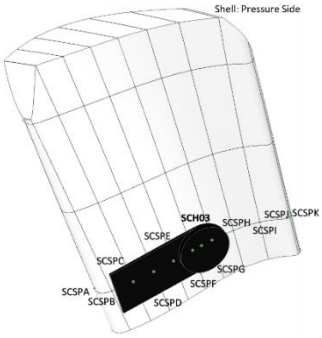

Shell: Suction side.

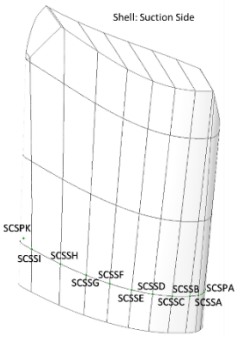

Stator CFD monitor points coordinates. Core pressure side

					CFD Location (m)		
Monitor	**Element**	**Location**	**Edge**	**Stream**	**X**	**Y**	**Z**
SCCPA	Stator	PSide	--	Core	0.0485	0.0612	0.0623
SCCPB	Stator	PSide	--	Core	0.0485	0.0607	0.0628
SCCPC	Stator	PSide	--	Core	0.0498	0.0595	0.0639
SCH04	Stator	PSide	Lead	Core	0.0508	0.0588	0.0650
SCCPD	Stator	PSide	--	Core	0.0511	0.0584	0.0649
SCCPE	Stator	PSide	--	Core	0.0525	0.0573	0.0659
SCCPF	Stator	PSide	--	Core	0.0540	0.0562	0.0669
SCCPG	Stator	PSide	--	Core	0.0553	0.0550	0.0679
SCCPH	Stator	PSide	--	Core	0.0567	0.0535	0.0690
SCH05	Stator	PSide	Trail	Core	0.0574	0.0526	0.0696
SCCPI	Stator	PSide	--	Core	0.0581	0.0516	0.0705
SCCPJ	Stator	PSide	--	Core	0.0591	0.0502	0.0715
SCCPK	Stator	PSide	--	Core	0.0595	0.0504	0.0714

Stator CFD monitor points coordinates. Core suction side.

					CFD Location (m)		
Monitor	**Element**	**Location**	**Edge**	**Stream**	**X**	**Y**	**Z**
SCCPA	Stator	PSide	--	Core	0.0485	0.0612	0.0623
SCCSA	Stator	SSide	--	Core	0.0495	0.0617	0.0618
SCCSB	Stator	SSide	--	Core	0.0498	0.0617	0.0619
SCCSC	Stator	SSide	--	Core	0.0511	0.0615	0.0622
SCCSD	Stator	SSide	--	Core	0.0525	0.0609	0.0627
SCCSE	Stator	SSide	--	Core	0.0540	0.0599	0.0636
SCCSF	Stator	SSide	--	Core	0.0553	0.0586	0.0648
SCCSG	Stator	SSide	--	Core	0.0567	0.0567	0.0665
SCCSH	Stator	SSide	--	Core	0.0581	0.0542	0.0686
SCCSI	Stator	SSide	--	Core	0.0595	0.0511	0.0709
SCCPK	Stator	PSide	--	Core	0.0595	0.0504	0.0714

Stator CFD monitor points coordinates. Middle pressure side.

					CFD Location (m)		
Monitor	**Element**	**Location**	**Edge**	**Stream**	**X**	**Y**	**Z**
SCHPA	Stator	PSide	--	Mid	0.0485	0.0663	0.0416
SCHPB	Stator	PSide	--	Mid	0.0485	0.0657	0.0426
SCHPC	Stator	PSide	--	Mid	0.0498	0.0648	0.0438
SCH01	Stator	PSide	Lead	Mid	0.0508	0.0643	0.0446
SCHPD	Stator	PSide	--	Mid	0.0511	0.0642	0.0449
SCHPE	Stator	PSide	--	Mid	0.0525	0.0634	0.0458
SCHPF	Stator	PSide	--	Mid	0.0540	0.0626	0.0468
SCHPG	Stator	PSide	--	Mid	0.0553	0.0620	0.0478
SCHPH	Stator	PSide	--	Mid	0.0567	0.0611	0.0489
SCH02	Stator	PSide	Trail	Mid	0.0579	0.0600	0.0502
SCHPI	Stator	PSide	--	Mid	0.0581	0.0599	0.0504
SCHPJ	Stator	PSide	--	Mid	0.0593	0.0587	0.0518
SCHPK	Stator	PSide	--	Mid	0.0595	0.0587	0.0518

Stator CFD monitor points coordinates. Middle suction side.

					CFD Location (m)		
Monitor	**Element**	**Location**	**Edge**	**Stream**	**X**	**Y**	**Z**
SCHPA	Stator	PSide	--	Mid	0.0485	0.0663	0.0416
SCHSA	Stator	SSIDE	--	Mid	0.0493	0.0666	0.0413
SCHSB	Stator	SSIDE	--	Mid	0.0498	0.0665	0.0413
SCHSC	Stator	SSIDE	--	Mid	0.0511	0.0663	0.0417
SCHSD	Stator	SSIDE	--	Mid	0.0525	0.0659	0.0423
SCH06	Stator	SSIDE	Lead	Mid	0.0527	0.0657	0.0423
SCHSE	Stator	SSIDE	--	Mid	0.0540	0.0653	0.0433
SCHSF	Stator	SSIDE	--	Mid	0.0553	0.0645	0.0445
SCHSG	Stator	SSIDE	--	Mid	0.0567	0.0634	0.0462
SCHSH	Stator	SSIDE	--	Mid	0.0581	0.0618	0.0482
SCH07	Stator	SSIDE	Trail	Mid	0.0591	0.0603	0.0499
SCHSI	Stator	SSIDE	--	Mid	0.0595	0.0597	0.0507
SCHPK	Stator	PSide	--	Mid	0.0595	0.0587	0.0518

Stator CFD monitor points coordinates. Shell pressure side

					CFD Location (m)		
Monitor	**Element**	**Location**	**Edge**	**Stream**	**X**	**Y**	**Z**
SCSPA	Stator	PSide	--	Shell	0.0485	0.0492	0.0499
SCSPB	Stator	PSide	--	Shell	0.0485	0.0481	0.0510
SCSPC	Stator	PSide	--	Shell	0.0498	0.0471	0.0519
SCSPD	Stator	PSide	--	Shell	0.0511	0.0464	0.0526
SCSPE	Stator	PSide	--	Shell	0.0525	0.0456	0.0532
SCSPF	Stator	PSide	--	Shell	0.0540	0.0449	0.0538
SCH03	Stator	PSide	Mid	Shell	0.0546	0.0446	0.0541
SCSPG	Stator	PSide	--	Shell	0.0553	0.0442	0.0544
SCSPH	Stator	PSide	--	Shell	0.0567	0.0433	0.0551
SCSPI	Stator	PSide	--	Shell	0.0581	0.0421	0.0561
SCSPJ	Stator	PSide	--	Shell	0.0593	0.0405	0.0572
SCSPK	Stator	PSide	--	Shell	0.0595	0.0405	0.0572

Stator CFD monitor points coordinates. Shell suction side.

					CFD Location (m)		
Monitor	**Element**	**Location**	**Edge**	**Stream**	**X**	**Y**	**Z**
SCSPA	Stator	PSide	--	Shell	0.0485	0.0492	0.0499
SCSSA	Stator	SSide	--	Shell	0.0491	0.0494	0.0498
SCSSB	Stator	SSide	--	Shell	0.0498	0.0493	0.0499
SCSSC	Stator	SSide	--	Shell	0.0511	0.0491	0.0502
SCSSD	Stator	SSide	--	Shell	0.0525	0.0485	0.0506
SCSSE	Stator	SSide	--	Shell	0.0540	0.0478	0.0513
SCSSF	Stator	SSide	--	Shell	0.0553	0.0468	0.0522
SCSSG	Stator	SSide	--	Shell	0.0567	0.0457	0.0532
SCSSH	Stator	SSide	--	Shell	0.0581	0.0441	0.0546
SCSSI	Stator	SSide	--	Shell	0.0595	0.0419	0.0562
SCSPK	Stator	PSide	--	Shell	0.0595	0.0405	0.0572

Stator true instrumentation location.

					True Sensor Location (m)		
IRT Nom.	**Element**	**Location**	**Edge**	**Stream**	**X**	**Y**	**Z**
SCH01	Stator	PSide	Lead	Mid	0.0508	0.0643	0.0446
SCH02	Stator	PSide	Trail	Mid	0.0580	0.0600	0.0502
SCH03	Stator	PSide	Mid	Shell	0.0546	0.0446	0.0541
SCH04	Stator	PSide	Lead	Core	0.0508	0.0588	0.0647
SCH05	Stator	PSide	Trail	Core	0.0574	0.0526	0.0696
SCH06	Stator	SSIDE	Lead	Mid	0.0527	0.0657	0.0423
SCH07	Stator	SSIDE	Trail	Mid	0.0591	0.0603	0.0499

E. Cavities, Walls, Interfaces and Boundaries Nomenclature

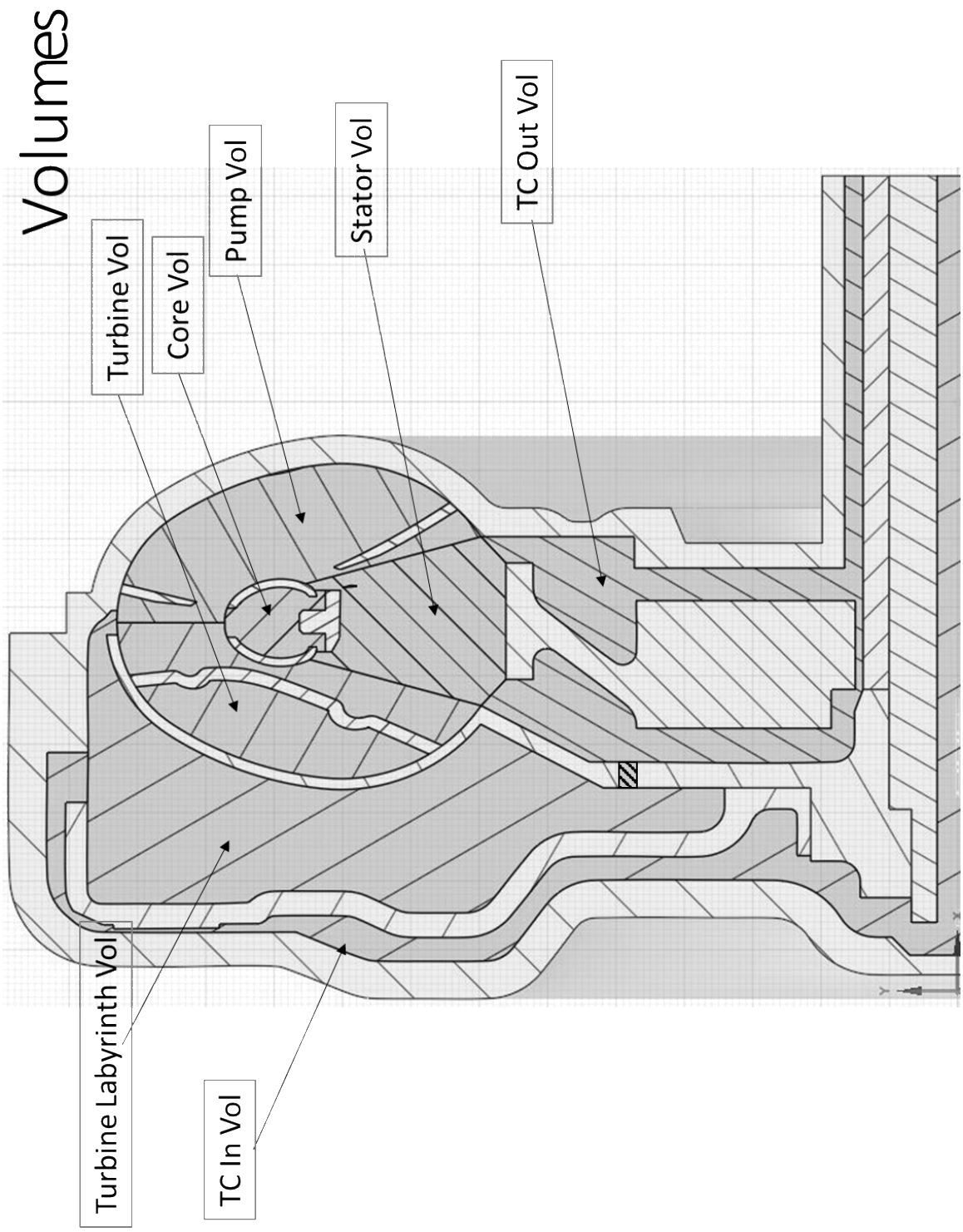

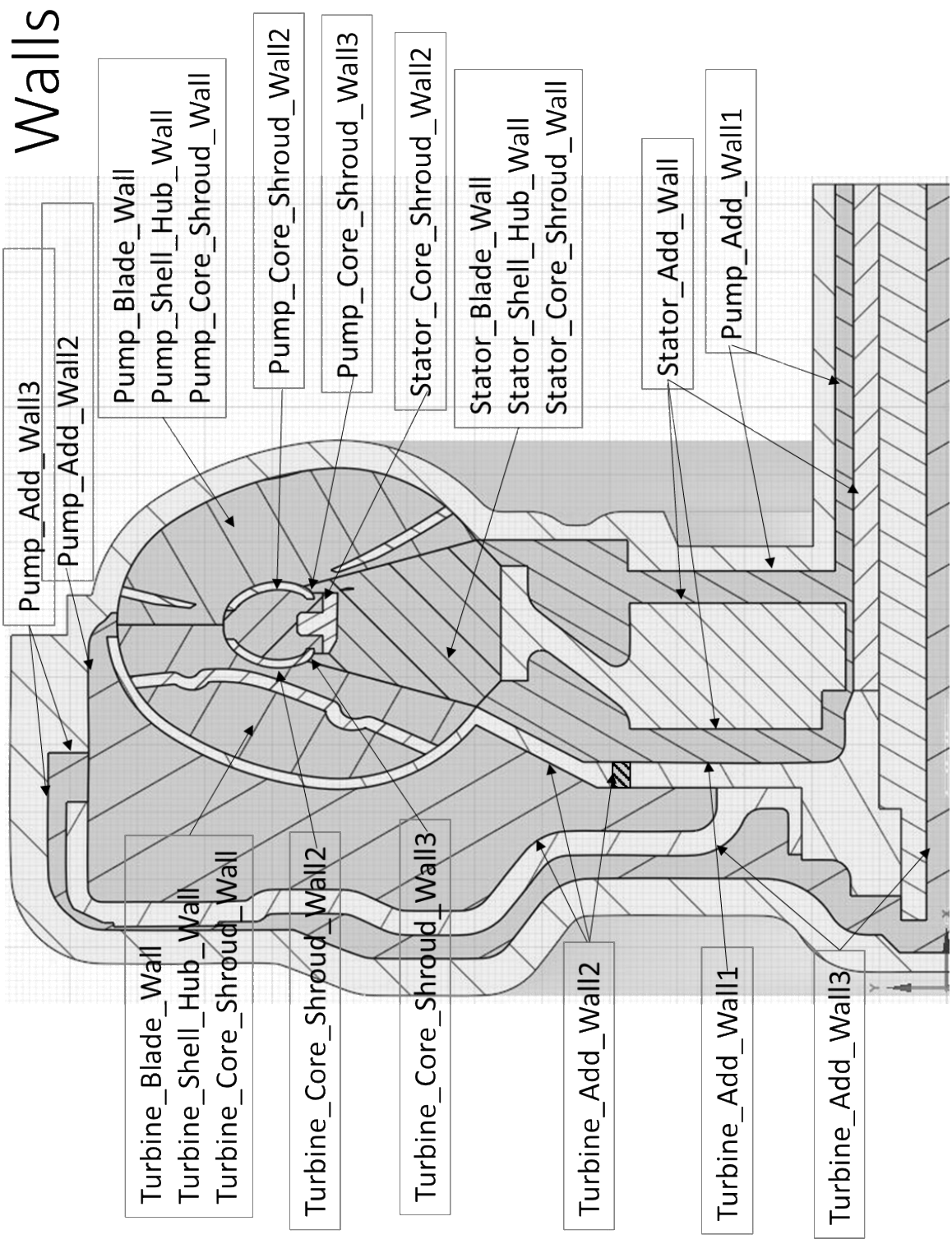

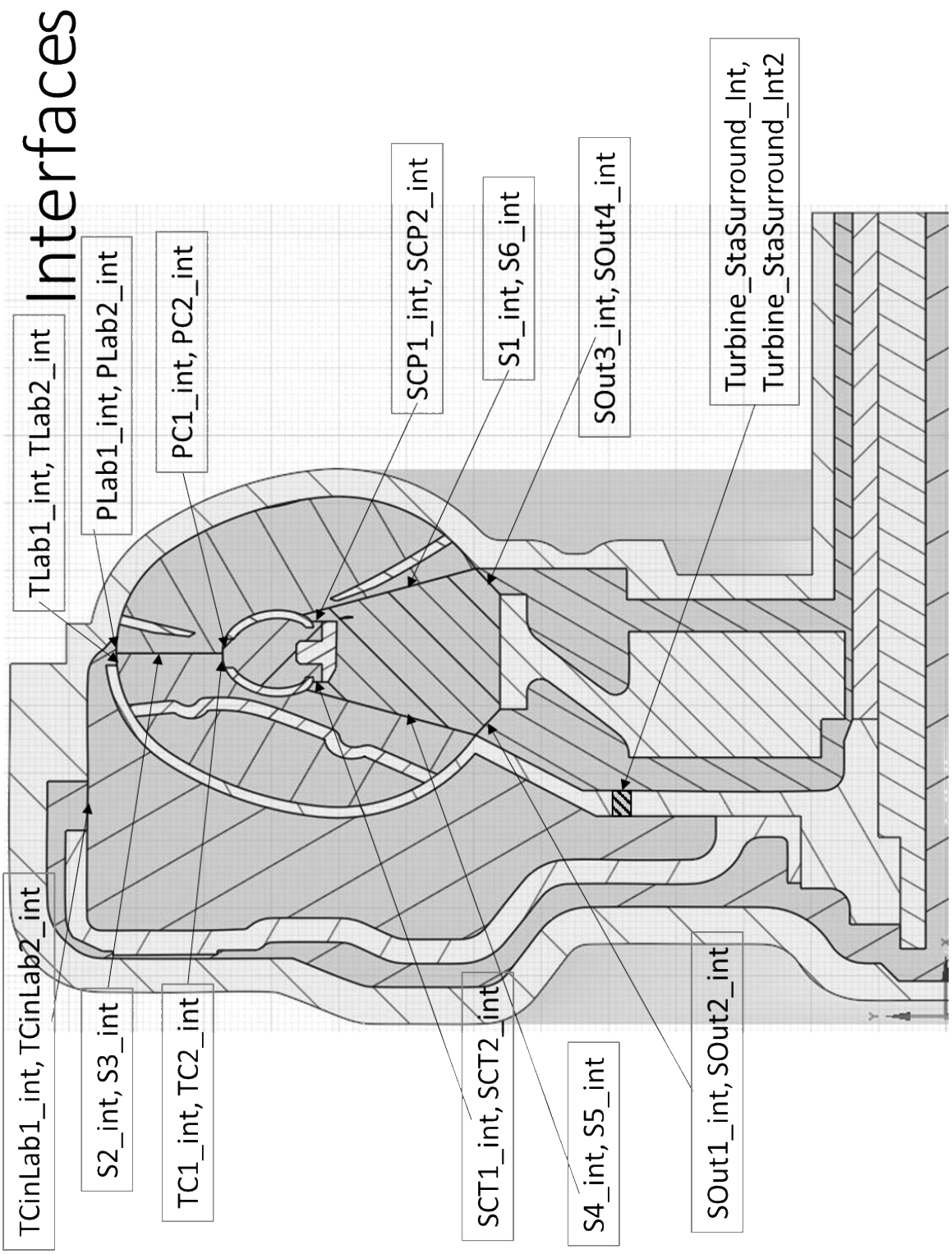

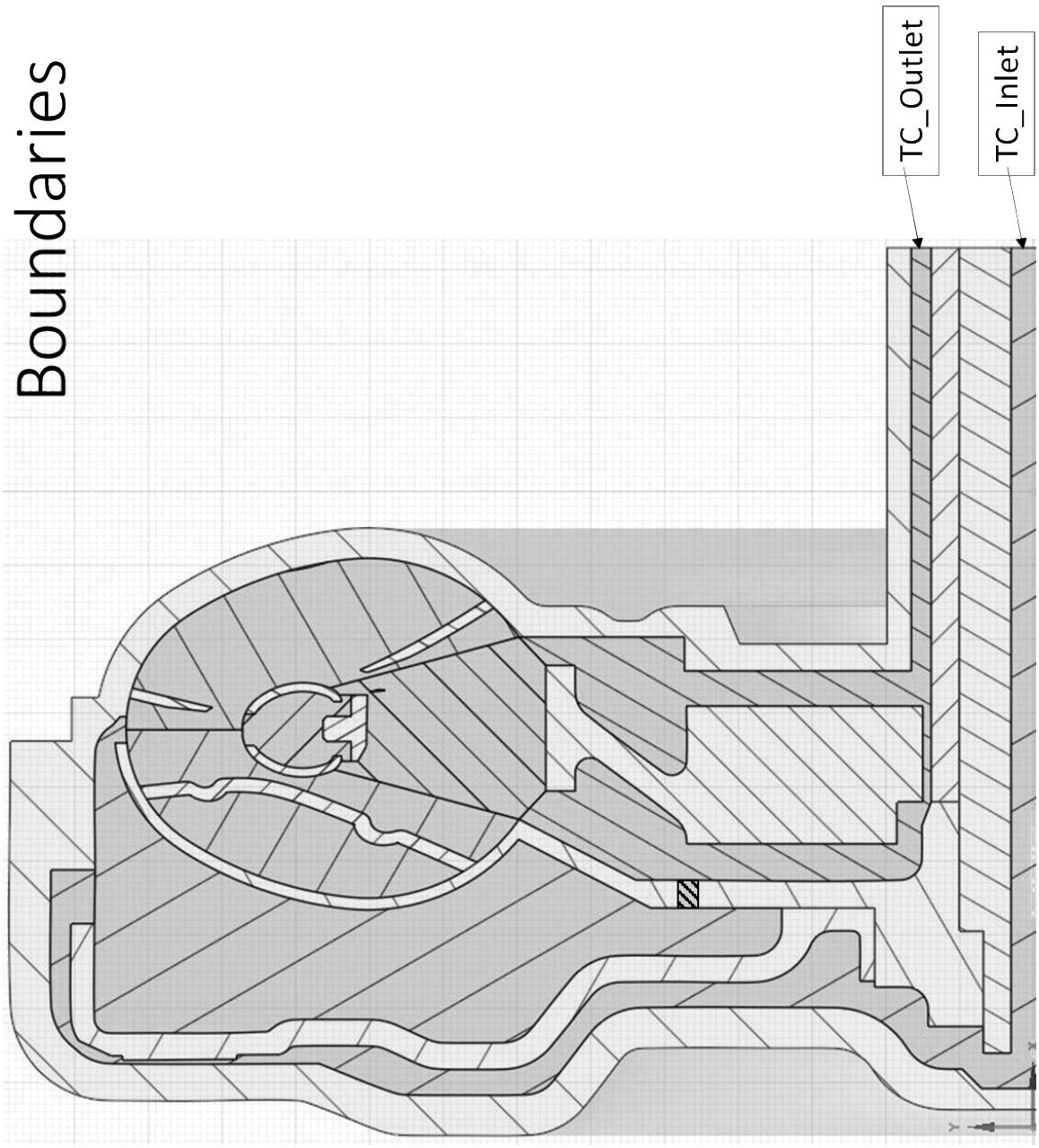

F. Selected Photos

F.1 Laboratory

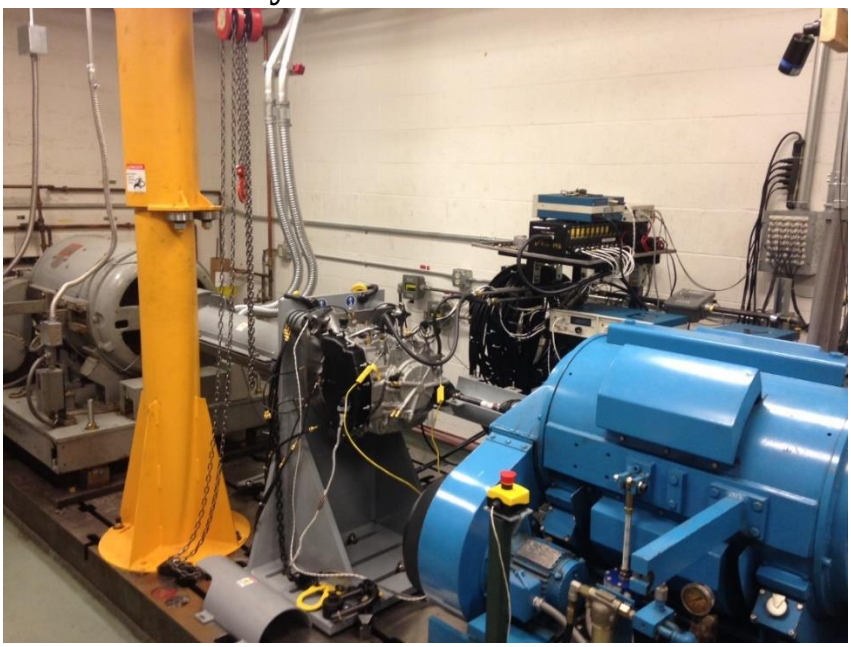

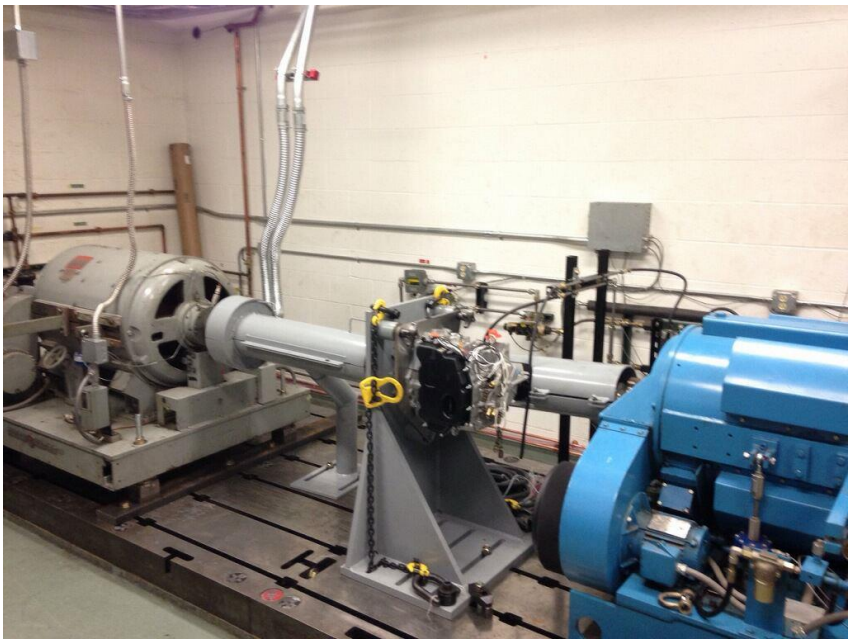

F.2 Main Power Induction Coil

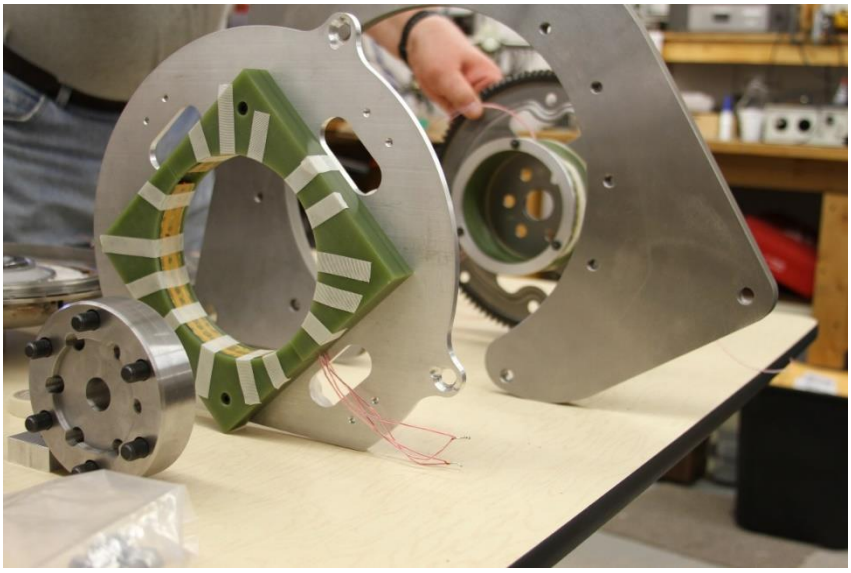

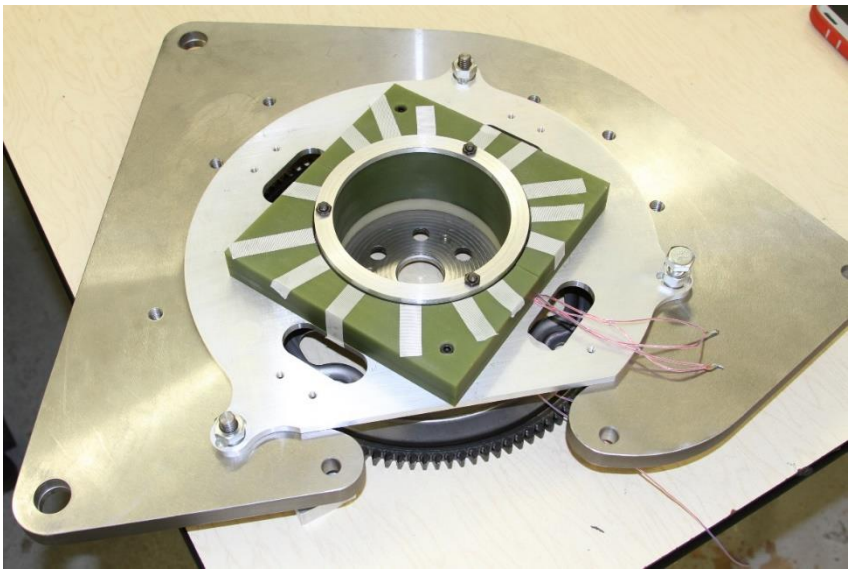

F.3 Torque Converter Instrumentation

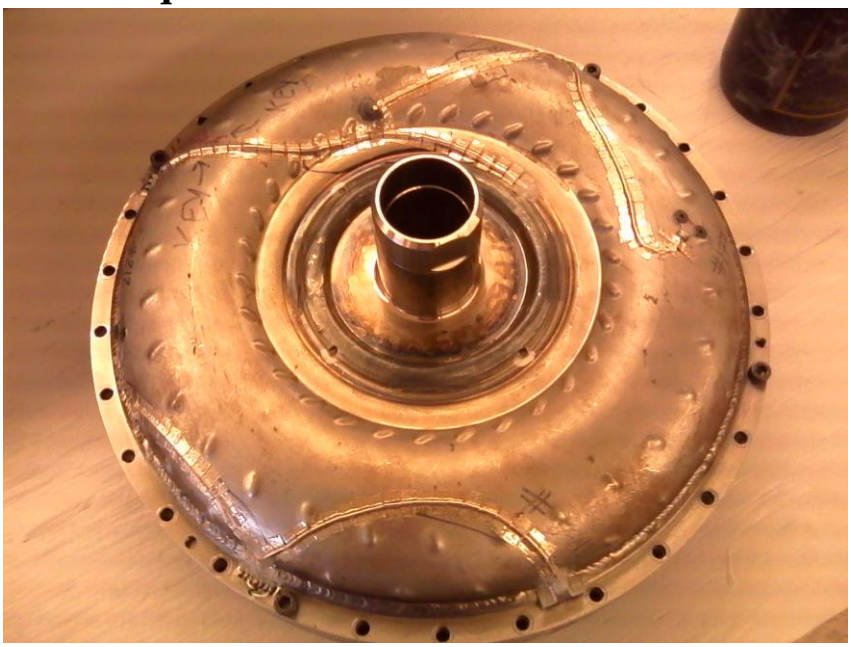

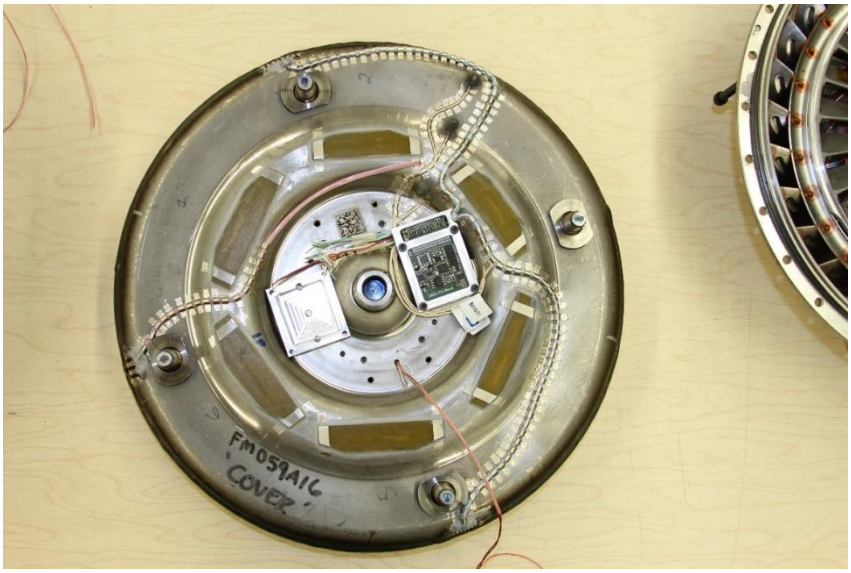

F.4 Impeller & TC Cover

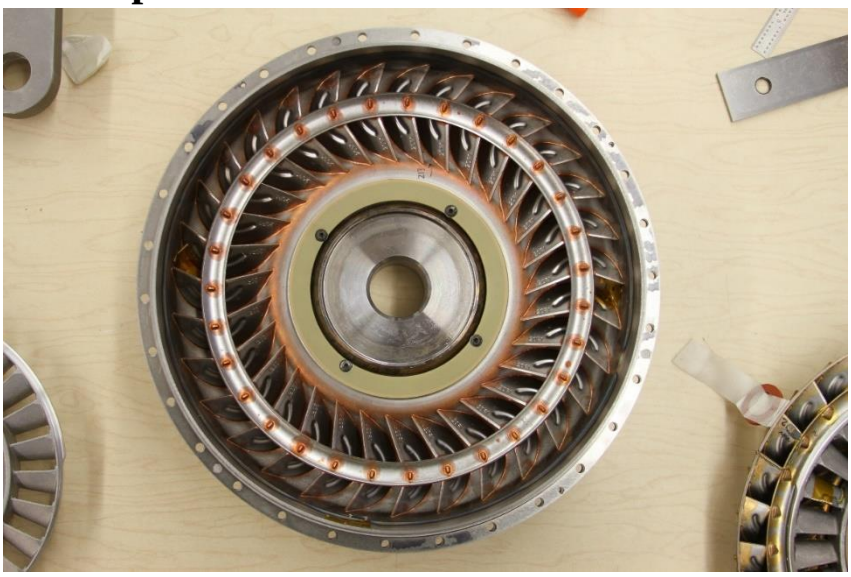

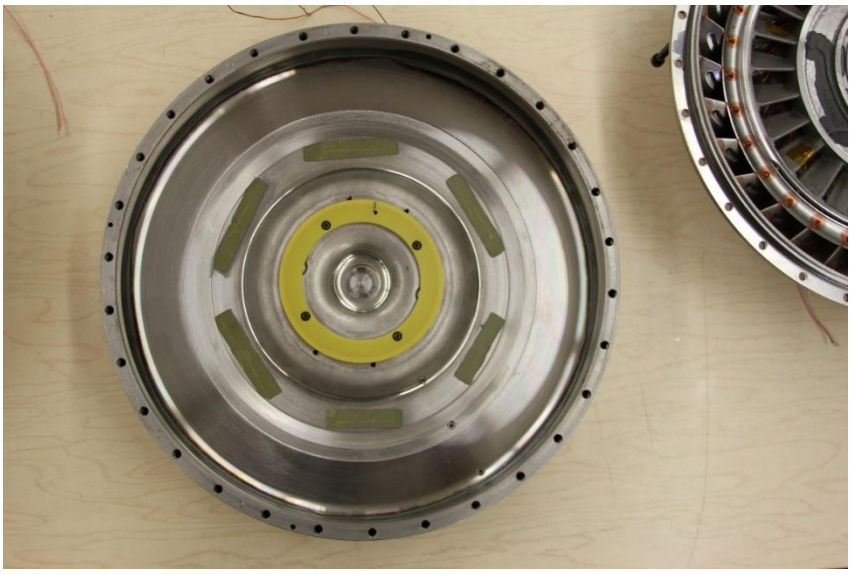

F.5 Turbine

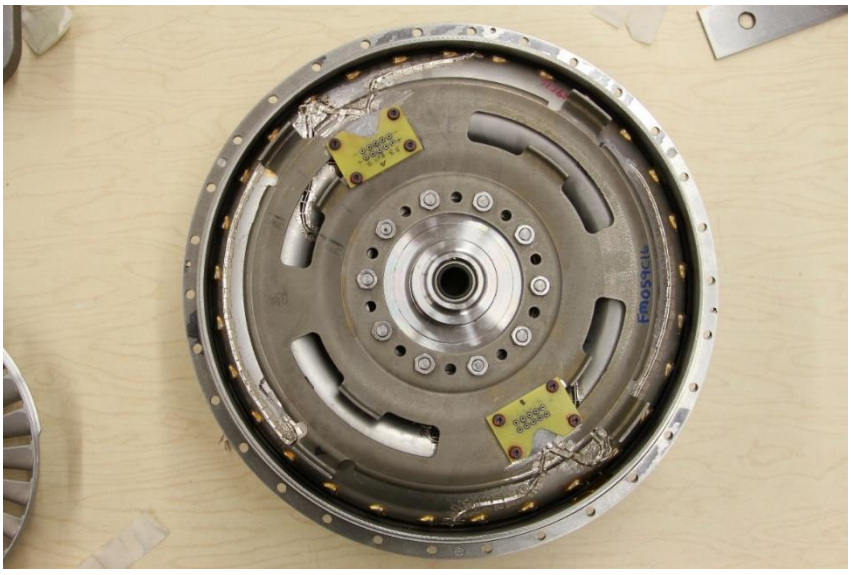

F.6 Stator

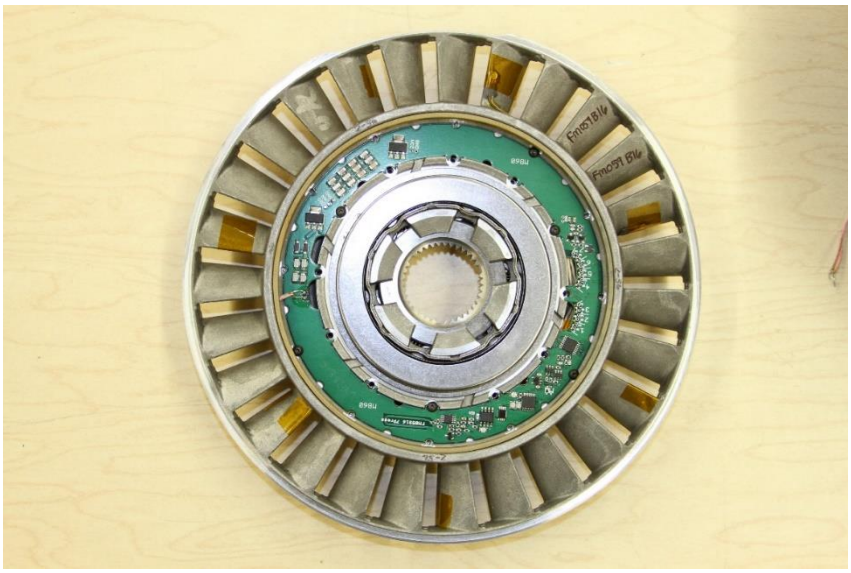

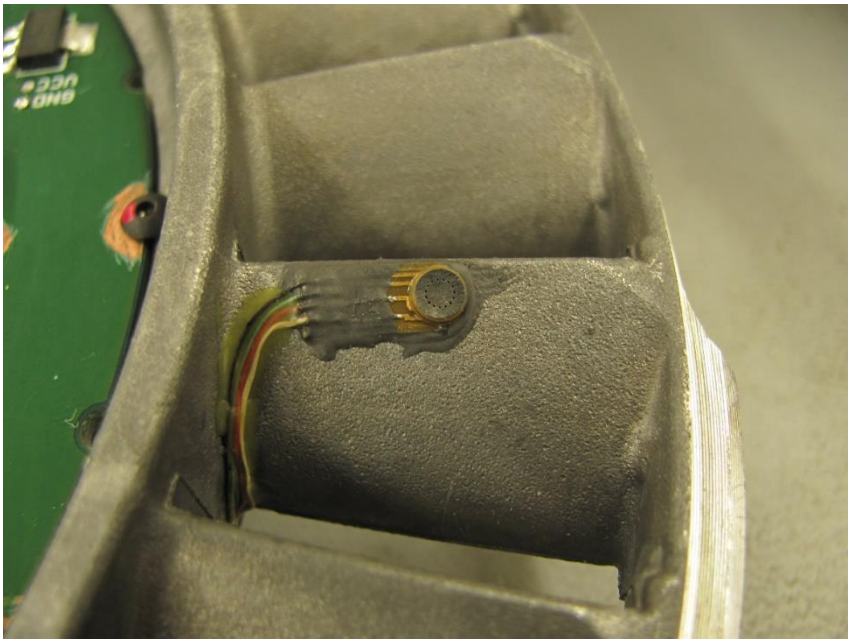

F.7 Pressure Plate

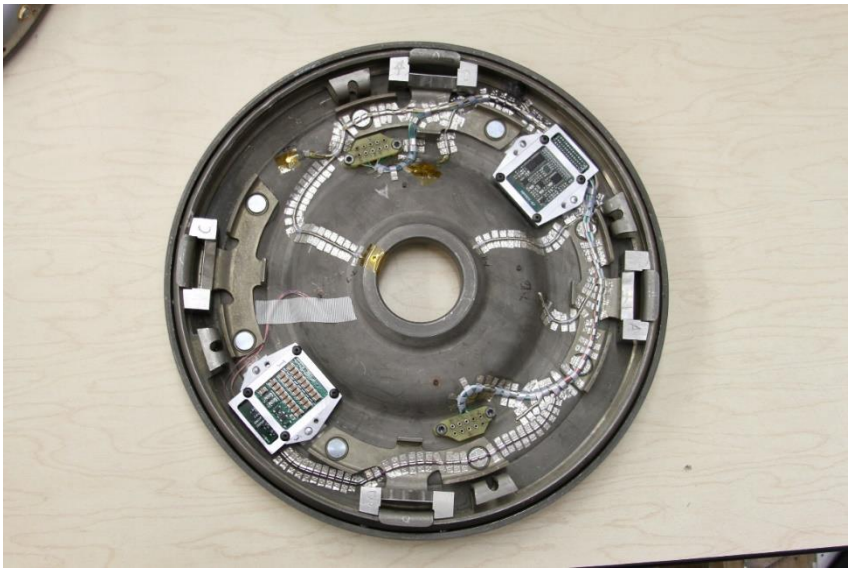

F.8 Antennas on Bell Housing

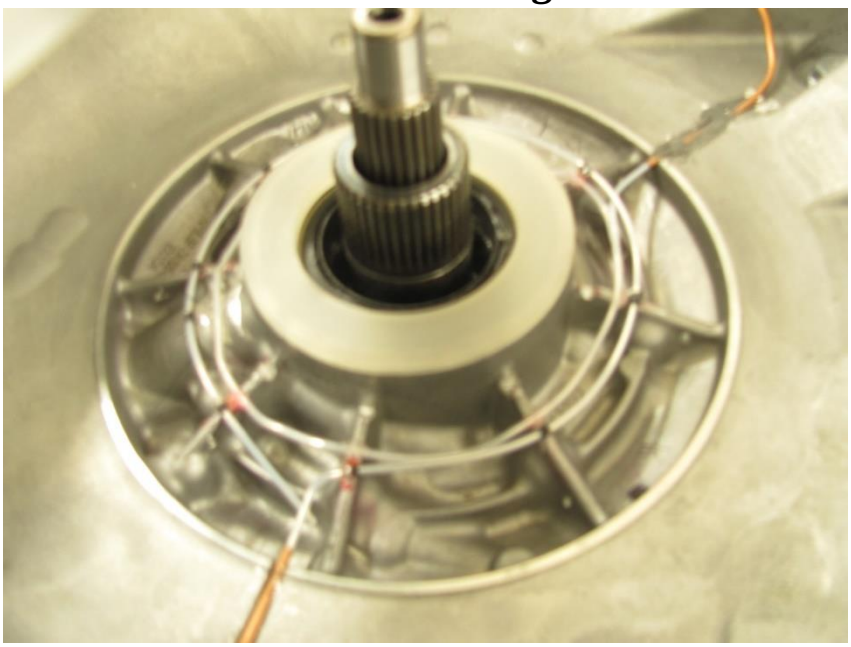

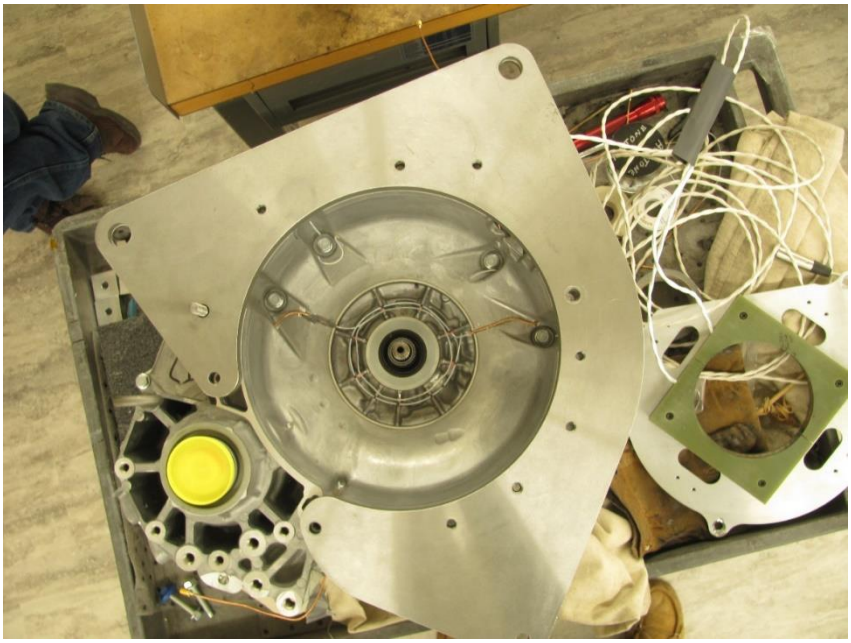

G. Spalart-Allmaras Model Modifications

Spalart-Allmaras turbulence model as defined by the commercially available software used as part of this investigation is defined as follows.

$$\frac{\partial}{\partial t}(\rho\tilde{\nu}) + \frac{\partial}{\partial x_i}(\rho\tilde{\nu}u_i) = G_\nu + \frac{1}{\sigma_{\tilde{\nu}}}\left[\frac{\partial}{\partial x_j}\left\{(\mu_t + \rho\tilde{\nu})\frac{\partial\tilde{\nu}}{\partial x_j}\right\} + C_{b2}\rho\left(\frac{\partial\tilde{\nu}}{\partial x_j}\right)^2\right] - Y_\nu + S_{\tilde{\nu}}$$

"μ_t" represents the turbulent viscosity.

$$\mu_t = \rho\tilde{\nu}f_{\upsilon 1}$$

"$f_{\upsilon 1}$" represent the viscous damping.

$$f_{\upsilon 1} = \frac{\chi^3}{\chi^3 + C_{\upsilon 1}^3}$$

$$\chi = \frac{\tilde{\nu}}{\nu}$$

The production of turbulent viscosity (G_ν).

$$G_\nu = C_{b1}\rho\tilde{S}\tilde{\nu}$$

$$\tilde{S} = S + \frac{\tilde{\nu}}{\kappa^2 d^2}f_{\upsilon 2}$$

"*d*" represents the distance from the wall. "*S*" is a scalar measure of the deformation tensor and is based on the magnitude of the vorticity.

$$S \equiv \sqrt{2\Omega_{ij}\Omega_{ij}}$$

Where Ω_{ij} is a tensor representing the mean rate of rotation.

$$\Omega_{ij} = \frac{1}{2}\left(\frac{\partial u_i}{\partial x_j} - \frac{\partial u_j}{\partial x_i}\right)$$

$$f_{v2} = 1 - \frac{\chi}{1 + \chi f_{v1}}$$

The destruction of turbulent viscosity (Y_v).

$$Y_v = C_{w1}\rho f_w \left(\frac{\tilde{\nu}}{d}\right)^2$$

$$f_w = g\left[\frac{1 + C_{w3}^6}{g^6 + C_{w3}^6}\right]^{1/6}$$

$$g = r + C_{w2}(r^6 - r)$$

$$r \equiv \frac{\tilde{\nu}}{\tilde{S}\kappa^2 d^2}$$

All constants are defined as follows.

$$C_{b1} = 0.1355, C_{b2} = 0.622, \sigma_{\tilde{\nu}} = \frac{2}{3}, C_{v1} = 7.1, \kappa = 0.4187$$

$$C_{w1} = \frac{C_{b1}}{\kappa^2} + \frac{(1 + C_{b2})}{\sigma_{\tilde{\nu}}}, C_{w2} = 0.3, C_{w3} = 2.0$$

G.1 S-A Modifications Effects on Torque

Torque converter stall was used to study effects of modifying the Spalart-Allmaras coefficients. Only sigma and Cb2 were targeted. Modifying any of the default parameters is not recommended. This exercise was done to understand the effects of changing such coefficients.

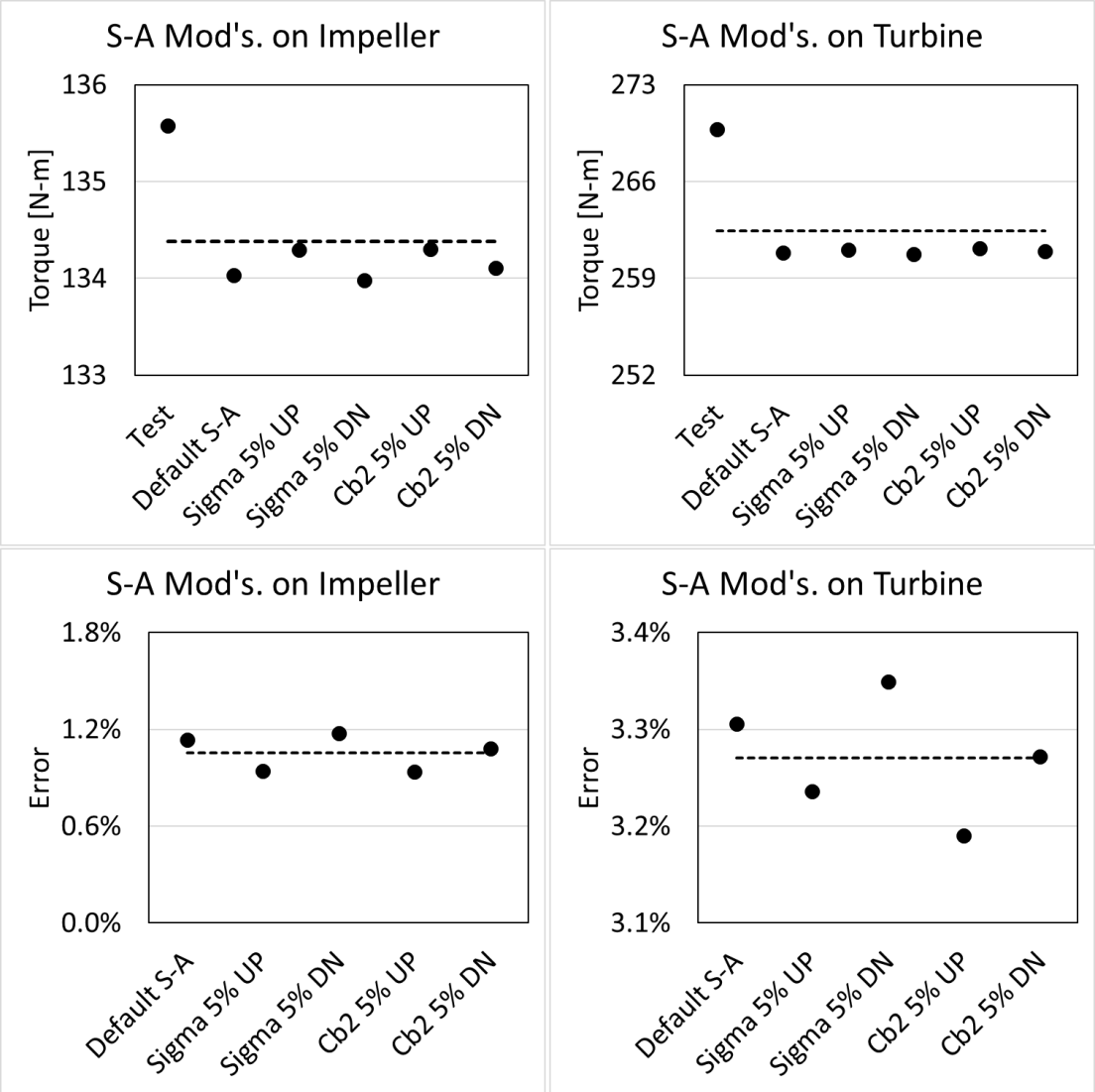

Results show that Cb2 and sigma modifications of 5% on either direction results in a negligible changes in predicted torques.

G.2 S-A Modifications Effects on Pressure

The 5 different cavities of the torque converter shown in Figure 4-28 through Figure 4-30 were studied as part of the Spalart-Allmaras modifications.

G.2.1 Impeller Cavity

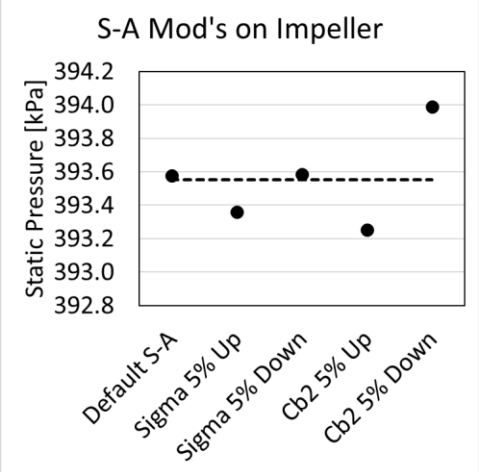

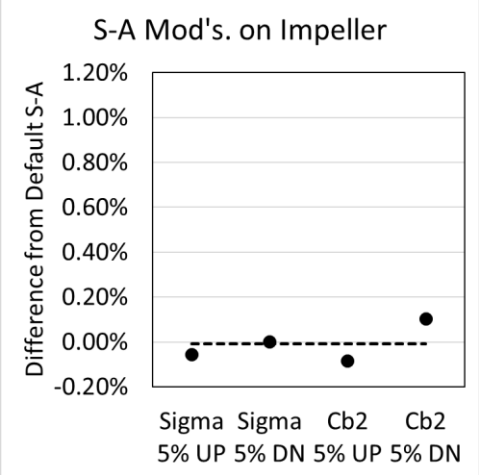

G.2.2 Turbine Cavity

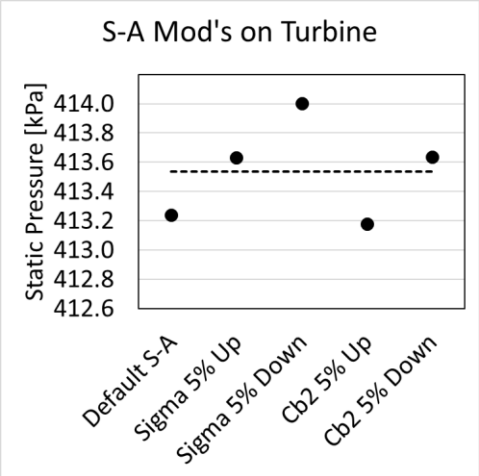

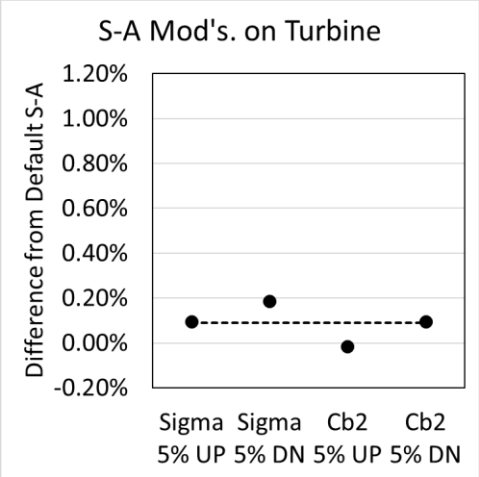

G.2.3 Stator Cavity

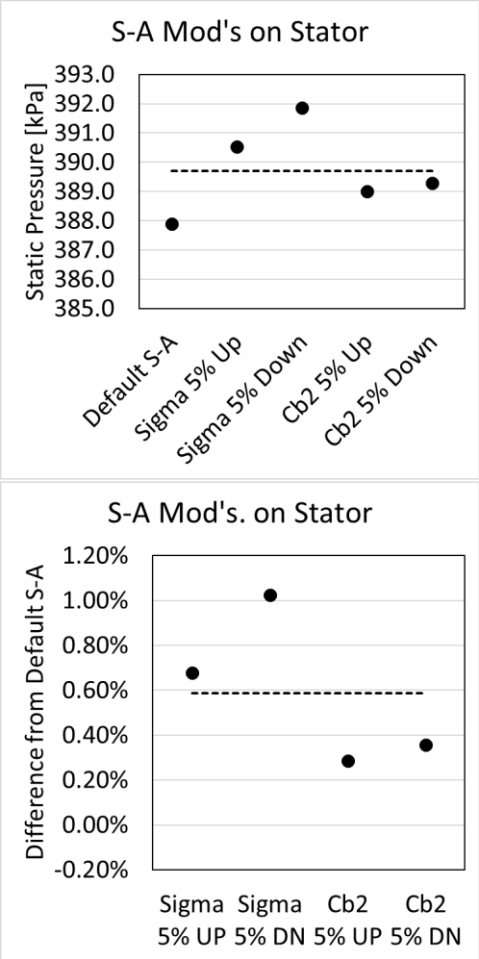

Spalart-Allmaras turbulence model modifications had higher impact on the stator instrumentation than any of the other cavities.

G.2.4 Clutch Cavity

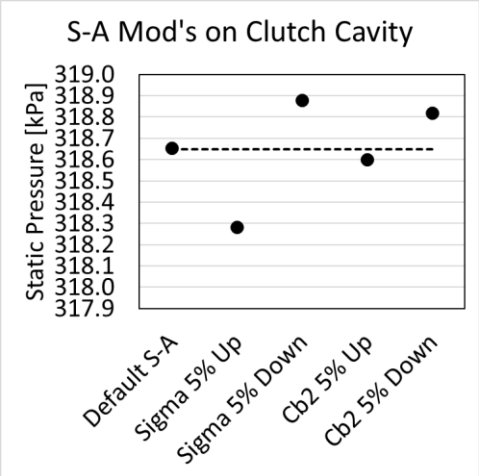

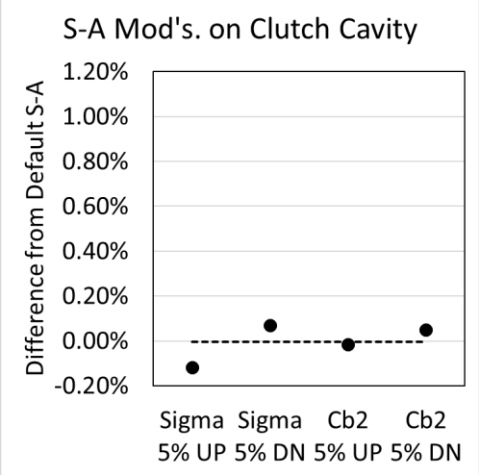

G.2.5 Pressure Plate/Turbine Shell Cavity